Design and Development of a Novel Reconfigurable Wheeled Robot for Off-Road Applications

Tamer S.A. Attia

Dissertation submitted to the Faculty of the
Virginia Polytechnic Institute and State University
in partial fulfillment of the requirements for the degree of

Doctor of Philosophy
in
Mechanical Engineering

Kevin B. Kochersberger, Chair
Tomonari Furukawa, Co-Chair
Corina Sandu
John B. Ferris
Pratap Tokekar

September 21, 2018
Blacksburg, Virginia

Keywords: Elastic actuated mechanism, Agile reconfigurable robot, Rough terrain, Optimal control, Uncertainties.

Design and Development of a Novel Reconfigurable Wheeled Robot for Off-Road Applications

Tamer S.A. Attia

(ABSTRACT)

Autonomous navigation with high speed in rough terrain is one of the most challenging tasks for wheeled robots. To achieve mobility over this terrain, a high agility wheeled robot should adapt and react fast to optimally traverse this challenging environment. Therefore, this dissertation is geared towards the design and development of a novel reconfigurable wheeled robot paradigm for rough terrain applications.

This research focuses on the design, modeling, analysis and control of the reconfigurable wheeled robot, TIGER, with an elastic actuated mechanism for improving the robot's dynamic stability on rough terrain by controlling the robot's ground clearance, body roll and pitch angles. The elastic actuated mechanism mainly consists of a linear actuator connected in series with a shock absorber. Four sets of the elastic actuated mechanism are used to create different robot configurations to adapt to the terrain.

Three main aspects were considered in this research in order to extend the ability of the robot to effectively navigate in rough terrain. The first aspect focuses on designing an agile reconfigurable wheeled robot by including an elastic actuated mechanism for improving maneuverability, longitudinal/lateral stability, and rollover prevention. Robot agility, stability, and high speed have been considered during the design process. The new design provides different configuration modes. These configurations allow for controlling the robot's Center Of Mass (COM) height and optimally distribute the vertical force on each tire for enhancing the tractive efficiency, mobility and dynamic stability.

The second aspect presents the robot kinematic and dynamic modeling and analysis. The robot dynamics model is represented with fourteen degrees of freedom (DOF), where the

dynamic behaviors of the robot body, suspension system, forces and moments on the tires are included. The dynamic behavior is controlled using the linear actuators' position and speed as inputs to determine the resulting ground clearance, body roll, and pitch angles. Sensors are integrated onboard the robot to calculate the robot's states in real time for use in feedback control.

The third aspect focuses on introducing a technique for estimating the robot state-space dynamic model and control the Elastic Actuated Mechanism (EAM) using only a noisy Inertial Measurement Unit (IMU) with COM position uncertainty. The simulation results show that the observer estimates the actual behavior of the robot with 95% accuracy and up to 20% COM uncertainty. The Root Mean Square (RMS) has been reduced by 21% for bounce, 51% for pitch and 50% for roll acceleration.

Design and Development of a Novel Reconfigurable Wheeled Robot for Off-Road Applications

Tamer S.A. Attia

(GENERAL AUDIENCE ABSTRACT)

Wheeled mobile robots are being used for rough terrain applications in the field of robotics as a practical solution to accomplish various tasks. Unfortunately, most of the wheeled robots are not able to perform high dynamically tasks with high speed in rough terrain due to complex suspension design, high power-to-weight ratio, high cost and complexity of controlling highly nonlinear model in real-time. Therefore, this dissertation is geared towards the design and development of a novel reconfigurable wheeled robot paradigm for rough terrain applications.

This research focuses on the design, modeling, analysis and control of the reconfigurable wheeled robot, TIGER, with an elastic actuated mechanism for improving the robot's dynamic stability on rough terrain by controlling the robot's ground clearance, body roll and pitch angles. The elastic actuated mechanism mainly consists of a linear actuator connected in series with a shock absorber. Four sets of the elastic actuated mechanism are used to create different robot configurations to adapt to the terrain.

Three main aspects were considered in this research in order to extend the ability of the robot to effectively navigate in rough terrain. The first aspect focuses on designing an agile reconfigurable wheeled robot by including an elastic actuated mechanism for improving maneuverability, longitudinal/lateral stability, and rollover prevention. Robot agility, stability, and high speed have been considered during the design process. The new design provides different configuration modes. These configurations allow for controlling the robot's COM height and optimally distribute the vertical force on each tire for enhancing the tractive efficiency, mobility and dynamic stability.

The second aspect presents the robot kinematic and dynamic modeling and analysis. The robot dynamics model is represented with fourteen degrees of freedom (DOF), where the dynamic behaviors of the robot body, suspension system, forces and moments on the tires are included. The dynamic behavior is controlled using the linear actuators' position and speeds as inputs to determine the resulting ground clearance, body roll, and pitch angles. Sensors are integrated onboard the robot to calculate the robot's states in real time for use in feedback control.

The third aspect focuses on introducing a technique for estimating the robot state-space dynamic model and control the EAM using only a noisy IMU with COM position uncertainty. The simulation results show that the observer estimates the actual behavior of the robot with 95% accuracy and up to 20% COM uncertainty. The RMS has been reduced by 21% for bounce, 51% for pitch and 50% for roll acceleration.

Dedication

To the memory of my best friend Hany Mokhtar. You will forever be remembered, missed, and loved.

Acknowledgments

First of all, I would like to begin by thanking Almighty Allah for allowing me to pursue my graduate study so far. Secondly, I would like to thank the Military Technical College and the Egyptian Armed Forces for providing me this oppotunity with the scholarship I was granted in the last three years.

I would like to thank my beloved wife, Nehal, for her support and encourage throughout my education. Without her love and understanding, I would not be able to complete this research.

Thanks to my advisor Prof. Kevin Kochersberger for having me as a P.hD. student in Virginia Tech and giving me the opportunity to work on the field of robotics. I am very grateful for the guidance, resources, and advice that have been provided to me by his experience and during designing and building my robot. I would like to thank him for his trust to advise and work with a senior design team to build a rover.

I would like to express my deepest appreciation and sincere to my co-advisor Prof. Tomonari Furukawa for his support and encouragement throughout my research and during MBZIRC competition. He taught me not to give up even when things seemed impossible and difficult. He taught me what is the meaning of Doctor of Philosophy, what is the meaning of academic research and how to get new ideas. His dedication, motivation and pursuit of excellence along with his continuous stream of ideas has inspired me to do my best.

Thanks as well to my committee members, Prof. Corina Sandu, Prof. John B. Ferris and Prof. Pratap Tokekar for their time, counsel and support.

I would like to extend my sincerest gratitude to Dr. John Bird. It was an honor for me to work with him. I feel lucky and blessed for having him during my research. Thanks for your support, guidance and time.

It was also a great pleasure for me to advise, work and interact with the first team from VT to design and build a rover for the 2018 University Rover Challenge. Many thanks for all the team members; Andrew Beckwith, Franco Honores, Muhammad Rehan Khan, Nash Kocur, Yifei Lang, Jhonatan Lavayen, Cornelius Leary, Eric McAchren, Julianna Neumann, Sebastian Villacis, and Anthony Wagner.

Finally, I would like to thank all the members of USL and CMS labs here in Virginia Tech for helping and support. In particular, Karim Abdelatty, Jonathan Hodge, Haseeb Chaudhry, Drew Morgan, Georgios Kontoudis, Jeeseop Kim, Ashrarul Haq Sifat, Yazhe Hu, Ioannis Papakis, Murat Ambarkutuk, Diya Li, Mengyu Song, Cong Chen, Urvi Desai, Jihong Cai, Brian Cesar-Tondreau, and Alfred Mayalu.

Contents

List of Figures

List of Tables

Nomenclature

a, b	COM location from front and rear wheels
e_x, e_y	COM position uncertainty
$F_{G_x}, F_{G_y}, F_{G_z}$	Gravitational forces
$F_{X_i}, F_{Y_i}, F_{Z_i}$	Tire forces expressed at the robot frame of reference
$F_{x_i}, F_{y_i}, F_{z_i}$	Tire forces expressed at wheel coordinate system
F_{s_i}, F_{d_i}	Spring and damping forces at each robot corner
F_i	Actuator force of the EAM
F_{R_i}	Rolling resistance force
g	Gravitational acceleration
h_g	Robot COM height w.r.t global frame
I_{xx}, I_{yy}, I_{zz}	Mass moment of inertia of the robot's body
I_{xy}, I_{yz}, I_{zx}	Mass product moment of inertia of the robot's body
I_{w_i}	Mass moment of inertia of wheels
$K_{f,r}$	Suspension spring stiffness (front/rear)
$C_{f,r}$	Suspension damping coefficient (front/rear)
L	Robot wheelbase

M_X, M_Y, M_Z	Moments applied to robot's body
$m_{f,r}$	Suspension mass (front/rear)
m_s	Robot's body mass
m_t	Robot total mass
m_w	Wheel mass
p, q, r	Rotational velocities (roll, pitch and yaw) w.r.t robot local frame
r_d	Wheel dynamic radius
S_{x_i}, S_{y_i}	Longitudinal and lateral slip ratios
T_i	Driving moment applied at each wheel hub
T_s	Sampling rate
U, V, W	Translational velocities in (X, Y, Z) w.r.t robot local frame
V_{x_i}, V_{y_i}	Longitudinal and lateral velocities w.r.t robot local frame
V_{xw_i}, V_{yw_i}	Longitudinal and lateral velocities w.r.t wheel reference frame
x_G, y_G, z_G	Robot COM position
w_1	Wheel track from COM to front left tire
w_2	Wheel track from COM to front right tire
w_3	Wheel track from COM to rear left tire
w_4	Wheel track from COM to rear right tire
z	Robot's body displacement
z_{r_i}	Road displacement at each tire
z_{w_i}	Wheel vertical displacement
ϕ, θ, ψ	Euler angles

ζ	Coefficient of rolling resistance
α_i	Lateral slip angle
η_i	Relative dynamic tire load
μ_i	Relative suspension deflection
σ_ν	White Gaussian noise
ν	Measurement uncertainty
ω_b	Breaking frequency

Glossary

COM	Center Of Mass
DAE	Differential Algebraic Equation
DOF	Degree Of Freedom
EAM	Elastic Actuated Mechanism
IMU	Inertial Measurement Unit
ISO	International Organization for Standardization
LQG	Linear Quadratic Gaussian
LQR	Linear Quadratic Regulator
PID	Proportional–Integral–Derivative
PSD	Power Spectral Density
RMS	Root Mean Square
ROS	Robot Operating System

Chapter 1

Introduction

This chapter introduces the work that has been carried out as part of this research. The chapter discusses the background and challenges of the dissertation research, objectives, the principal contributions, and finally a concise description of the dissertation outline.

1.1 Background

One of the most challenging task for an off-road robot is traversing in unstructured rough terrain with high speed and high stability. In critical situations after any disaster, the terrain is poorly characterized and may be slippery, deformable, bumpy with steep slopes. Undoubtedly, there is still much progress to be made in introducing a robust robot that has the capability to work in such environment at high speed with high stability and follow the optimal trajectory to reach its final destination. In fact, some existing wheeled robots that are working in rough terrain lack the ability to perform high dynamically tasks with high speed. The main reason for this is the limited innovative actuated suspension design with a less power-to-weight ratio. Actually, most of the rough terrain robots are using passive

suspension or a suspension actuated with low-speed motors which cannot handle the high dynamic tasks.

On the other hand, legged robots are introduced for rough terrain tasks as a promising solution. Legged robots have many advantages over wheeled and tracked robots in terms of agility and mobility on uneven terrain. For instance, Boston Dynamics robots; Atlas and SpotMini stunned the researchers with their online videos that demonstrated their ability to perform highly dynamic tasks like jumping, balancing, climbing stairs and adaption to the terrain and external uncertainties.

Despite the advantages of humanoid and quadruped robots, there are disadvantages related to high cost, limited speed, stability and complexity for controlling many degrees of freedom in real-time.

Therefore, there is a powerful motivation to introduce a high agility robot that can react and adapt to different terrain variations very fast with high stability with a simple design, low cost and simple control algorithm.

This dissertation is a stepping stone to introduce an agile reconfigurable wheeled robot with EAM that has the capabilities to work in challenging terrain with high stability. Possible applications for this robot platform are:

- Transporting emergency supplies in disaster situations.
- Search and rescue in a large area.
- Collecting soil samples in contaminated zones.
- Agriculture tasks including harvesting, monitoring, and high-precision seeding.
- Planetary exploration missions.
- Various military applications.

1.2 Research Objectives

Based on the above mentioned reasons, this research is focusing on introducing an intelligent solution for improving the performance and dynamic stability of high-speed wheeled robot that working on the complex environment. Three main objectives were considered in this research to extend the ability of the wheeled robot to traverse rough terrain as follow:

- **Reconfigurable wheeled robot design:** To design a robot with agile reconfigurable body by including actuated suspension system for improving longitudinal/lateral stability, and prevent robot's rollover on uneven terrain. The design should consider high speed mobility, agility, low weight, low cost, and high strength. The active suspension system mainly consists of a linear actuator connected in series with a shock absorber. This configuration allows for controlling the UGV's COM height and optimally distribute the vertical force on each tire for enhancing the tractive efficiency and dynamic stability. The robot dynamics model is represented with fourteen DOF, where it is including the dynamic behaviors of the sprung mass, suspension system, forces and moments on the tires.

- **Robot mechanics and control analysis:** presented the robot kinematic and dynamic modeling and analysis, The robot dynamics model is represented with fourteen degree of freedom (DOF), where it is including the dynamic behaviors of the robot body, suspension system, forces and moments on the tires for analyzing the dynamic behavior using the linear actuators positions and speeds as inputs to determine the resulting ground clearance, body roll and pitch angles. Sensors are integrated on-board the robot to calculate the robot's states in real time for use in feedback control. An unified dynamics control for maneuvering stability based on active suspension/traction system is employed to increase the admissible stability region.

- **Dynamic model estimation and control** introducing a novel technique to estimate the robot dynamics and control the active suspension system using only a noisy single point sensor with center of mass position uncertainty. The simulation results show that the observer estimates the actual behavior of the vehicle with 95% accuracy and up to 20% COM uncertainty. The RMS has been reduced by 21% for bounce, 51% for pitch and 50% for roll acceleration.

1.3 Contribution

The main contributions of this research can be summarized as follows;

- Designed and developed a reconfigurable wheeled robot with high speed, agility and stability capabilities using Elastic Actuated Mechanism (EAM).

- Online optimal tire forces distribution for improving dynamic stability and traction efficiency on uneven terrain.

- Simultaneous dynamic system estimation and optimal control of robot's EAM with a parametric study on the effect of COM uncertainty.

This dissertation introduces and develops TIGER, a reconfigurable wheeled robot with an elastic actuated mechanism to increase the wheeled robot agility in rough terrain. The EAM is a novel mechanism that adding more degree of freedom between each tire and the robot's body. The EAM is driven by a linear motor connected in series with a shock absorber for precisely controlling the suspension height and simultaneous dynamically react with the terrain variations.

1.4 Publications

Disclosure: This dissertation uses some of the contents from the following publications:

- **T. Attia**, K. Kochersberger, J. Bird, S. Southward, "System Identification and Optimal Control of Half-Car Active Suspension System Using A Single Noisy IMU With Position Uncertainty," *in ASME 2017 Dynamic Systems and Control Conference. 2017. American Society of Mechanical Engineers.*
- **T. Attia**, K. Vamvoudakis, K. Kochersberger, J. Bird, T. Furukawa, "Simultaneous Dynamic System Estimation and Optimal Control of Vehicle Active Suspension," *Vehicle System Dynamics, 2018.*
- J. Hodes, **T. Attia**, T. Furukawa, et al, "Multi-stage Bayesian Autonomy for High-precision Operation in a Large Field," *Journal of Field Robotics, 2018;1–21.*
- T. Furukawa, G. Dissanayake, **T. Attia**, J. Hodes, "A Bayesian Framework for Simultaneous Robot Localization and Target Detection and Engagement," *IEEE/RSJ IROS, 2018.*

1.5 Dissertation Outline

This dissertation is organized in seven chapters. A brief description of the issues discussed in each chapter is given below:

Chapter 1: Introduction

Summarize the background and challenges of the proposed work, as well as the overall objectives and main contributions. A brief description of the research framework is outlined.

Chapter 2: Literature Review

A review of the state-of-the-art in the field of rough terrain robots is presented. The survey covers the aspects of various design and control methodologies for rough terrain robots with focusing on the reconfigurable wheeled robots.

Chapter 3: Robot Design Paradigm

A detailed explanation of the robot design process is introduced through this chapter. The design requirements and the robot configuration modes have been illustrated to ensure robot agility, stability with modular body structure. The description of the mechanical design, the actuation and sensory systems and the control architecture is demonstrated as well.

Chapter 4: Elastic Actuated Mechanism Modeling, Analysis, and Experimentation

Discusses the robot's suspension system kinematic and dynamic models and the proposed control algorithm for controlling the EAM to improve the quasi-static stability of the robot in rough terrain. In this chapter, we evaluate the performance of the EAM using kinematic and dynamic models with demonstrating the robot performance using several experimental tests.

Chapter 5: Robot Dynamic Modeling, Control, and Analysis

Introduces the robot's dynamic model with 14-DOF which include the dynamics of the robot's body, suspension system, forces and moments on the tires. Validation will be covered in order to design a controller for the suspension system to analyze the dynamic performance through simulation environment. A comparison between passive and active systems is illustrated to reveal the effectiveness of the proposed suspension design and controller in improving the robot stability in rough terrain.

Chapter 6: Estimation and Optimal Control of Robot Dynamics

Introduces a method to estimate the robot dynamics and optimally control the elastic

actuated mechanism system using only a noisy IMU with COM position uncertainty. The derived model is based on a channel-by-channel estimation technique using filtered white noise excitation signals. The transfer functions of the robot dynamics are estimated by analyzing the IMU signals in the frequency domain. The derived result is then used in a linear quadratic regulator to calculate the actuators' forces to stabilize the robot's body and improve the road holding stability within the limits of the rattle space. The simulation results show the efficacy of the proposed approach. Specifically, the observer estimates the actual behavior of the robot with 95% accuracy with up to 20% uncertainty. Finally, a parametric study has been investigated to ascertain the applicability of the proposed approach.

Chapter 7: Conclusions and Future Works

Summarizes the main conclusions and discusses the future work directions that can be achieved by the proposed work in this research.

Chapter 2

Literature Review

This chapter reviews the state-of-the-art in rough terrain robots that working in disaster situations, planetary explorations and military missions. Existing rough terrain robots are first reviewed which can be classified into wheeled robots, tracked robots, humanoid robots, wheeled humanoid robots, and quadruped robots. This chapter also focuses on the reconfigurable wheeled robots and its capability in varying their configuration to improve robot stability and mobility in rough terrain with different control strategies.

2.1 Robots for Rough Terrain

Rough terrain robots are widely used in many applications such as disaster situations. In this critical situation after any disaster, the terrain is poorly characterized and may be slippery, deformable, bumpy with steep slopes. As well as, time is a crucial factor in this situation to provide a fast and reliable help to save people's lives and make the right decisions to keep the responder safe [3]. As stated in the Annual Disaster Statistical Review 2016 [4], there were about 342 disasters are reported with an average of more than 69,00 people were killed, and

more than $150 billions of economic losses in that year. Disaster response robots which some times are called as rescue robots have been used since 2001 [5] to provide real-time data about the event and aid in moving some equipments, turning valves and even with the economic recovery. Because of the nature of the environment as mentioned before about the disaster terrain, the rescue robots should be designed to be fast and adapt with this terrain to have successful missions. Most of ground robot platforms that designed to work in the disaster environment are small platform for rescue people inside collapsed building. For instants, in 2004 Niigata-Chuetsu earthquake the Soryu III snake robot was used for search inside collapsed houses as shown in Figure 2.1a. On the other hand, Quince robot Figure 2.1b was used for structual inspection of damaged building in 2011 Tohoku earthquake, and Packbots robot Figure 2.1c was used with Quince robot during the Fukushima-Daiichi nuclear power plant accident in 2011 for gamma radiation monitoring and debris removal [5]. Telemax and Wolverine are tracked robots equipped with a manipulator which is used for rescue, mining, and military missions as shown in Figure 2.1d and Figure 2.1e.

Planetary exploration missions use wheeled robots which are called as rovers to perform tasks in rough terrain. The space agencies of USA sent four rovers for Martian surface exploration [10, 11, 12, 13]. These four mars rover (Sojourner, Opportunity, Spirit, and Curiosity) are wheeled robots with a passive rocker-bogie suspension for increasing mobility and improving driving performance through Martian surface [14, 15] as shown in Figure 2.2. Two of these rovers had been trapped before in the Martian sand, Spirit and Opportunity, they experienced a deep sinkage in the sand. So, great efforts from the researches to design rovers can traverse soft terrains, climb steep slopes, and have some configuration to adapt with different terrain variations. A new suspension system should be considered for the new rover generations; this suspension system should provide different configuration modes and can distribute the rover weight evenly on all wheels as well as can offer more weight to specific wheel in order to enhance the traction efficiency. Actively reconfigurable planetary rover

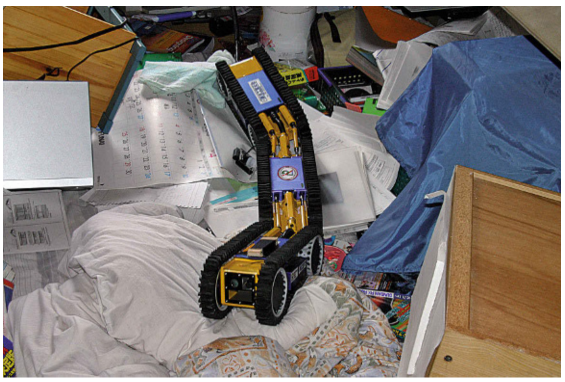

(a) Soryu III snake robot [5].

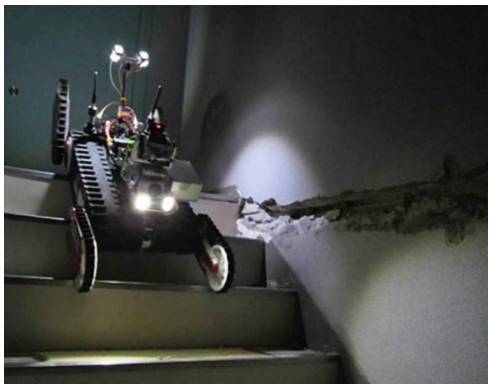

(b) Quince robot [6, 7].

(c) Packbots robot [5].

(d) Telemax robot [5, 8].

(e) Wolverine robot [9].

Figure 2.1: Different disaster response robots.

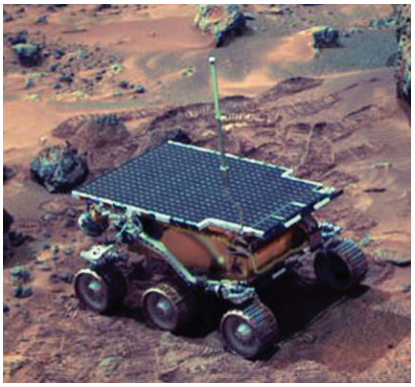

(a) Rover Sojourner.

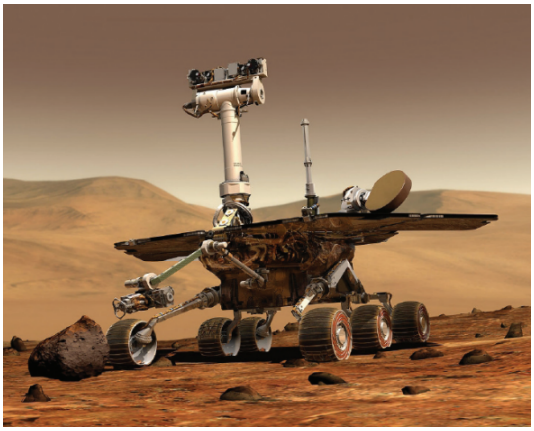

(b) Rover Spirit and Opportunity.

(c) Rover Curiosity.

Figure 2.2: Mars rovers [1].

[12, 16, 17, 18] started to be considered for future Martian exploration missions. Because of this suspension the rovers can modify their configuration to negotiate challenging terrain to improve the rover's stability, adhesion and performance.

Other rough terrain robots are used for different environments; agriculture and forestry [19, 20, 21], industry, hazard applications [22] and mining. With these different robot applications, the rough terrain robots have to be agile and stable during the operation in such environments in order to successfully complete its mission.

2.2 Reconfigurable Wheeled Robots

Reconfigurable wheeled robots as a solution for improving mobility and robot stability on rough terrain had been introduced in many publications [19, 21, 23, 24, 25, 26]. This was achieved by designing an articulated suspension system to allow changing the COM location, the ground clearance, roll and pitch angles. The work of [24] has introduced a kinematic control strategy to improve robot mobility using multiple objectives control based on ground clearance, orientation, stability and traction criteria. However, the proposed control strategy based on kinematics approach which may fail during dynamic interaction between the robot and the terrain with high speed. Another work of [16] has proposed a suspension design with two degree of freedom for controlling each side of the rover suspension dependently in order to negotiate different obstacles and improving the rover stability. The proposed approach is based on changing the rover wheelbase and height to stabilize its drill in contact with the ground and have a different posture to better ascending and descending slopes in rough terrain. This design with only two degree of freedom limits the rover agility to adapt with different terrain by limiting the number of configuration modes.

Improving traction on rough terrain has been deeply studied in [17, 18] and how the traction

performance can be enhanced by changing the robot configuration. The study is based on changing the robot posture to reduce the wheel slippage by studying the relationship between the attitude of the robot and the forces acting on each tire. The research study in [27, 28], the authors also studies the effect of changing the rover configuration on the traction performance to increase the mobility. They investigated the effect of internal force distribution by using active suspension for evaluating the rover mobility, the research results confirm that the traction force is increased by changing the normal force on each tire.

The rover in [25, 29] is equipped with actively articulated suspension system to offer high degree of mobility on Martian surface. The MAMMOTH rover is designed as a reconfigurable wheel-on-leg rover for introducing a variety of locomotion modes to enhance the stability. The Kinematic model of the wheel-on-leg along with a tip-over stability model has been introduced in this research to ensure stability and safety of the system. Moreover, the proposed controller objective is to maintain a constant body pose during traversing uneven terrain with improving the estimation of wheel-terrain contact angle and wheel slippage. However, the proposed robot moves with low speed on uneven terrain due to kinematic limitations model that introduced in this research.

A reconfigurable wheel-legged robot is called Hylos has been introduced in [30] which is using an actively articulated locomotion systems to adapt with the irregular sloping terrain for stability and traction optimization. A sub-optimal approach is presented to optimize both the balance of traction forces and the tipover stability. The control algorithm for posture stability is governed by a velocity model in this work.

Chapter 3

Robot Design Paradigm

The state-of-the-art from the contributed works in the previous chapter section 2.2 shows that there is a potential direction for introducing a high-speed reconfigurable wheeled robot with elastic elements for adapting to terrain irregularities and isolating the robot's body from external disturbances. This chapter presents an overview of the robot design paradigm, which starts with the design requirements and the different robot configuration modes. From these requirements, the robot mechanical design will be discussed in section 3.3 with focusing on the robot body structure and the design of the EAM. Then, the actuation and sensory system will be demonstrated in section section 3.4, and finally the robot control architecture will be discussed in section 3.5.

3.1 System Overview

TIGER is a reconfigurable wheeled robot with electrically actuated suspension system. Figure 3.1 shows a 3D view of the robot with the proposed suspension system. The robot main mechanical structure is built from a strong and light-weight of aluminum alloy sheets, and

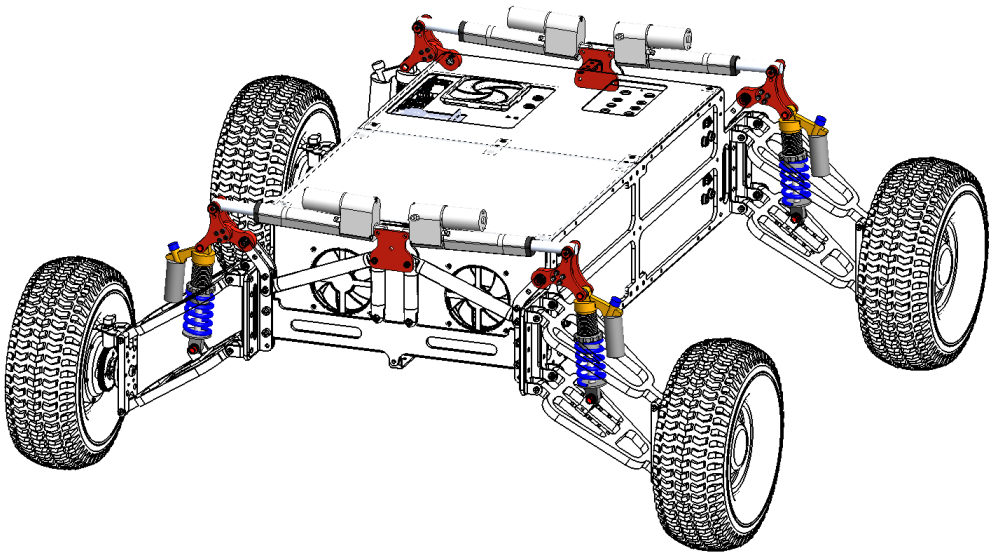

Figure 3.1: 3D model of TIGER with EAM. The proposed robot design is based on adding an extra degree of freedom between the robot's body and each tire.

carbon fiber tubes with some critical components are built using stainless steel. The body structure is designed to be modular as the robot's width, and height can be increased according to the required application and the payload types. The shock absorber stiffness and damping can be modified to adapt to the working conditions and the payload. Brushless in-wheel DC motors are used for driving the robot with high speed and high torque. The high-level control architecture is computed by an onboard computer with Intel® Core™ i7 Processor using Robot Operating System (ROS) framework. Suspension and robot mobility controllers are using different sensors which including speed, position, current sensors and IMU. Table 3.1 gives a summary of the main robot specifications. Figure 3.2 shows all main components of TIGER robot.

3.2 Design Requirements and Configuration Modes

Three main requirements are considered during the design process. First, the robot should move fast by considering a high-speed driving motor with sufficient torque, that is why we

Table 3.1: TIGER wheeled robot main parameters

Dimensions (LxWxH)	135x125:140x58:40 (cm)
Wheel track $(2w)$	112:127 (cm)
COM height (h_g)	20:45 (cm)
COM location from front wheels (a)	50 (cm)
COM location from rear wheels (b)	50 (cm)
Max speed(U)	35 km/h
Body mass (m_s)	41.22 Kg
Tire and suspension mass $(m_{f,r})$	9.67 Kg
Max roll angle (ϕ)	10 $(deg.)$
Max pitch angle (θ)	10 $(deg.)$

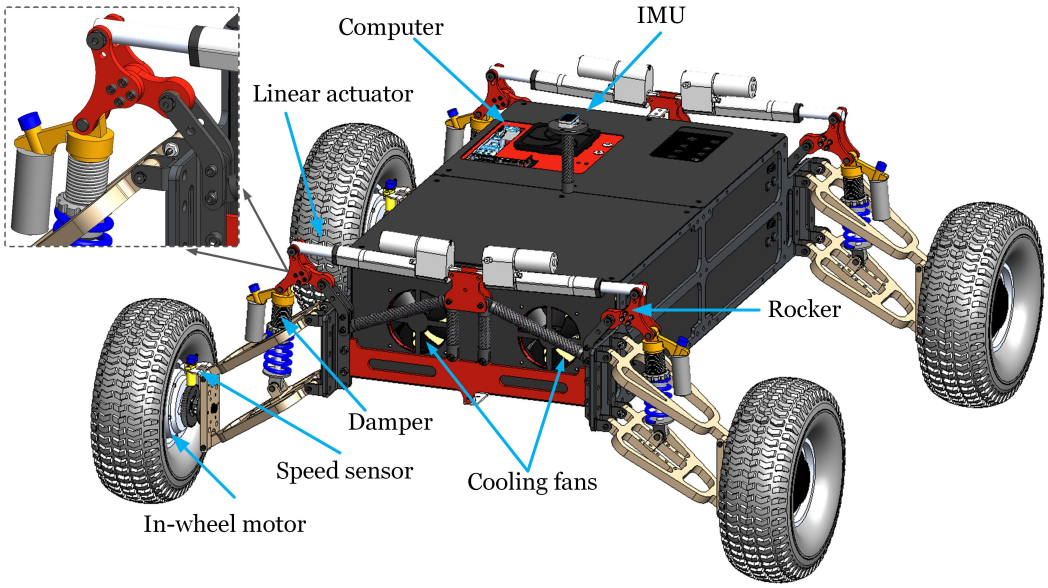

Figure 3.2: 3D CAD model of TIGER with the main components

considered the in-wheel brushless DC motors as a drive train for the robot. In-wheel motors offer numerous potential benefits like; compact design, high acceleration and high speed with high torque. Robot agility is the second design requirement to adapt to the complex terrain. Robot agility comes from the novel suspension design; we considered different travel suspension system which aims to enable the robot to travel over rough terrain while keeping the robot's body stable and minimizing the bounce, roll and pitch accelerations. We considered an elastic actuated mechanism between the tire and the robot body to have different robot

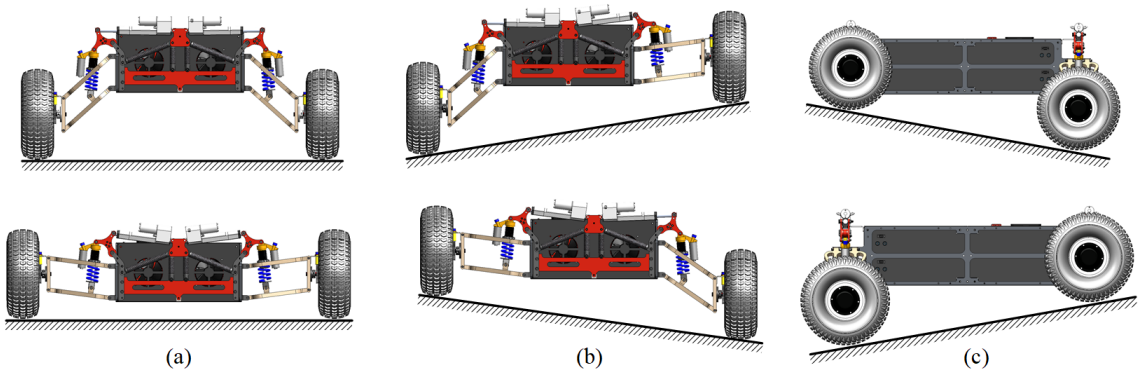

Figure 3.3: Different configuration modes: (a) change the COM height, (b) change the roll angle, (c) change the pitch angle

configuration for improving the robot stability with high speed on rough terrain which is the third design requirement. By including this EAM in the suspension system, the robot can tackle steep slopes and grades by actively and independently adjusting the suspension's height on each wheel of the robot to improve the longitudinal and lateral robot stability.

These requirements governed the design process of the robot, which will be covered in the upcoming sections.

Different robot configuration modes can be achieved based on the operational objectives. The robot's COM height, body roll angle and body pitch angle can be changed as shown in Figure 3.3.

3.3 Mechanical Design

This section presents the mechanical design of the reconfigurable wheeled robot, including the robot body structure and the elastic actuated mechanism. The total weight of the robot should be low to keep the robot inertia as low as possible to meet the agility requirement. The second aspect for robot structure is to be strong to resist the impacts and dynamic loads. This aspect somehow in general conflict with the first aspect for most of the commercial

materials. Therefore, a combination of different material will solve this conflict and reduce the production cost. The materials that used for building the TIGER robot are a combination of aluminum alloys, carbon fiber tubes and stainless steel. Most parts of the robot are made of aluminum 6061 and aluminum 5052 that is widely used due to its excellent strength-to-weight ratio and easy for manufacturing. For some critical parts that need a higher strength, such as the parts that connect the suspension system with the robot's body, we used stainless steel to handle these high loads and resist wear.

3.3.1 Robot Body Structure

The primary function of the robot's body is to carry all of the robot components including batteries, electric and electronic components, different payloads and support the suspension system. The robot's body should be strong and light weight. Therefore, we designed the robot's body to be a rigid modular housing based on the integration between carbon fiber tubes and aluminum shoulders connected together through modular cubes as shown in Figure 3.4. The body housing is developed based on the truss principle to ensure rigidity, light-weight, simple assembling and easy manufacturing. Also, the function of the modular cubes, besides connecting all parts together, it has a great function to connect other components to the chassis for increasing the robot's height and width, which give an advantage to the robot to be modular according to the application and working conditions.

3.3.2 Suspension with Elastic Actuated Mechanism

The most novel parts of the robot structure are the EAM. The design parameters that have been chosen and studied determined the suspension performance. Figure 3.5 shows the suspension layout, where a linear DC motor is connected to the damper through a rocker to actively control the suspension height and isolating the robot's body from external distur-

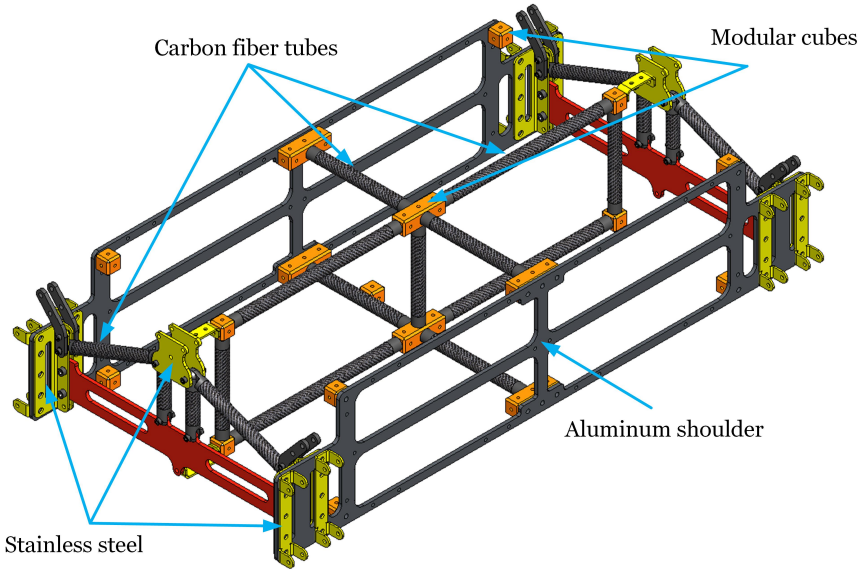

Figure 3.4: Robot body structure. Using the truss principle in designing the body housing, the structure is a combination of carbon fiber tubes and aluminum sheets.

bances that can be caused by terrain and other irregularities. The lower suspension arm is designed with different mounting locations for the damper to modify the initial configuration of the suspension related to the robot's body.

All moving joints are connected through low friction thrust bearings and shoulder screws to reduce the friction as shown in Figure 3.5. The linear motor's stroke is 10 cm maximum length which changes the angle of the suspension arms from -7.5^o to 49^o with respect to the robot's body.

The connection between the in-wheel motor and the suspension system is constructed by a stainless steel flange that fixes the motor's shaft with the lower part of the suspension. To measure the speed of the motor, we fixed a gear to the motor hub with three screws and designed a mounting part for the speed sensor with a distance 2 mm from the gear.

Table 3.2 shows the weight and the material of all suspension parts, these values are measured using an accurate scale.

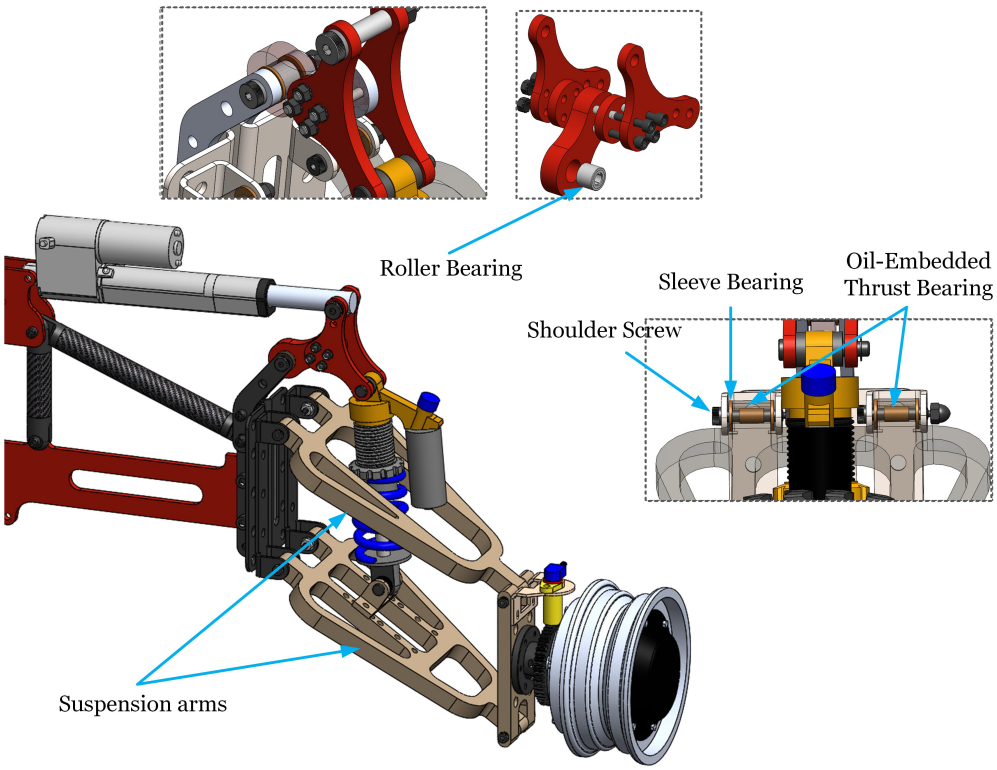

Figure 3.5: Robot suspension system with EAM.

Table 3.2: Suspension parts weight and material

Suspension part	Weight	Material
Lower arm	566 (gm)	Aluminum 6061
Upper arm	552 (gm)	Aluminum 6061
Rocker	200 (gm)	Aluminum 5052
Damper	790 (gm)	—
Linear motor	920 (gm)	—
In-wheel motor	7100 (gm)	—
Suspension flange	502 (gm)	Aluminum 6061
Total weight	9760 (gm)	—

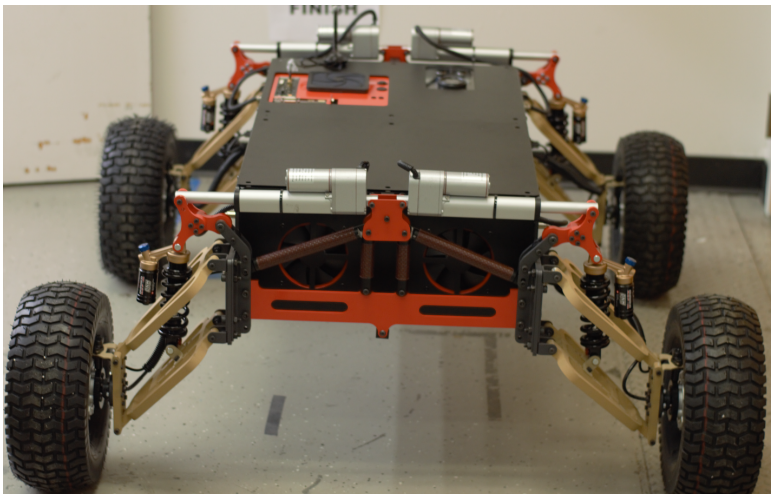

(a) Front view

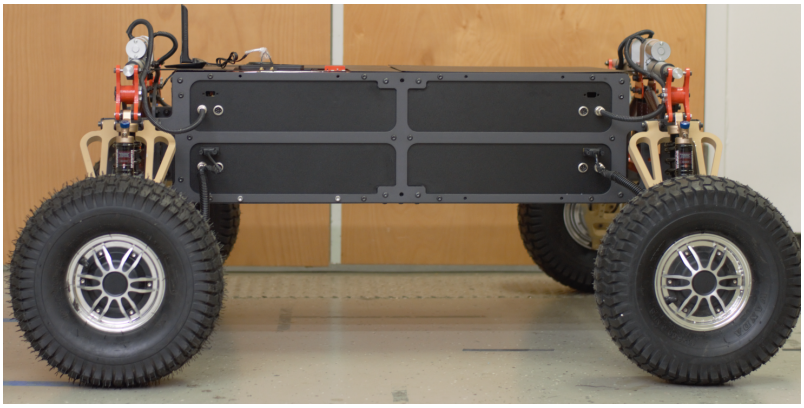

(C) Side view

Figure 3.6: TIGER reconfigurable wheeled robot after assembling all the components.

3.3.3 Assembled Robot

As the robot's body and suspension system has been designed and assembled, Figure 3.6 shows the front and side views of the robot after integrating all the mechanical systems together. All side, top, and bottom covers are attached to the robot's body to protect the electric components inside the chassis and to increase the strength of the robot's body especially enhancing the torsional rigidity. All covers are made from Aluminum sheet 5052 with 1.63 mm thickness.

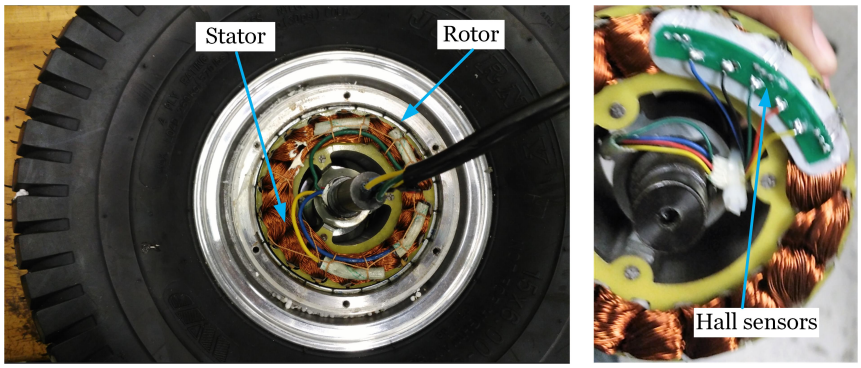

Figure 3.7: Brushless DC motor with 15-inch tire diameter and five hall sensors

3.4 Actuation and Sensory Systems

This section demonstrates the actuation and sensory systems that are used for controlling the robot drivetrain and suspension system. The robot is equipped with four in-wheel brushless DC motors and four linear DC motors for the suspension system. The robot is equipped with 25 sensors: quadrature speed sensors for measuring wheel speeds, potentiometers for measuring suspension stroke, current sensors, voltage sensors, and IMU for measuring robot's body accelerations, angular velocities, and orientations.

3.4.1 In-Wheel Brushless Motor

As discussed in section 3.2, four high-speed brushless DC motors are used for driving the robot with high speed. These motors are in-wheel motors with specifications as listed Table 3.3 and illustrated in Figure 3.7. Two HBL2360 Roboteq controllers are used to control these motors; each Roboteq controller controls the two motors in each side. The motor shaft is connected to the suspension system by a steel flange as shown in Figure 3.8.

Table 3.3: Brushless motor specifications

Rated DC voltage	24 ($Volts$)
Rated power	350 ($Watts$)
Max speed	800 (rmp)
Tire diameter	32.4 (cm)
Feedback sensor	5 hall sensors

3.4.2 Linear DC Motor

Four DC linear motors are used for controlling the suspension system. The motor maximum speed is 9.4 mm/s with a maximum force 667 N. Each motor is equipped with a limit switch and a feedback potentiometer to measure the stroke length. Based on the designed performance of the EAM, the maximum motor stroke is selected to be 7 cm.

3.4.3 Speed Sensor

Each wheel speed of the robot is measured by a Honeywell SNG-QPLA-000 quadrature speed sensor, which is a two-channel sensor for measuring the speed and direction. This sensor is mounted above a gear to the wheel hub by $2:4$ mm and connected to Arduino Mega microcontroller, Figure 3.8 shows a picture of the sensor. The signal from the speed sensor is used for measuring each wheel speed, estimating the wheel slip ratio, and localizing the robot position.

3.4.4 Suspension Position Sensor

As mentioned the linear Dc motor has a potentiometer sensor to measure the stroke length. This potentiometer is used as a feedback sensor for measuring the linear DC motor stroke and control the suspension height. A potentiometer calibration should be done to get the relationship between the stroke length and the digital signal from the potentiometers which

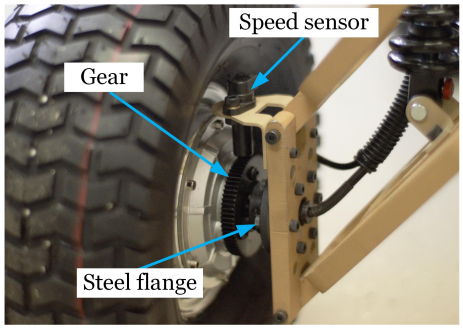

Figure 3.8: Quadrature speed sensor is attached above the hub gear to measure the wheel speed.

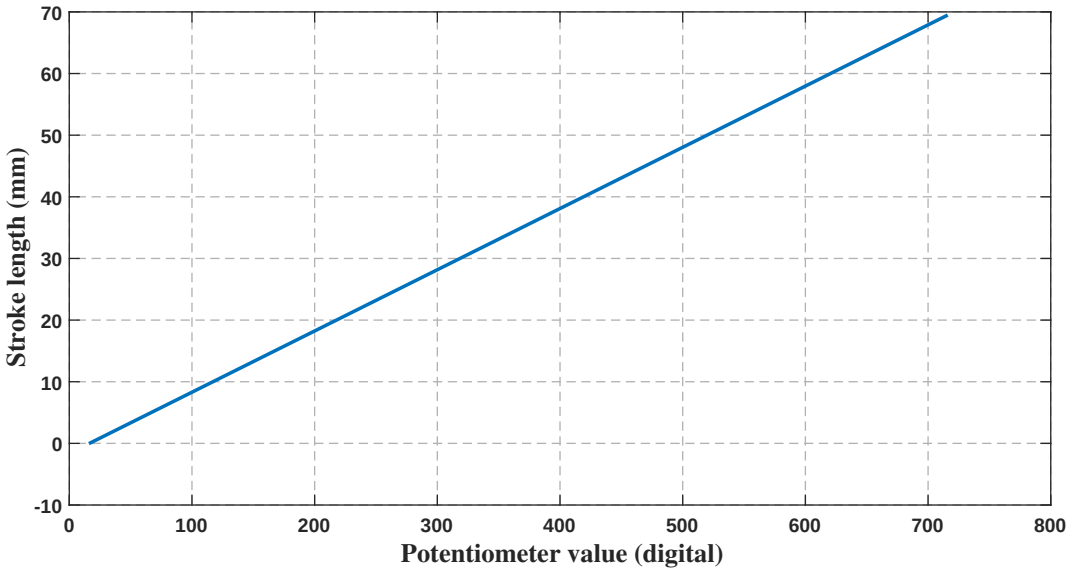

Figure 3.9: Motor stroke length Vs potentiometer value.

will be read by the Arduino Mega microcontroller as shown in Figure 3.9.

3.4.5 Current Sensor

The HBL2360 Roboteq controller that controls the brushless DC motors is equipped with current and voltage sensors for measuring the motors states. With the information of the motor current, we can estimate the rated motor torque as an indication of the resisting force on each tire, which can be used as a feedback sensor for controlling each wheel speed to

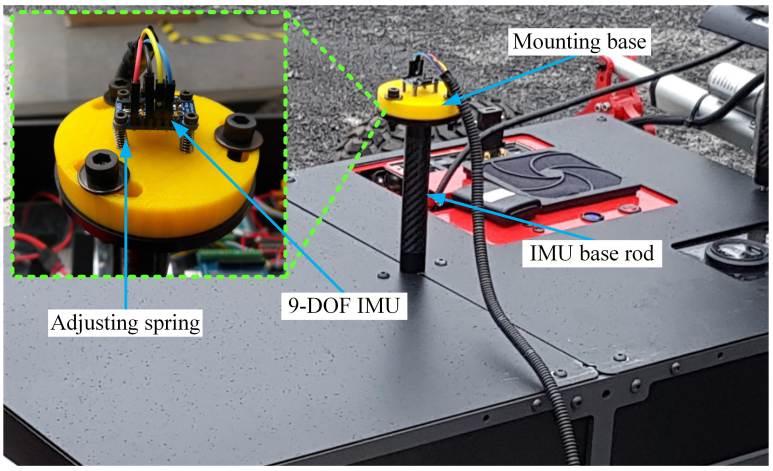

Figure 3.10: Adafruit 9-DOF absolute orientation IMU sensor is mounted on a designed base.

enhance the mobility in loose terrain. With the information of current and voltage, we can estimate the rated power of each motor as illustrated in section 4.4.

3.4.6 IMU

The inertial measurement unit (IMU) is an Adafruit 9-DOF absolute orientation IMU sensor as shown in Figure 3.10. It has a 3-axis accelerometer sensor, a 3-axis gyroscope sensor and a 3-axis magnetometer. This IMU module uses the sensors data to calculate the 3D space orientation. A mounting base is designed to fix the IMU on it. With adjusting springs, we can adjust the initial values of the IMU as a calibration process before executing any algorithm that controls the robot. The IMU data are analyzed by Arduino Nano for computing the robot's body orientation angles, angular accelerations, and the robot linear accelerations.

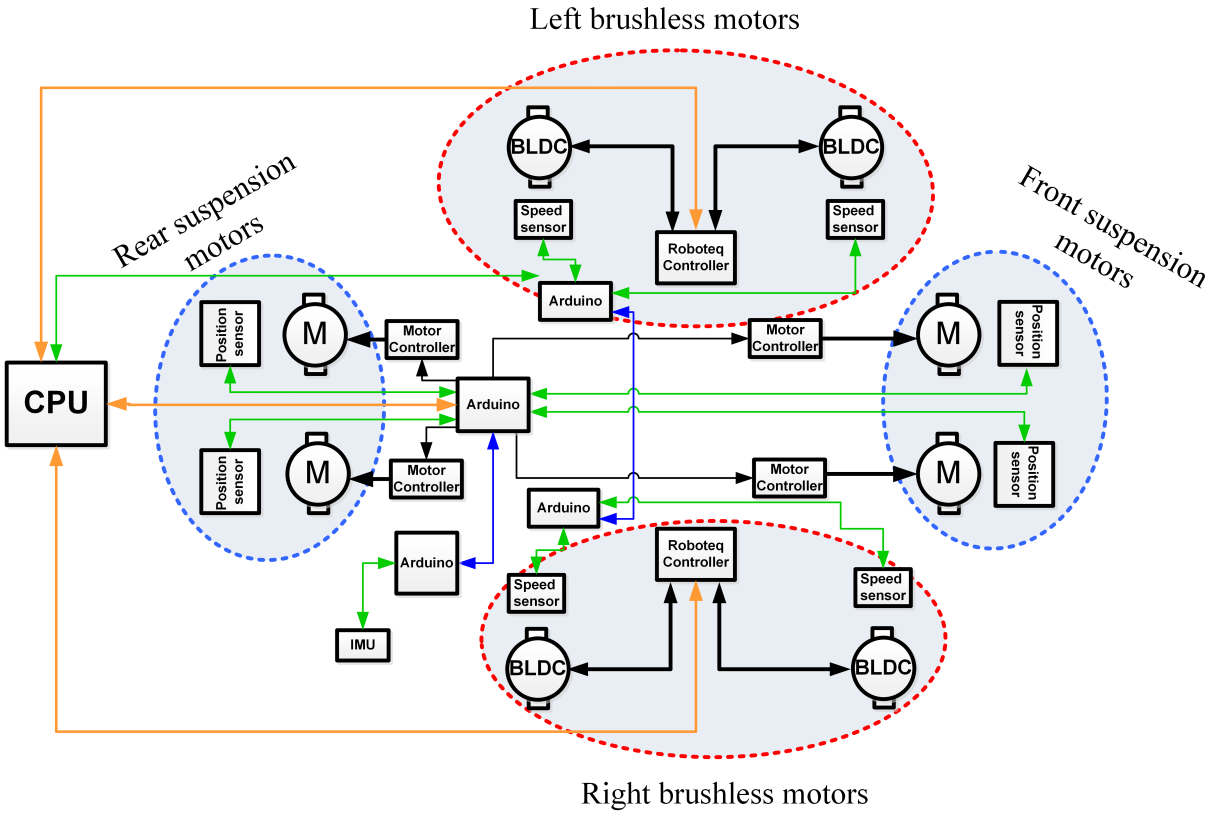

Figure 3.11: Control architecture of the Tiger robot. The black wires represent the voltage, the green wires represent data signals between sensors and microcontrollers, the blue wires are the RS-232 communication buses, and the orange wires are the USB communication signals.

3.5 Robot Control Architecture

The control system of the TIGER robot is shown in Figure 3.11. The control structure consists of the low-level and the high-level control systems; the low-level control systems includes all sensors, all motors, all motor drivers, and the microcontrollers. While the High-level control system consists of the CPU box. A power management circuit is designed to secure enough power for the robot systems; motors, computer, sensors, microcontrollers, and communication. As well as, auxiliary power outputs which can be used as a power source for any payload that may be used on the robot platform as a manipulator.

3.5.1 High-Level Control System

The robot's computer represents the high-level control system, which has the following specifications:

- Intel core i7-7700K processor,
- 32GB RAM,
- 512GB SSD,
- 8GB graphical processing unit (GPU),
- Gigabyte GA-Z170N-WIFI Motherboard.

The computer is running under ROS to calculate all high-level control algorithms and communicate with the low-level control system through USB serial communication. The computer receives all sensors data from the microcontrollers and the motors drivers, then calculate the desired speed for each wheel and the desired suspension configuration and send the desired values to the low-level control system.

An aluminum box had been designed to assemble all computer components and in the same time adapt with the robot's body as shown in Figure 3.12.

3.5.2 Low-Level Control Systems

Three level-control systems had been designed to control the robot speed and the suspension configurations; drivetrain control unit, suspension control unit, and robot' speed control unit. Each control unit connects to the robot's computer to send and receive data.

The drivetrain control unit consists of two HBL2360 Roboteq controllers and four in-wheel brushless motors. This control unit receives the desired speed for each motor and regulates

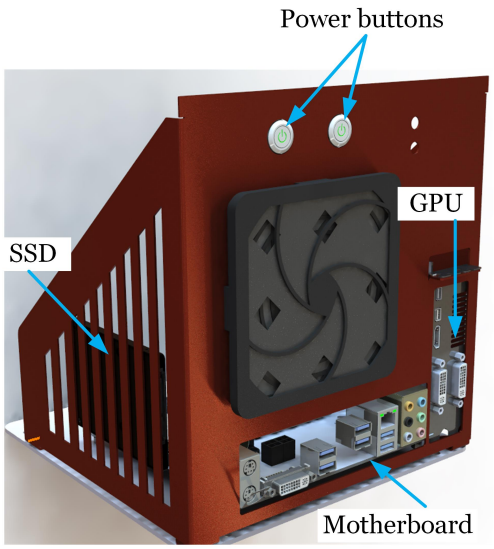

Figure 3.12: Aluminum box was designed to assemble all computer components inside it.

the input voltage to each brushless motor. The Roboteq controller calculates each motor current and voltage value and sends it to the robot's computer.

The suspension control unit consists of Arduino Mega, Arduino Nano, four DC linear motors, four suspension position sensors, and IMU. Arduino Nano receives the IMU data and calculates the orientation angles, angular velocities, and linear accelerations, then send these values to the Arduino Mega through RS-232 serial communication. The Arduino Mega is the main central unit for the suspension control unit, it receives the data from suspension position sensors, receives the data from IMU and controls the suspension motor through the motor drivers as shown in Figure 3.11. All sensors data are sent to the high-level control system through the USB serial communication in the Arduino Mega.

The robot's speed control unit is consists of two Arduino Mega and four speed sensors. This unit calculates each wheel speed and sends these data to the high-level control system.

3.6 Summary

This chapter presented an overview of the robot design paradigm, which discussed in details the robot mechanical design, actuation and sensory systems, and finally the robot's control structure. In the robot mechanical design, the robot's body structure was designed from aluminum shoulders and carbon fiber tubes that connected together through modular cubes to ensure rigidity, light weight and chassis modularity. While the EAM design was designed by connecting a linear DC motor to a damper in series to control the suspension's height. All different motors and sensors that used on the robot had been represented in the section of actuation and sensory systems, followed by the description of the robot control architecture. This included a detailed explanation of the high-level control system and low-level control systems.

Chapter 4

Elastic Actuated Mechanism Modeling, Analysis, and Experimentation

This chapter discusses the robot's suspension system kinematic and dynamic models and the proposed control algorithm for controlling the EAM to improve the quasi-static stability of the robot in rough terrain. This chapter is structured as follows; Section 4.2 describes in detail the linear quarter and full robot kinematic and dynamic models with EAM. In Section 4.3, the design of an observer based on the Kalman filter for estimating the robot states and the Linear Quadratic Regulator (LQR)-based optimal control are presented for the robot with EAM. Section 4.4 provides the results from experiments with three different scenarios. Finally, Section 4.5 concludes and discusses the results.

4.1 Background

Recent years have seen accelerated rate at which robots replace humans in human-centric tasks. As the robot becomes more intelligent, the desired mission is not limited to transportation but extends to manipulation. This yields the wheeled humanoid robot, which has an upper humanoid body on top of a robot for both traveling and manipulation [31, 32, 33]. Because of the high COM location, which is caused by the upper humanoid body, such a wheeled humanoid robot is significantly concerned with stability on uneven surfaces. The robot will flip over if the COM is outside its support polygon.

Past work on the wheeled mobile platform for stability can be classified into two types. In the first, stability is ensured in a passive fashion. These include the increase of weight of the wheeled mobile platform [34] as well as the increase of area of the support polygon [35]. In either way, the COM is located more stably within the support polygon. While the passive control is easy to implement, the range of its applicability is limited by the mechanical design.

The second approach, on the contrary, is the active control. This approach guarantees stability by actively controlling the location of the COM. Numerous publications on the stability of legged humanoid robots belong to this approach [36, 37, 38, 39]. The active control of wheeled mobile platform was studied rather in the context of active suspension of passenger cars [40, 41, 42]. While its effectiveness is obvious, the active suspension has not been implemented into an wheeled robot.

This chapter presents an agile active control of the TIGER reconfigurable wheeled robot with EAM. The robot controls the equipped suspension and minimizes the robot's roll and pitch angles when situated on a non-flat terrain. In order for the control, a full robot motion model and a sensor model of IMU have been developed. The state of the robot is estimated using an observer where the Kalman filter acts as a compensator. An LQR is then designed and used to perform the optimal state-feedback control.

Figure 4.1: The wheeled humanoid robot consists of the TIGER reconfigurable wheeled robot with four EAM and dual arms for high precision manipulation on irregular terrain.

4.2 Elastic Actuated Mechanism Mechanics

In this section, the EAM kinematic and dynamic models are developed for quarter and full robot suspension system. A system description of the platform with EAM will be illustrated; then the kinematic and dynamic models will be studied.

4.2.1 System Description

The robot mainly consists of a body connected to the wheels through an EAM as shown in Figure 4.2. The wheel is supported to the body through a spring-damper system connected in series with a linear DC geared motor. As the linear DC motor moves, the relative distance between the robot's body and the wheel will change. The kinematics relationship between the linear actuator stroke and the suspension travel is slightly nonlinear as shown in Figure 4.3. So, a linear robot model is utilized for designing an optimal control scheme to control the robot attitude.

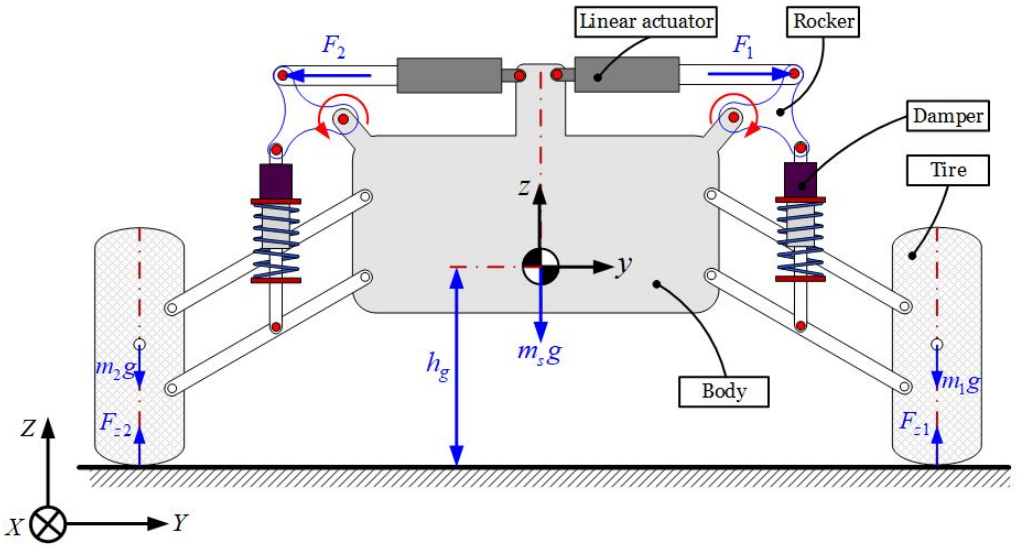

Figure 4.2: Schematic of the EAM applied to the robot.

An IMU is placed on the top of the platform for measuring the vertical acceleration, roll and pitch angular velocities, and roll and pitch angles. The linear actuator has a potentiometer for measuring the stroke velocity and length.

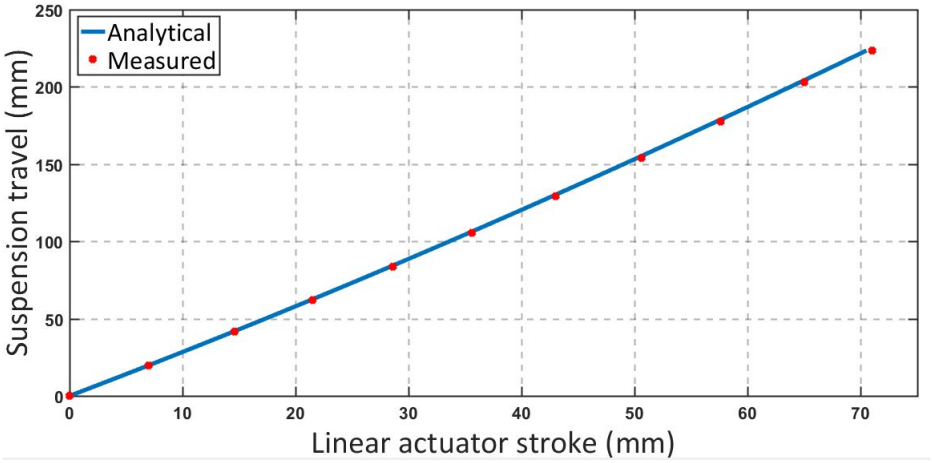

Figure 4.3: Geometric relationship between the linear actuator stroke and the suspension travel; kinematics solution (blue) and experimental measurement (red).

4.2.2 Elastic Actuated Mechanism Kinematic Model

The kinematic model of the suspension system is described with five bodies and 15 generalized coordinates that representing the suspension mechanism as shown in Figure 4.4. The mechanism has one DOF with 14 kinematic constraint equations ($\Phi^K = 14$) and one driving constraint ($\Phi^D = 1$). The mechanism global coordinate is located at the front left corner of the model free-body digram, and each link has its local coordinate as illustrated in Figure 4.4.

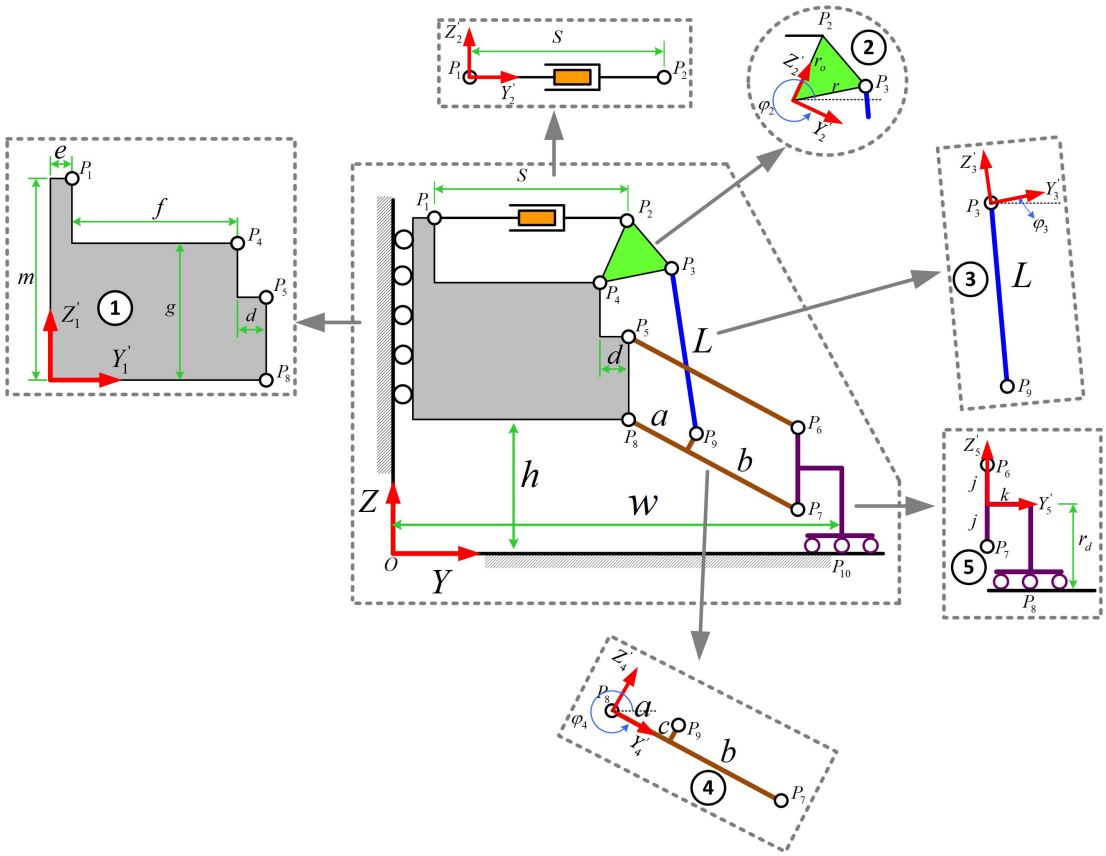

Figure 4.4: Free-body digram of the EAM for kinematic analysis

Assumption 1. The damper is assumed as a rigid body, link 3, between the rocker, link 2, and the suspension lower arm, link 4 .

Based on Assumption 1 the generalized coordinates are;

$$q = [r_i^T, \phi_i]^T, \quad i = 1:5, \tag{4.1}$$

and the complete constraint vector can be described as follow [43]:

$$\Phi = \begin{bmatrix} \Phi^K \\ \Phi^D \end{bmatrix} = \begin{bmatrix} Y_1' \\ \phi_1 \\ r_1^{P_4} - r_2^{P_4} \\ r_1^{P_8} - r_4^{P_8} \\ r_2^{P_3} - r_3^{P_3} \\ r_3^{P_9} - r_4^{P_9} \\ r_4^{P_7} - r_5^{P_7} \\ \phi_5 \\ Z_5' - r_d \\ S^2 - (r_2^{P_2} - r_1^{P_1})^T (r_2^{P_2} - r_1^{P_1}) \end{bmatrix}. \tag{4.2}$$

where, $S = 244 + 9.4t$ (mm) for the linear actuator moves with maximum speed.

The velocity and acceleration equations can be obtained as:

$$\Phi_q \dot{q} = -\Phi_t, \tag{4.3}$$

$$\Phi_q \ddot{q} = -[(\Phi_q \dot{q})_q \dot{q} + 2\Phi_{qt}\dot{q} + \Phi_{tt}]. \tag{4.4}$$

By solving the Differential Algebraic Equation (DAE) in (4.2), the analytical results of the suspension system is demonstrated in Figure 4.5. As the stroke of the actuator increases, the robot's ground clearance will increase while the wheel track will decrease.

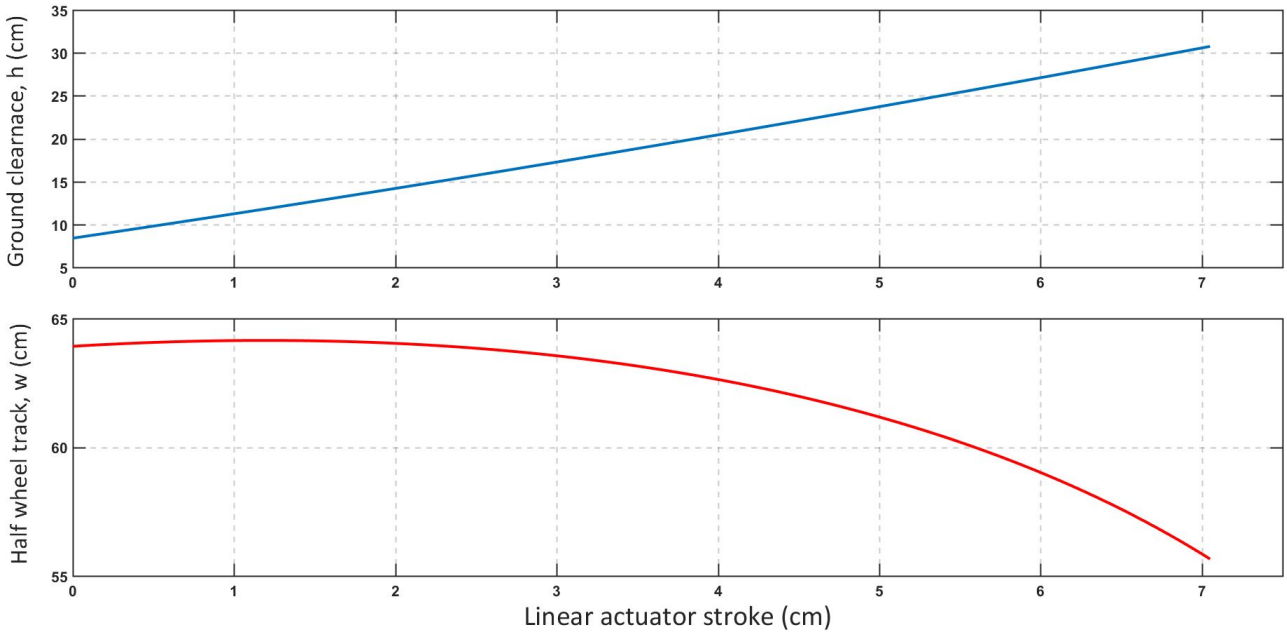

Figure 4.5: Geometric relationship between the linear actuator stroke and the robot ground clearance (blue), and wheel track(red).

4.2.3 Linearized Elastic Actuated Mechanism Dynamic Model

The EAM dynamic model is described as a mass-spring-damper system with 2-DOF as shown in Figure 4.6. The tire is represented as a mass, m_u, supported to the ground through a linear spring with stiffness K_t. The shock absorber is illustrated as a spring-damper unite, K_s, C_s which supports the robot's body, m_s with an active force, F_a.

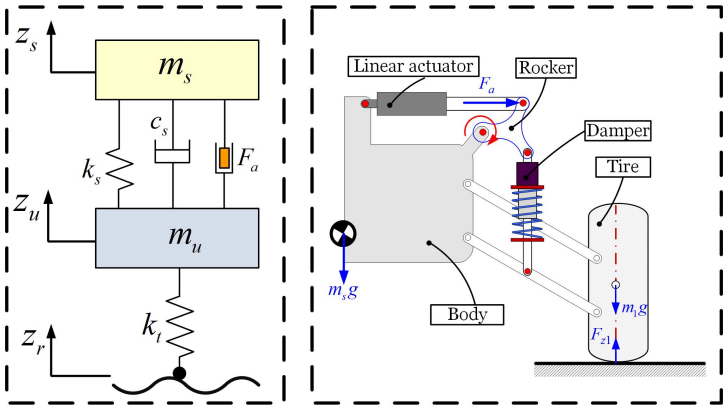

Figure 4.6: Linearized actuated suspension system

The dynamic equations of the system can be driven as follow;

$$\begin{aligned} m_s\ddot{Z}_s &= K_s(Z_u - Z_s) + C_s(\dot{Z}_u - \dot{Z}_s) + F_a, \\ m_u\ddot{Z}_u &= -K_s(Z_u - Z_s) - C_s(\dot{Z}_u - \dot{Z}_s) + K_t(Z_r - Z_u) - F_a. \end{aligned} \tag{4.5}$$

The states, input and output vectors are as follow;

$$\begin{aligned} X &= \begin{bmatrix} Z_s & \dot{Z}_s & Z_u & \dot{Z}_u \end{bmatrix}^T, \\ U &= \begin{bmatrix} F_a & Z_r \end{bmatrix}^T, \\ y &= \ddot{Z}_s \end{aligned}$$

With

$$\begin{bmatrix} A & B \\ C & D \end{bmatrix} = \begin{bmatrix} 0 & 1 & 0 & 0 & 0 & 0 \\ \frac{-K_s}{m_s} & \frac{-C_s}{m_s} & \frac{K_s}{m_s} & \frac{C_s}{m_s} & \frac{-1}{m_s} & 0 \\ 0 & 0 & 0 & 1 & 0 & 0 \\ \frac{K_s}{m_u} & \frac{C_s}{m_u} & \frac{-K_s-K_t}{m_u} & \frac{-C_s}{m_u} & \frac{1}{m_u} & \frac{K_t}{m_u} \\ \frac{-K_s}{m_s} & \frac{-C_s}{m_s} & \frac{K_s}{m_s} & \frac{C_s}{m_s} & \frac{-1}{m_s} & 0 \end{bmatrix}.$$

4.2.4 Full Robot Dynamic Model

A linear robot dynamic model with 7-DOF is developed for optimal control as shown in Figure 4.7. The model consists of a robot's body with 3-DOF in the vertical Z_s-axis (bounce), rotation about X_s-axis (roll) and rotation about Y_s-axis (pitch), with four suspension systems at each corner which have 1-DOF in the vertical directions Z_1, Z_2, Z_3, Z_4 at front left, front right, rear left and rear right respectively.

The dynamic equations can be derived using the Newton's second law as follows [44, 45, 46,

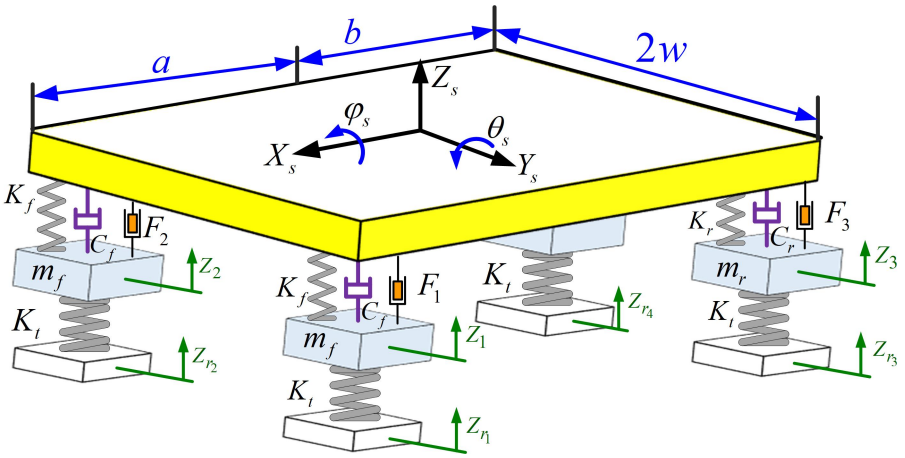

Figure 4.7: The full robot model with actuated suspension system.

47],

$$
\begin{aligned}
m_s\ddot{Z}_s &= F_{fl} + F_{fr} + F_{rl} + F_{rr},\\
I_y\ddot{\theta}_s &= -aF_{fl} - aF_{fr} + bF_{rl} + bF_{rr},\\
I_x\ddot{\phi}_s &= wF_{fl} - wF_{fr} + wF_{rl} - wF_{rr},\\
m_f\ddot{Z}_1 &= -F_{fl} - K_t(Z_1 - Z_{r_1}),\\
m_f\ddot{Z}_2 &= -F_{fr} - K_t(Z_2 - Z_{r_2}),\\
m_r\ddot{Z}_3 &= -F_{rl} - K_t(Z_3 - Z_{r_3}),\\
m_r\ddot{Z}_4 &= -F_{rr} - K_t(Z_4 - Z_{r_4}).
\end{aligned}
\tag{4.6}
$$

where m_s is the mass of the robot's body, I_x is the roll moment, I_y is the pitch moment of inertia about the center of mass, ϕ_s, θ_s are the roll and pitch angles, a, b are the COM locations of the front and rear tires, $2w$ is the wheel track, m_f, m_r stand for the tire mass on front and rear respectively, K_t is the tire spring stiffness, $Z_{r_1}, Z_{r_2}, Z_{r_3}, Z_{r_4}$ are the road displacements at front left, front right, rear left and rear right respectively, $F_{fl}, F_{fr}, F_{rl}, F_{rr}$ are the forces generated by the spring-damper system at front left, front right, rear left and rear right respectively, and F_1, F_2, F_3, F_4 are the linear actuators forces at the front left, the front right, the rear left and the rear right respectively.

The forces are defined as follows,

$$\begin{aligned} F_{fl} &:= -K_f(Z_{fl} - Z_1) - C_f(\dot{Z}_{fl} - \dot{Z}_1) + F_1, \\ F_{fr} &:= -K_f(Z_{fr} - Z_2) - C_f(\dot{Z}_{fr} - \dot{Z}_2) + F_2, \\ F_{rl} &:= -K_r(Z_{rl} - Z_3) - C_r(\dot{Z}_{rl} - \dot{Z}_3) + F_3, \\ F_{rr} &:= -K_r(Z_{rr} - Z_4) - C_r(\dot{Z}_{rr} - \dot{Z}_4) + F_4, \end{aligned} \tag{4.7}$$

where K_f is the front spring stiffness and K_r is the rear spring stiffness, C_f, C_r are the front and the rear shock absorber damping coefficients.

Assuming small angles θ_s and ϕ_s, $\sin\theta_s \approx \theta_s$, $\sin\phi_s \approx \phi_s$, the dynamic vertical displacements of the robot's body corners can be written as,

$$\begin{aligned} Z_{fl} &:= Z_s + w\phi - a\theta, \\ Z_{fr} &:= Z_s - w\phi - a\theta, \\ Z_{rl} &:= Z_s + w\phi + b\theta, \\ Z_{rr} &:= Z_s - w\phi + b\theta. \end{aligned} \tag{4.8}$$

For simplicity let us use the following state-space assignments,

$$\begin{aligned} X_1 &:= Z_s, & X_3 &:= \theta_s, & X_5 &:= \phi_s, & X_7 &:= Z_1, \\ X_2 &:= \dot{Z}_s, & X_4 &:= \dot{\theta}_s, & X_6 &:= \dot{\phi}_s, & X_8 &:= \dot{Z}_1, \\ X_9 &:= Z_2, & X_{11} &:= Z_3, & X_{13} &:= Z_4, & & \\ X_{10} &:= \dot{Z}_2, & X_{12} &:= \dot{Z}_3, & X_{14} &:= \dot{Z}_4. & & \end{aligned}$$

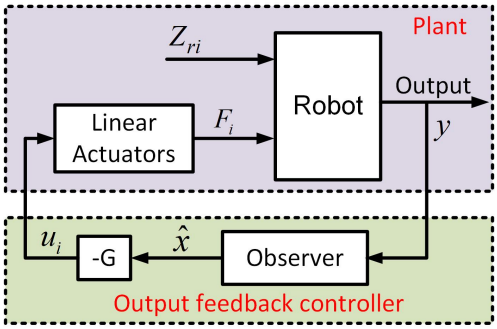

Figure 4.8: The optimal control diagram for estimating the robot states, observer, and control the suspension system, LQR, to stabilize the body attitude.

The state-space assignments rewrite (4.6)-(4.8) as follows,

$$\begin{aligned} \dot{X} &= AX + B_e Q + B_f F, \\ y &= CX + D_e Q + D_f F, \end{aligned} \tag{4.9}$$

where,

$$\begin{aligned} X &= \begin{bmatrix} X_1 & X_2 & X_3 & \dots & X_{12} & X_{13} & X_{14} \end{bmatrix}^T, \\ y &= \begin{bmatrix} \ddot{Z}_s & \dot{\theta}_s & \dot{\phi}_s & \theta_s & \phi_s \end{bmatrix}^T, \\ Q &= \begin{bmatrix} Z_{r_1} & Z_{r_2} & Z_{r_3} & Z_{r_4} \end{bmatrix}^T, \\ F &= \begin{bmatrix} F_1 & F_2 & F_3 & F_4 \end{bmatrix}^T. \end{aligned}$$

4.3 Stability-Based Reconfiguration Control

Optimization-based stability control consists of two main parts; (1) design an observer for estimating the robot states, (2) based on the estimated states, the LQR will optimally control the linear actuators to reduce the robot's body accelerations; bounce, roll, and pitch accelerations as shown in Figure 4.8.

4.3.1 Observer Design

The observer is designed as an optimal output tracking control for estimating the actual states. Where, the Kalman filter is acting as a compensator to drive the observer states to the actual states by minimizing the error between IMU signals and the observer output.

Using (4.10) and (4.11), the observer dynamics are given by,

$$\dot{\hat{X}} = A\hat{X} + B_e Q + B_f F \tag{4.10}$$

$$\hat{y} = C\hat{X} + D_e Q + D_f F \tag{4.11}$$

We assume Q is a disturbance input for the actual plant of the robot and it is not available for measurement. We can then rewrite (4.10) and (4.11) as,

$$\dot{\hat{X}} = A\hat{X} + B_f F + L(y - \hat{y}) \tag{4.12}$$

$$\hat{y} = C\hat{X} + D_f F \tag{4.13}$$

Where L is the Kalman gain added to the observer states to achieve $y \to \hat{y}$.

It is desired to obtain the optimal value L which minimizes the following cost function over infinite horizon,

$$J_L = \frac{1}{2}\int_t^\infty [(y - \hat{y})^T M (y - \hat{y}) + L^T R L] d\tau, \forall x \; and \; t > 0 \tag{4.14}$$

where $R \succ 0$, $M \succeq 0$ are symmetric matrices. (4.14) can be solved in terms of the constraints (4.12) and (4.13) using optimal control theory [48, 49].

The Hamiltonian for the system is,

$$H_L(\hat{x}, L, \lambda) = \lambda^T[A\hat{X} + B_f F + L(y - \hat{y})] + \frac{1}{2}[(y - \hat{y})^T M(y - \hat{y}) + L^T RL], \forall x \ , \ L \tag{4.15}$$

The optimal control can be found by using the stationarity condition $\frac{\partial H_L}{\partial L} = 0$ as follows,

$$L^* = -R^{-1}B_f^T\lambda \tag{4.16}$$

Where,

$$\lambda = P\hat{x} - g \tag{4.17}$$

Solving the Algebraic Riccati Equation (ARE) to get P and g:

$$PA + A^T P - PB_f R^{-1}B_f^T P + C^T MC = 0 \tag{4.18}$$

$$g = -(A^T - PB_f R^{-1}B_f^T)^{-1}(C^T My_m) \tag{4.19}$$

4.3.2 State-Feedback Control Design

The objective of the LQR optimization is to stabilize the robot pitch and roll angles by including the states in the weighted matrix M. In other words, the goal is to find a controller $F = [F_1, F_2, F_3, F_4]^T$ that minimizes the cost function,

$$J_F(x(0); F) = \frac{1}{2}\int_0^\infty [\hat{x}^T M\hat{x} + F^T RF]dt \tag{4.20}$$

which can be solved in terms of the constraints (4.12) using the ARE (4.18) to find G,

$$F = -G\hat{x} \tag{4.21}$$

where:

$$G = R^{-1}B_f^T P \tag{4.22}$$

$$A^T P + P\hat{x} - PB_f R^{-1} B^T P + M = 0 \tag{4.23}$$

Based on the output feedback controller design as shown in Figure 4.8, the augmented system will be,

$$\begin{bmatrix} X \\ \hat{X} \end{bmatrix} = \underbrace{\begin{bmatrix} A & -B_f G \\ LC & \hat{A} - L\hat{C} - \hat{B}_f G - L(D_f - \hat{D}_f)G \end{bmatrix}}_{A_{aug}} \begin{bmatrix} X \\ \hat{X} \end{bmatrix} + \underbrace{\begin{bmatrix} B_e \\ 0 \end{bmatrix}}_{B_{aug}} \begin{bmatrix} Z_{r_1} \\ Z_{r_2} \\ Z_{r_3} \\ Z_{r_4} \end{bmatrix} \tag{4.24}$$

$$\begin{bmatrix} y \\ \hat{y} \end{bmatrix} = \underbrace{\begin{bmatrix} C & -D_f G \\ 0 & \hat{C} - \hat{D}_f G \end{bmatrix}}_{C_{aug}} \begin{bmatrix} X \\ \hat{X} \end{bmatrix} + \underbrace{\begin{bmatrix} D_e \\ 0 \end{bmatrix}}_{D_{aug}} \begin{bmatrix} Z_{r_1} \\ Z_{r_2} \\ Z_{r_3} \\ Z_{r_4} \end{bmatrix} \tag{4.25}$$

4.4 Experimental Results

This section discusses the experimental results to show the effectiveness of the proposed approach for stabilizing the robot on irregular terrain. The TIGER robot has been designed and developed in Computational Multiphysics Systems Laboratory for use in real-world

tests as shown in Figure 4.9. The suspension position sensors and IMU are used in feedback controller to control the pitch and roll angles based on the controller objectives.

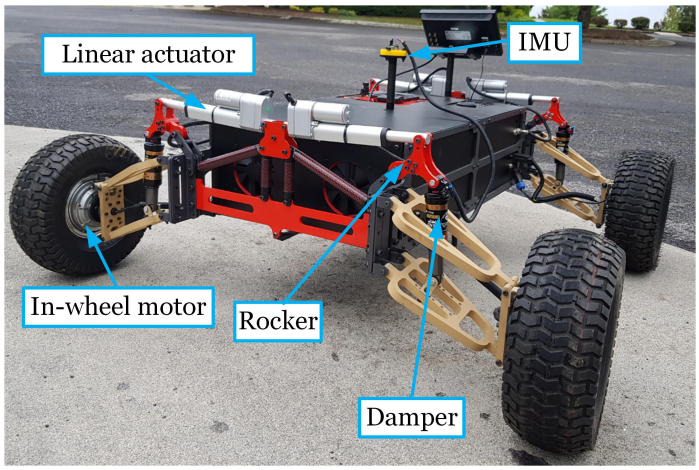

Figure 4.9: TIGER reconfigurable robot which is used for real-world tests.

4.4.1 Performance Analysis For Shaking Plate

In this test, the robot is placed on a wooden plate which is over a cylindrical tube. This arrangement will introduce roll and pitch motion of the wooden plate to simulate the change of terrain level under the robot.

First, rotating the wooden plate as a step input about the robot x-axis (roll). Figure 4.10 demonstrates that the controller succeeds to minimize the roll and pitch angles by controlling the linear actuators velocities based on estimating the robot states. The observer estimates the change of the robot's body pitch and roll angles from the IMU, then these angles errors are compensated by the LQR controller. The LQR sends the velocity value for each linear actuator which is handled by a Proportional–Integral–Derivative (PID) controller for each actuator with the information of the suspension position sensor as a feedback sensor. Due to the heavy weight of the robot with respect to the wooden plate, there is a deflection of the plate which creates a small pitch angle during the test. But, these uncertainties are handled

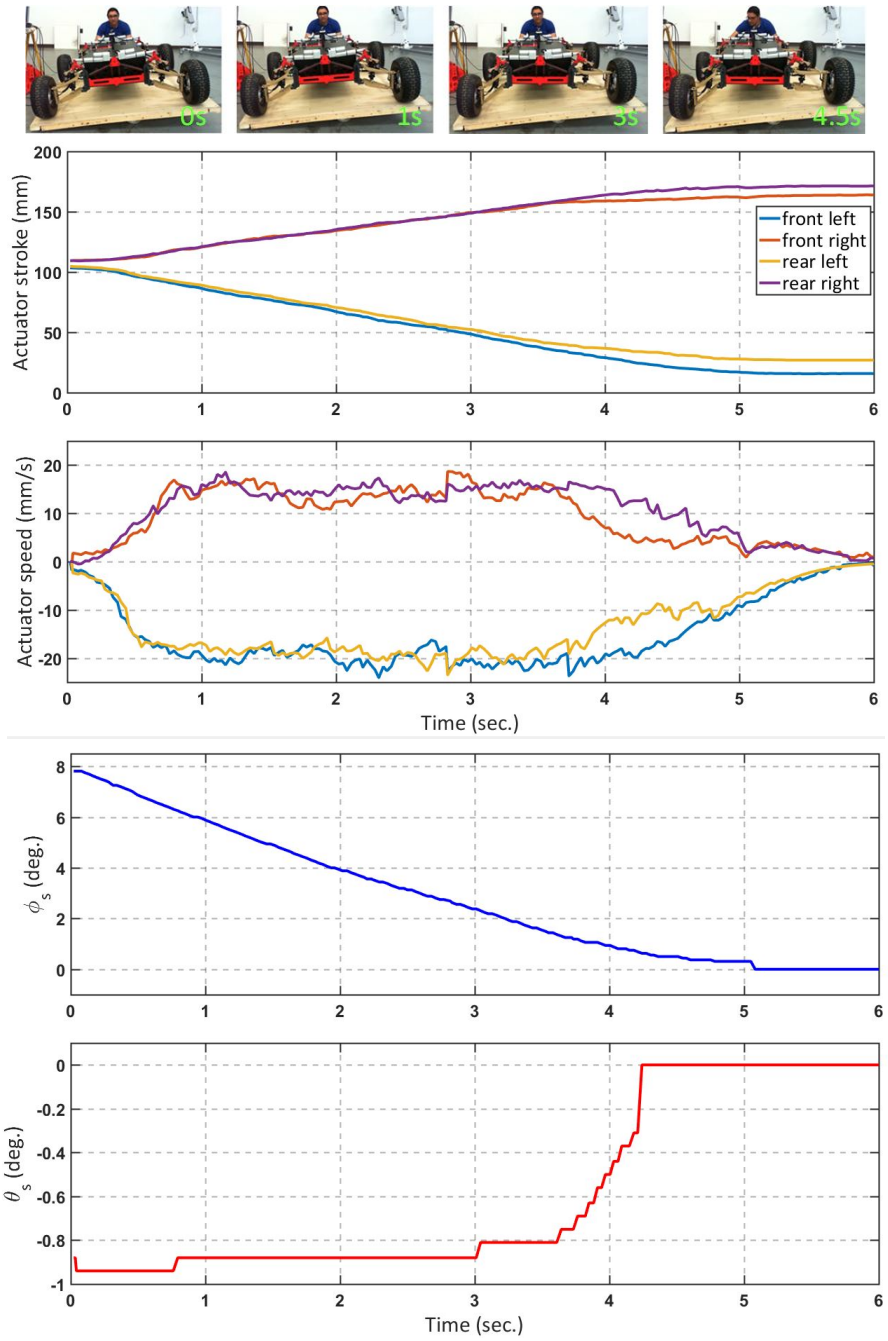

Figure 4.10: Step input test results. The time frames for the TIGER platform for stabilizing its attitude are depicted in the top, the linear actuator stroke and velocity (middle), and the platform roll and pitch angles (bottom).

by the controller.

Secondly, a harmonic excitation is applied to the wooden plate for evaluating the robustness of the observer and the controller to mitigate different road disturbances. Figure 4.11 illustrates the robustness of the output feedback controller in stabilizing the robot with good accuracy without accumulating any errors.

The LQR is an upper controller with the PID as lower controllers succeed to compensate the external disturbance during the harmonic excitation for stabilizing the robot's body as a controller objective.

4.4.2 Performance Analysis For Moving Over Uneven Terrain

In terms of evaluating the performance of the proposed framework for moving over uneven terrain, we selected an open area with different slopes for this test. The experimental results are depicted in Figure 4.12, where the robot was moving at a fixed speed and controlling the suspension system to reduce the platform roll and pitch angles.

4.4.3 Performance Analysis For Moving on Rough Terrain Slopes

In this test, we evaluate the robot performance for its capabilities to traverse slope without slipping and its ability to change the robot's COM location. In this test, we measured each wheel slip and consumed power. Figure 4.13 shows the TIGER robot when it is trying to traverse rough terrain slope.

Two case studies are demonstrated in this experiment:

- The TIGER robot traverses the slope with passive configuration,
- The TIGER robot traverses the slope with active configuration.

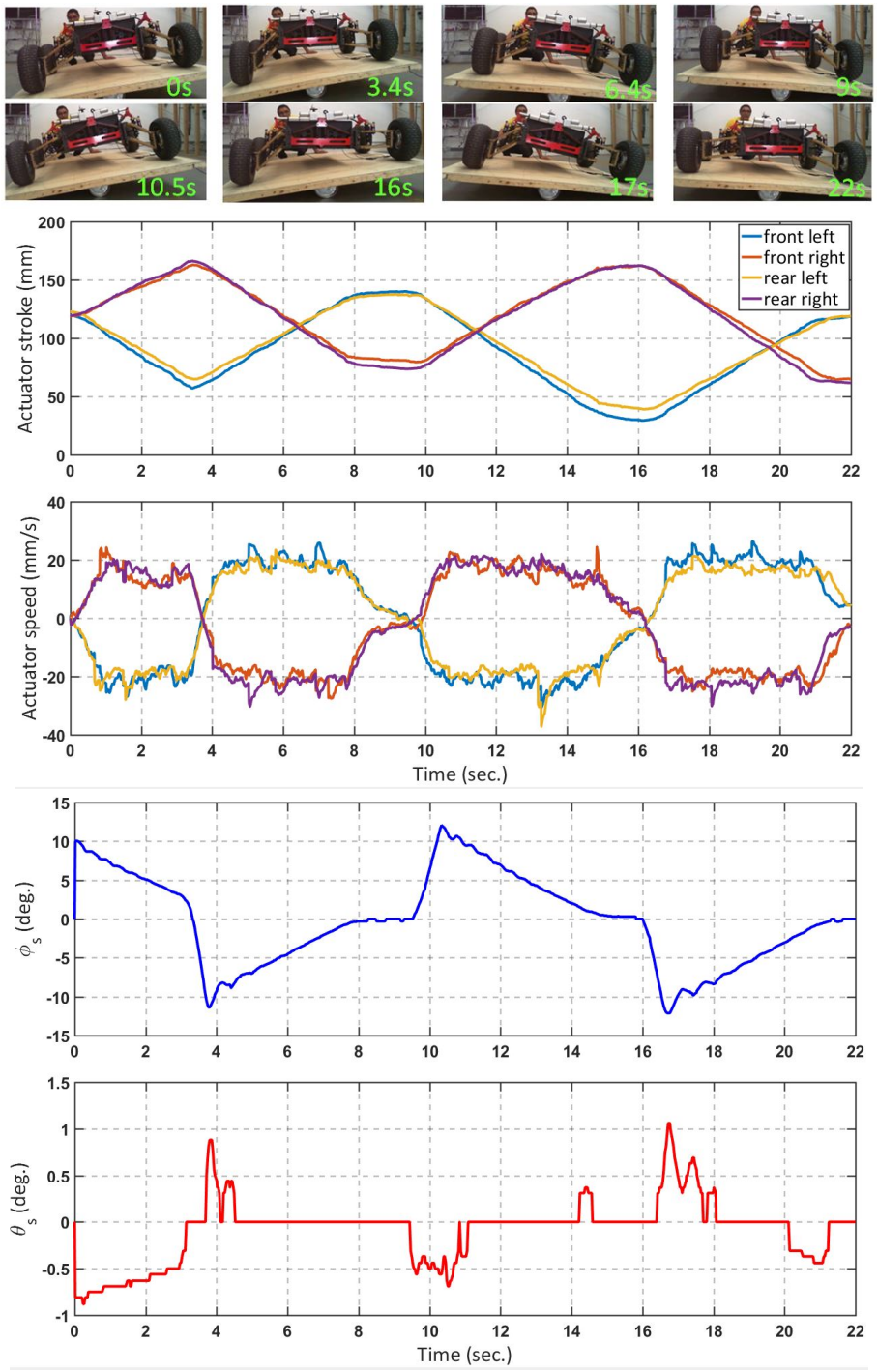

Figure 4.11: Harmonic excitation test results; the controller optimally control the robot dynamics for stabilizing the roll and pitch angles.

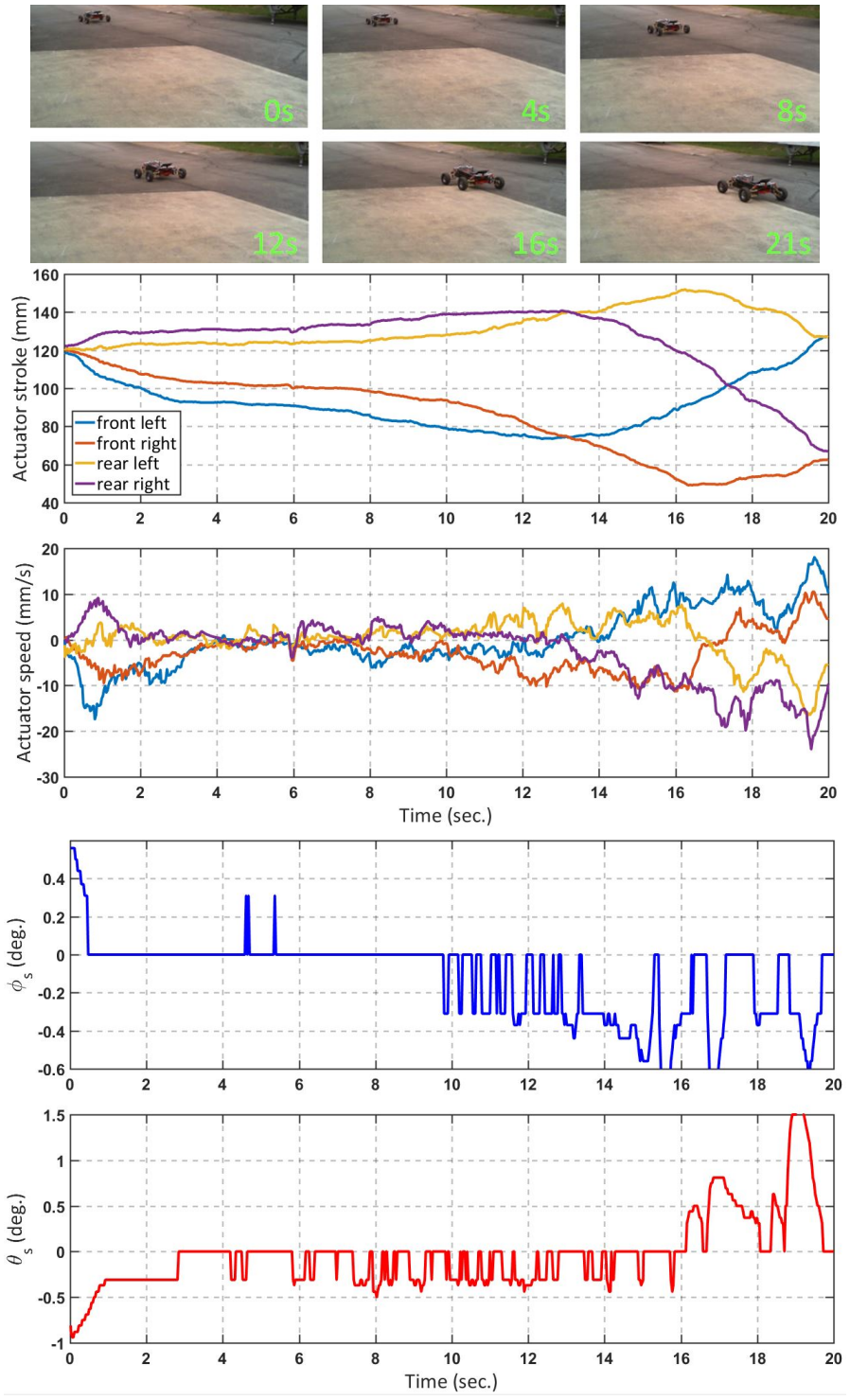

Figure 4.12: TIGER is moving over uneven terrain.

Figure 4.13: TIGER reconfigurable robot is traversing loose slope.

For evaluating the robot performance with passive configuration, Figure 4.14 shows the results of the robot during traversing slope, in this test two of the robot tires had been trapped in soil with high slippage. The front left and rear right tires lost the contact with the terrain and experience high slippage, then the robot failed to traverse the terrain. In this test, most of the robot's weight is supported by rear left tire only; therefore the tractive efficiency for the other tires becomes very low which affects the total performance of the robot.

On the other hand, for evaluating the robot performance with active configuration, Figure 4.15 shows the results with the active configuration of the suspension system to ensure that all the tires will be in contact with the terrain and try to distribute the robot's weight on all the tires equally by moving the robot's COM location. It can be seen from Figure 4.15 that the suspension had been configured based on the IMU data to enhance the traction efficiency. The robot succeeded to traverse this trough slope with minimum power consumption and less time with respect to the passive scenario.

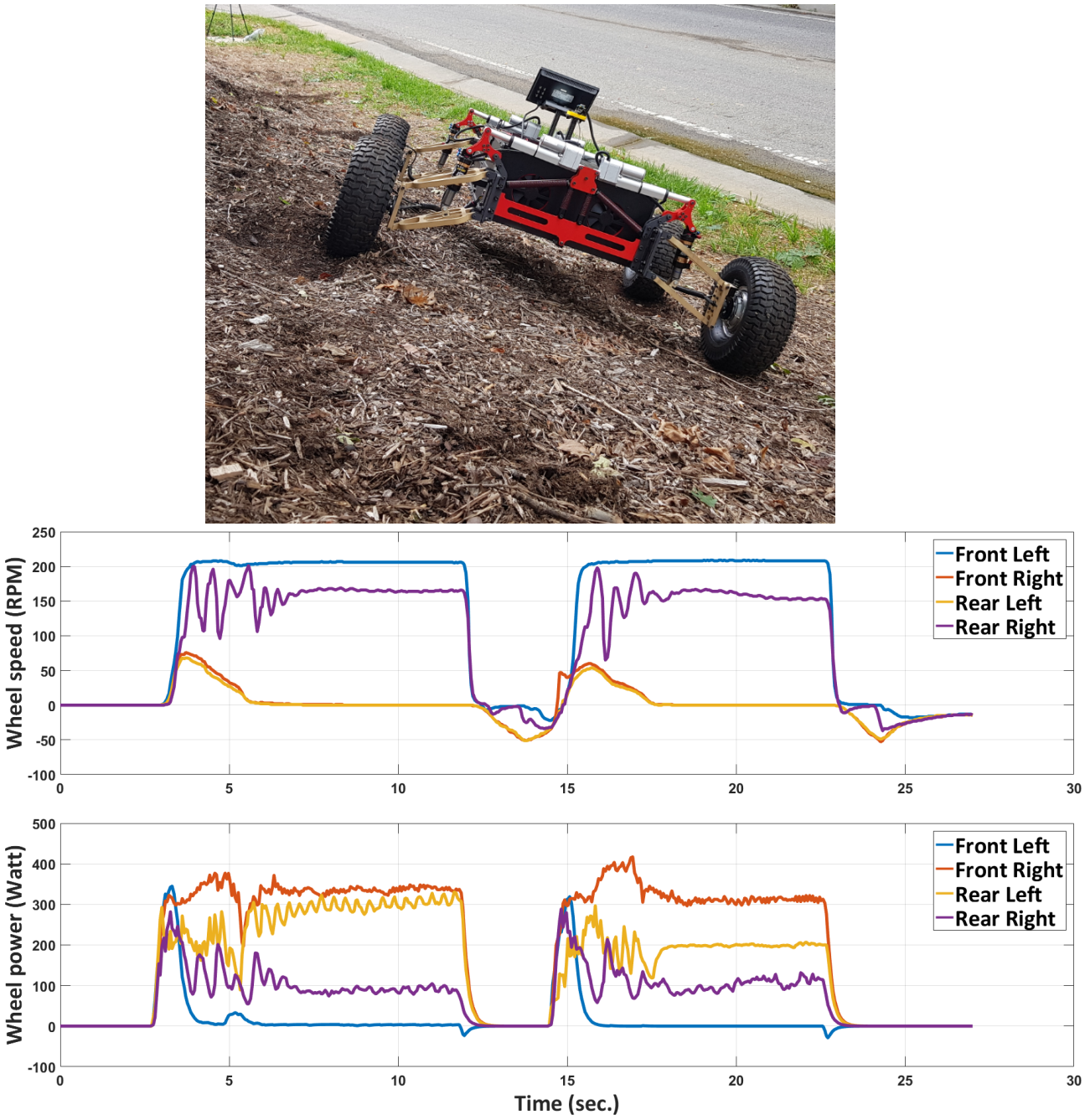

Figure 4.14: TIGER is traversing loose slope with passive configuration.

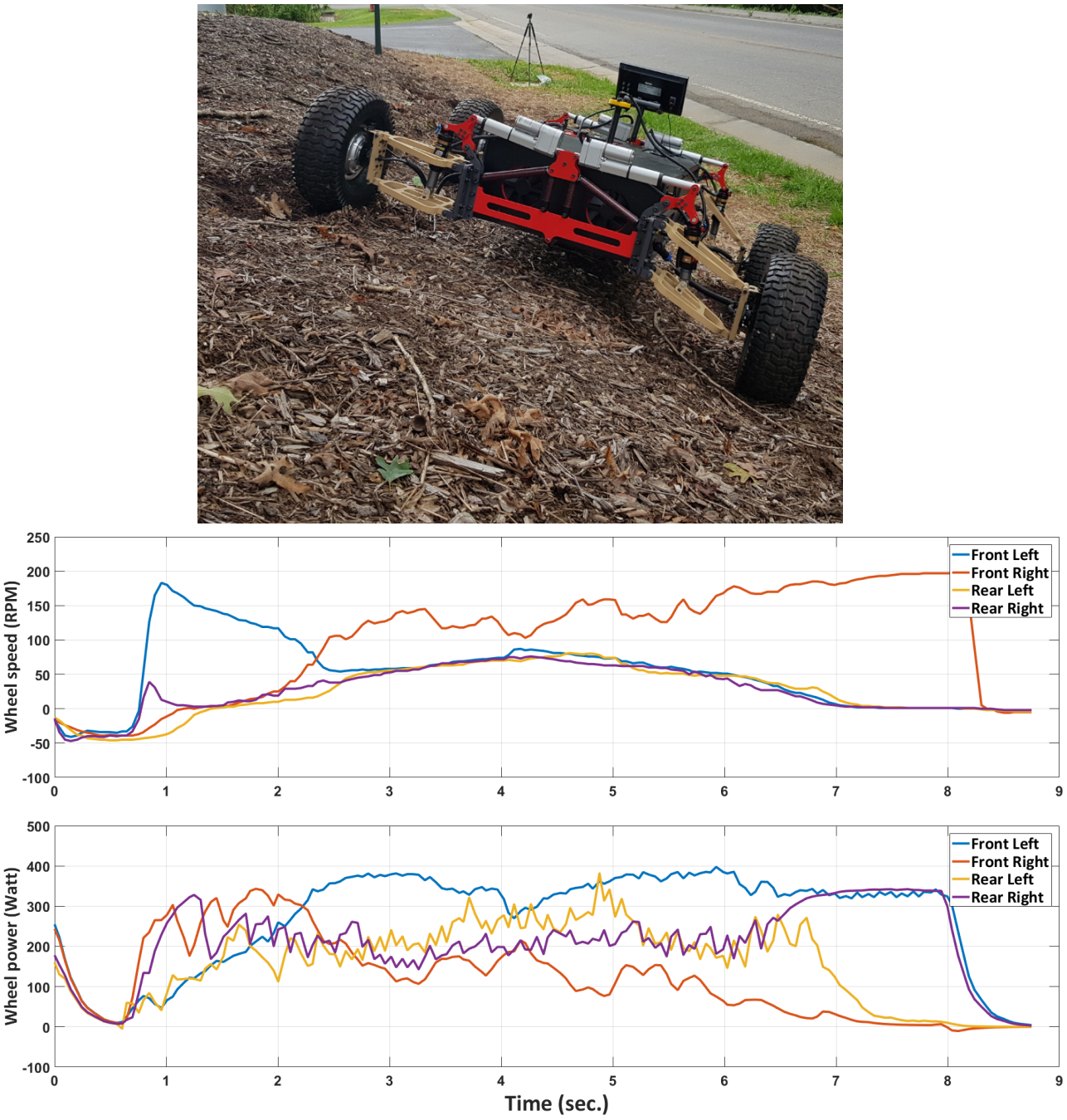

Figure 4.15: TIGER is traversing loose slope with active configuration.

4.5 Summary

This chapter has presented a detailed EAM kinematic and dynamic models for analysis and performance evaluation. A full robot dynamic model with actuated suspension sys-

tem has been demonstrated. Then designing an output-feedback controller by considering the duality of Kalman filter in estimating plant states with the LQR as a state-feedback controller. Finally, experimental results are presented to demonstrate the efficiency and quantified performance of the proposed framework for distributing the robot's weight on all the tires equally. The application of the control approach for stabilizing the robot's body and distributing the robot's weight has been demonstrated with a shaking plate test and traversing rough terrain slopes.

Chapter 5

Robot Dynamic Modeling, Control, and Analysis

5.1 Robot Dynamics

The robot's response during certain maneuver is controlled by the forces imposed on the robot from the tire-ground contact conditions and gravitational effect. For the theoretical analysis of the robot dynamics, the equations of motion must be known, and the physical interactions between the various subsystems must be written in the form of mathematical expressions. The robot and its subsystems are modeled to determine the forces produced by each of these sources under particular maneuvers.

In this research, the robot dynamics model is represented with 14-DOF. Where, it is including the dynamic behaviors of the robot's body, suspension system, forces and moments on the tires.

The robot consists of five rigid bodies; robot's body and four tires where the tires are connected to the robot's body with an EAM. The tire are considered as a linear spring

where the calculation of tire forces are based on Pacejke tire model [50].

Remark 5.1. Note that the Pacejke tire model that used for calculating the robot tire forces is valid for on-road dynamic simulations only. Other off-road tire models can be used for rough terrain dynamic simulations.

The robot's body has 6-DOF; 3 translations and 3 rotations and each tire has 1-DOF in vertical direction as well as each tire has 1-DOF as a rotation about its lateral axis.

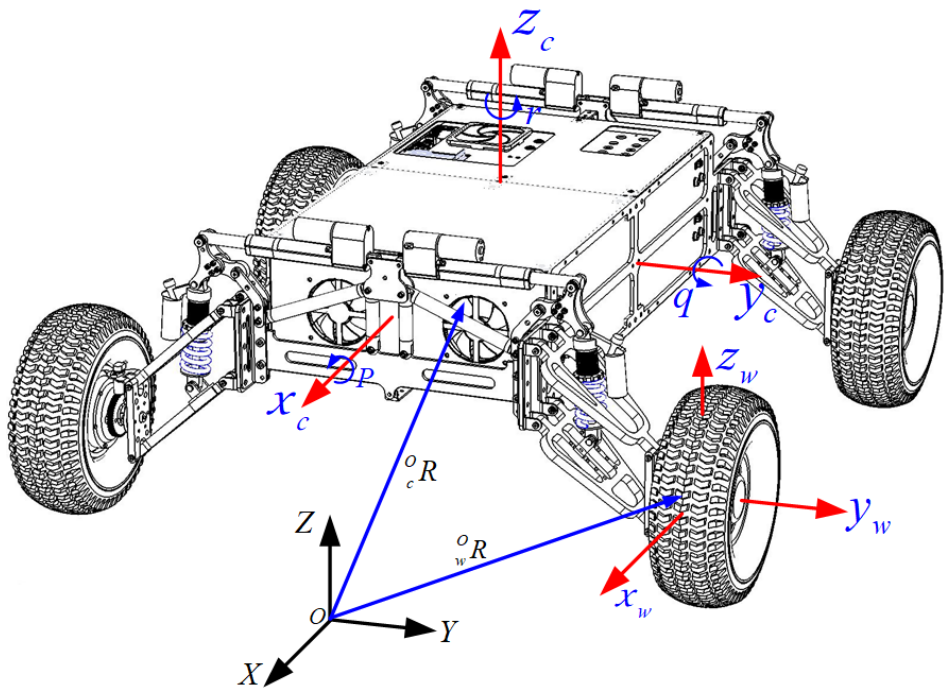

Figure 5.1: Definitions of global, local and tire coordinates

For describing the 3-D dynamic model of the robot, three coordinates are used as shown in Figure 5.1. Where the local coordinate (C) is fixed to the robot's body COM, such that the x-axis is parallel to the longitudinal direction and z-axis is directed upward as a positive direction. The tire coordinate (w_i) for each wheel is fixed at the wheel center of rotation. The relationship between local and global coordinates are defined by the rotation matrix

$R(\phi, \theta, \psi)$ as follow:

$$[X, Y, Z]^T = {}^{O}_{C}R(\phi, \theta, \psi) \times [x, y, z]^T \tag{5.1}$$

Where ϕ, θ, ψ are the Euler angles and ${}^{O}_{C}R(\phi, \theta, \psi)$ denotes the transformation from local to global frame.

$$\begin{cases} {}^{O}_{C}R(\phi, \theta, \psi) = \begin{bmatrix} r_{11} & r_{12} & r_{13} \\ r_{21} & r_{22} & r_{23} \\ r_{31} & r_{32} & r_{33} \end{bmatrix} \\ r_{11} = \cos\theta \cos\psi \\ r_{12} = \sin\phi \sin\theta \cos\psi - \cos\phi \sin\psi \\ r_{13} = \cos\phi \sin\theta \cos\psi + \sin\phi \sin\psi \\ r_{21} = \cos\theta \sin\psi \\ r_{22} = \sin\phi \sin\theta \sin\psi + \cos\phi \cos\psi \\ r_{23} = \cos\phi \sin\theta \sin\psi - \sin\phi \cos\psi \\ r_{31} = -\sin\theta \\ r_{32} = \sin\phi \cos\theta \\ r_{33} = \cos\phi \cos\theta \end{cases} \tag{5.2}$$

5.1.1 Robot's Body Dynamics

The equations of motion for the three translational and three rotational DOF, acting on the robot's body as shown in Figure 5.2 are described in the following equations:

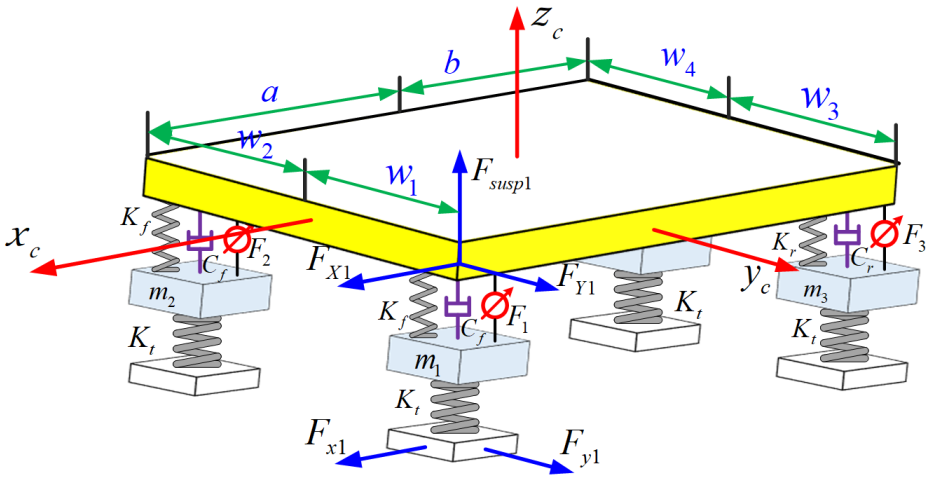

Figure 5.2: Robot free body diagram in 3D

$$
\begin{aligned}
m_t\ \dot{U} &= \sum F_x - m_t(Wq - Vr) \\
m_t\ \dot{V} &= \sum F_y - m_t(Ur - Wp) \\
m_t\ \dot{W} &= \sum F_z - m_t(Vp - Uq) \\
I_{xx}\ \dot{p} - I_{zx}\ \dot{r} &= \sum M_x + (I_{yy} - I_{zz})\ qr + I_{zx}pq \\
I_{yy}\ \dot{q} &= \sum M_y + (I_{zz} - I_{xx})pr + I_{xz}(p^2 - r^2) \\
I_{zz}\ \dot{r} - I_{xz}\ \dot{p} &= \sum M_z + (I_{xx} - I_{yy})pq + I_{xz}rq
\end{aligned}
\tag{5.3}
$$

Where, m_t the robot total mass, net forces $\sum F_x, \sum F_y, \sum F_z$ and net moments $\sum M_x, \sum M_y, \sum M_z$ acting on the robot's body COM in x, y, z respectively. U, V, W are longitudinal, lateral and vertical velocities and p, q, r are roll, pitch and yaw velocities.

The total forces in (5.3), can be described as follow:

$$
\begin{cases}
\sum F_x = \sum_{i=1}^{4} F_{x_i} + F_{G_1} \\
\sum F_y = \sum_{i=1}^{4} F_{y_i} + F_{G_2} \\
\sum F_z = \sum_{i=1}^{4} F_{susp_i} + F_{G_3}
\end{cases}
\tag{5.4}
$$

Similarly the total moments $\sum M_x, \sum M_y$ and $\sum M_z$ acting on the robot's body (5.3), can be represented as follow:

$$\begin{cases} \sum M_x = \sum_{i=1}^{4} M_{x_i} \\ \sum M_y = \sum_{i=1}^{4} M_{y_i} \\ \sum M_z = \sum_{i=1}^{4} M_{z_i} \end{cases} \tag{5.5}$$

Where $F_{x_i}, F_{y_i}, F_{susp_i}$ and $M_{x_i}, M_{y_i}, M_{z_i}$ are the forces and moments that acting on the four corners of the robot's body in x, y, z local frame. This forces are generated from the tire forces. F_{G_i} represents the gravitational forces acting on x, y, z of the robot's body.

By solving (5.3), the following transformation provides the corresponding rates in the global frame.

$$\begin{bmatrix} \dot{\phi} \\ \dot{\theta} \\ \dot{\psi} \end{bmatrix} = \begin{bmatrix} 1 & \sin\phi.\tan\theta & \cos\phi.\tan\theta \\ 0 & \cos\phi & -\sin\phi \\ 0 & \frac{\sin\phi}{\cos\theta} & \frac{\cos\phi}{\cos\theta} \end{bmatrix} \begin{bmatrix} p \\ q \\ r \end{bmatrix} \tag{5.6}$$

5.1.2 Suspension Dynamics

The four suspension systems, which include wheels, tires and EAM, are modeled as mass-spring-damper systems as shown in Figure 5.2. The wheels and part of the suspension mass are modeled as 2-DOF mass-spring-damper systems. The tires are considered as linear spring which connect the suspension masses to the road. At their top ends, the suspension masses are connected to the robot's body using the EAM.

The spring-damper forces are represented as follow:

$$\begin{cases} F_{s_1} = -K_f\big(z_c + w_1\phi - a\theta - z_{w_1}\big) \\ F_{s_2} = -K_f\big(z_c - w_2\phi - a\theta - z_{w_2}\big) \\ F_{s_3} = -K_r\big(z_c + w_3\phi + b\theta - z_{w_3}\big) \\ F_{s_4} = -K_r\big(z_c - w_4\phi + b\theta - z_{w_4}\big) \end{cases} \tag{5.7}$$

where K_f, K_r are the front and rear spring stiffness and w_1, w_2, w_3, w_4 are wheel track at front left, front right, rear left and rear right respectively, and a, b are the distance from front and rear wheel to the robot local frame respectively.

$$\begin{cases} F_{d_1} = -C_f\big(W + w_1 p - aq - \dot{z}_{w_1}\big) \\ F_{d_2} = -C_f\big(W - w_2 p - aq - \dot{z}_{w_2}\big) \\ F_{d_3} = -C_r\big(W + w_3 p + bq - \dot{z}_{w_3}\big) \\ F_{d_4} = -C_r\big(W - w_4 p + bq - \dot{z}_{w_4}\big) \end{cases} \tag{5.8}$$

The total suspension force at each corner can be written as,

$$F_{susp_i} = F_{s_i} + F_{d_i} + F_i \qquad i = 1:4 \tag{5.9}$$

where C_f, C_r are the front and the rear shock absorber damping coefficients, and F_i is the linear actuator forces at each corner.

The equation for the vertical motion of the suspension system for the i_{th} wheel can be

expressed as,

$$m_i.\ddot{z}_{w_i} = F_{susp_i} - K_t(z_{w_i} - z_{r_i}) - m_i.g \qquad (5.10)$$
$$i = 1:4$$

where m_i is the suspension mass at each corner.

5.1.3 Tire Forces and Moments

In this section, tire forces are calculated based on Pacejke tire model [50], where the vertical force and slip ratio are used to calculate tire forces at each contact patch. All tire forces are transformed from tire coordinate (w_i) to the local coordinate (C).

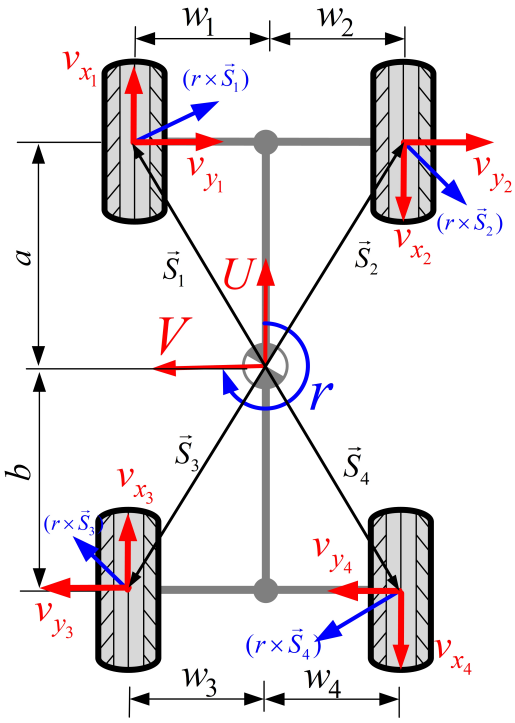

Figure 5.3: Tire longitudinal and lateral velocity components

In order to calculate the longitudinal and lateral slip ratios for each tire, we should calculate the longitudinal and lateral velocities as shown in Figure 5.3.

The longitudinal velocities at the tire center with respect to the robot's body can be calculated as,

$$\begin{cases} v_{x_1} = U + w_1 r \\ v_{x_2} = U - w_2 r \\ v_{x_3} = U + w_3 r \\ v_{x_4} = U - w_4 r \end{cases} \tag{5.11}$$

Similarly, the lateral velocities can be calculated as:

$$\begin{cases} v_{y_1} = V + ar \\ v_{y_2} = V + ar \\ v_{y_3} = V - br \\ v_{y_4} = V - br \end{cases} \tag{5.12}$$

The longitudinal slip ratio can be calculated based on the longitudinal tire velocity and rotational speed (ω) of the tire, the longitudinal slip ratio of the i_{th} wheel can be estimated as follows,

$$\begin{aligned} S_{x_i} &= \frac{\omega_i . r_i - v_{x_i}}{v_{x_i}} \qquad \text{During braking} \\ S_{x_i} &= \frac{\omega_i . r_i - v_{x_i}}{\omega_i . r_i} \qquad \text{During acceleration} \end{aligned} \tag{5.13}$$

The lateral slip can be calculated as the ratio of lateral velocity to the longitudinal wheel velocity, the lateral slip of the i_{th} wheel takes the form:

$$S_{y_i} = \frac{-v_{y_i}}{v_{x_i}} \tag{5.14}$$

After calculating the slip ratios and vertical force for each tire, we can estimate the longitudinal and later forces based on Pacejke tire model [50].

We are now able to calculate the roll, pitch, and yaw moments on the robot's body as follows,

Roll Moments:

$$\begin{cases} M_{x_1} = F_{y_1}(h_g - z + z_{w_1}) + F_{susp_1} w_1 \\ M_{x_2} = F_{y_2}(h_g - z + z_{w_2}) - F_{susp_2} w_2 \\ M_{x_3} = F_{y_3}(h_g - z + z_{w_3}) + F_{susp_3} w_3 \\ M_{x_4} = F_{y_4}(h_g - z + z_{w_4}) - F_{susp_4} w_4 \end{cases} \tag{5.15}$$

where h_g is the robot COM height with respect to global frame, and $F_{y_1}, F_{y_2}, F_{y_3}, F_{y_4}$ are the lateral tire forces at front left, front right, rear left and rear right respectively.

Pitch Moments:

$$\begin{cases} M_{y_1} = F_{x_1}(h_g - z + z_{w_1}) + F_{susp_1} a \\ M_{y_2} = F_{x_2}(h_g - z + z_{w_2}) + F_{susp_2} a \\ M_{y_3} = F_{x_3}(h_g - z + z_{w_3}) - F_{susp_3} b \\ M_{y_4} = F_{x_4}(h_g - z + z_{w_4}) - F_{susp_4} b \end{cases} \tag{5.16}$$

where $F_{x_1}, F_{x_2}, F_{x_3}, F_{x_4}$ are the longitudinal tire forces at front left, front right, rear left and rear right respectively.

Yaw Moments:

$$\begin{cases} M_{z_1} = -F_{x_1} w_1 + F_{y_1} a \\ M_{z_2} = F_{x_2} w_2 + F_{y_2} a \\ M_{z_3} = -F_{x_3} w_3 - F_{y_3} b \\ M_{z_4} = F_{x_4} w_4 - F_{y_4} b \end{cases} \tag{5.17}$$

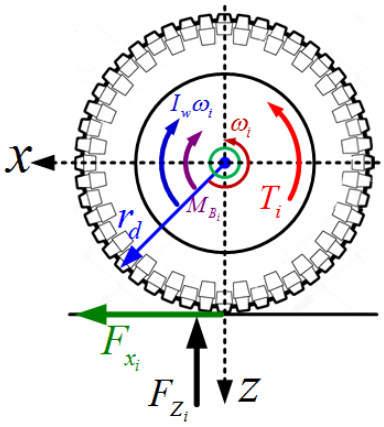

Figure 5.4: Forces and moments acting on the tire

5.1.4 Longitudinal Dynamics

The longitudinal dynamics are all forces that acting on longitudinal direction of the robot, which include rolling resistance and traction forces.

The rolling resistance force is the force generated at the tire contact patch, which opposes the wheel motion and is a major retardation force at high robot speed. The magnitude of the rolling resistance force depends mainly on the load and the surface characteristics, which is defined as follows,

$$F_{R_i} = \zeta \times F_{Z_i} \qquad i = 1:4 \tag{5.18}$$

where ζ is the coefficient of rolling resistance.

The forces and moments acting on the tire are illustrated in Figure 5.4, by balancing the wheel inertia (I_w), driving torque (T), tire longitudinal force (F_x), and rolling resistance force (F_R), the differential equation takes the following form,

$$
\begin{aligned}
I_w\ \dot{\omega}_1 &= T_1 - (F_{x_1} - F_{R_1})\ r_d \\
I_w\ \dot{\omega}_2 &= T_2 - (F_{x_2} - F_{R_2})\ r_d \\
I_w\ \dot{\omega}_3 &= T_3 - (F_{x_3} - F_{R_3})\ r_d \\
I_w\ \dot{\omega}_4 &= T_4 - (F_{x_4} - F_{R_4})\ r_d
\end{aligned}
\tag{5.19}
$$

Where r_d is the tire dynamic radius

5.2 Simulation Results

This section starts with validating the dynamic model, then evaluating the performance of controlling the active suspension system to improve the robot stability in bumpy road with high speed.

5.2.1 Model Validation

In order to design a controller for the EAM, it is essential to have a valid model to analyze the performance of the robot dynamics through computer simulations.

Remark 5.2. Due to the limitation of measuring the robot's real parameters; tire stiffness (K_t), suspension stiffness and damping (K_f, C_f), and the robot's mass moment of inertia (I_{xx}, I_{yy}, I_{zz}). The robot model should be validated with a published model.

The robot parameters that were considered for the simulation are shown in Table 5.1. These parameters are adopted from [2].

The 14-DOF robot model has been validated with published results in [2]. Two different tests are performed for validating the robot handling performance and suspension behavior.

Table 5.1: Robot Parameters.

Sprung mass (m_s)	1210 Kg
Front unsprung mass ($m_{1,2}$)	50 Kg
Rear unsprung mass ($m_{3,4}$)	50 Kg
Front spring stiffness (K_f)	20000 N/m
Rear spring stiffness (K_r)	20000 N/m
Tire spring stiffness (K_t)	220000 N/m
Front damping coefficient (C_f)	3000 Ns/m
Rear damping coefficient (C_r)	3000 Ns/m
CG location from front axle (a)	1.32 (m)
CG location from rear axle (b)	1.32 (m)
Wheel track ($w_1 + w_2$)	1.586 (m)
Pitch mass moment of inertia (I_{yy})	26070 ($Kg.m^2$)
Roll mass moment of inertia (I_{xx})	711 ($Kg.m^2$)
Yaw mass moment of inertia (I_{zz})	26744 ($Kg.m^2$)
Tire dynamic radius(r_d)	0.3509 (m)

In handling validation, the robot moves with constant forward speed $U = 30\ Km/h$, and yaw rate $r = 0.18sin(3t)\ rad$. It can be seen from Figures5.5 that the robot yaw rate and lateral acceleration are matching the published results in [2].

On the other hand for suspension validation, a step input bumpy road with amplitude 10 cm is applied to only the front left tire and measuring the vertical displacement at each corner of the robot's body and Euler angles. Figure 5.6 shows that there is a matching in the performance of the robot and the published results regarding the corner vertical displacement and the robot's roll, pitch, and yaw angles.

5.2.2 Robot Performance Evaluation

Based on the proposed controller that had been explained in section 4.3, we evaluate the performance of the robot's dynamic model with active suspension system to demonstrate the improvement of robot mobility and stability compared with passive system. In this simulation, the robot moves with high speed moving over two successive sinusoidal road

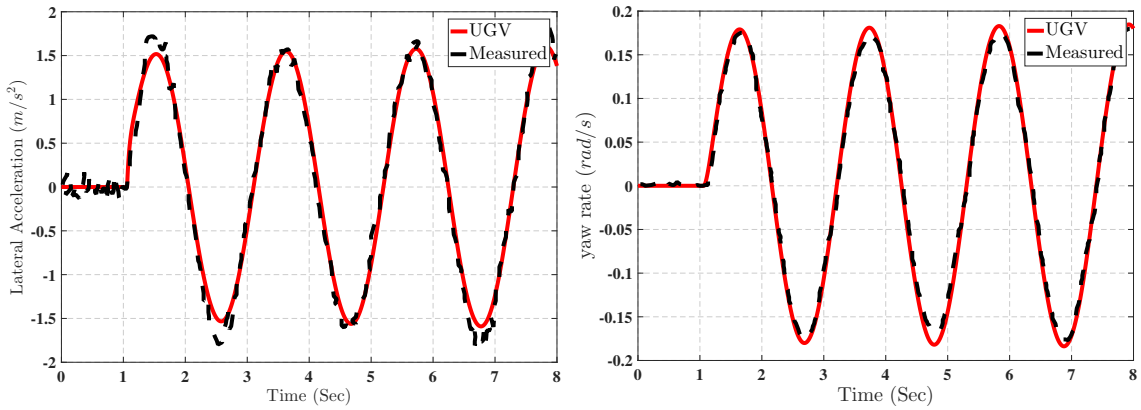

Figure 5.5: Comparison of the response of the robot and the published results in [2] with speed $U = 30$ km/h.

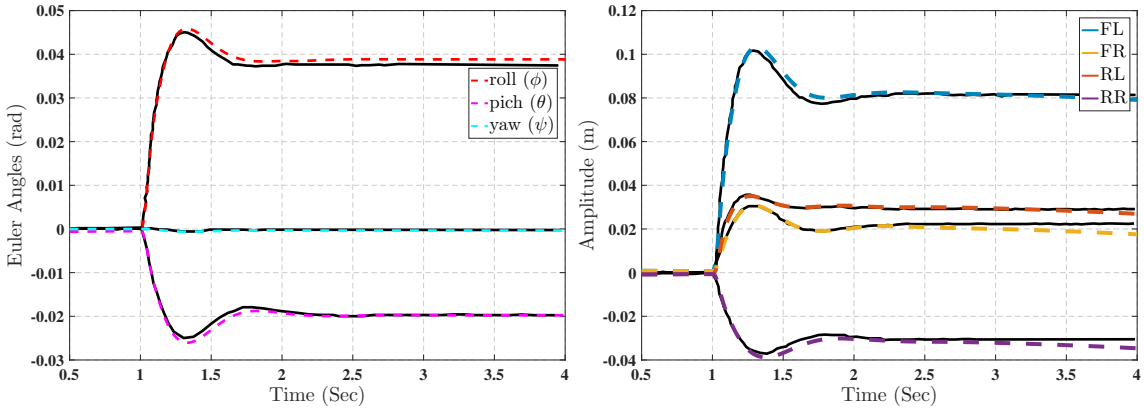

Figure 5.6: Comparison of the response of the robot and the published results in [2]. A bumpy road under only the left front wheel.

with 20 *cm* amplitude in the left side of the robot and compare between the performance of passive and active suspension systems.

It can be seen from Figure 5.7 that the active suspension system succeed to improve the robot mobility by enhancing the lateral stability, traction torque, forward speed. Where, the robot with active suspension is less deviated from the predefined path, but the robot with passive suspension is deviated from the predefined path in $Y - axis$ direction.

For robot stability, Figures 5.7 and 5.7 show the robot's rollover index, the robot's roll angle, pitch angle, yaw rate and robot's body displacement have been reduced using active

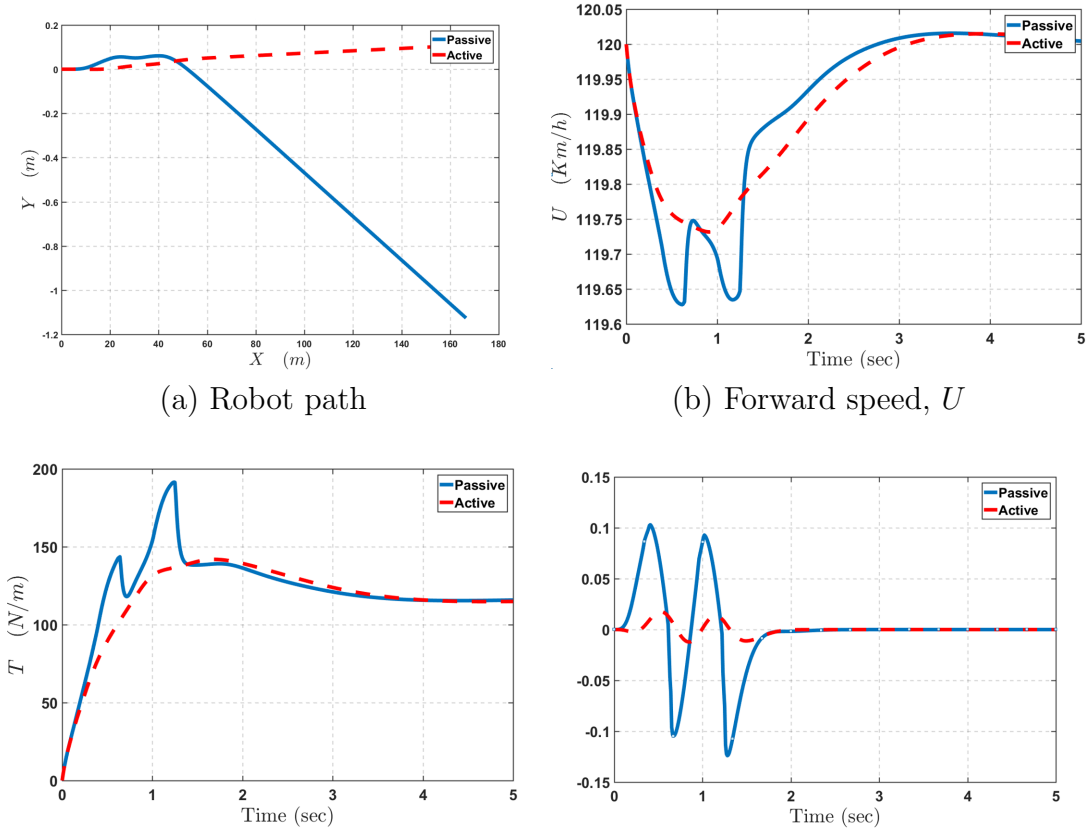

(a) Robot path

(b) Forward speed, U

(C) Total traction torque

(d) Rollover index

Figure 5.7: Comparison between robot with active and passive suspension systems.

suspension system over passive system.

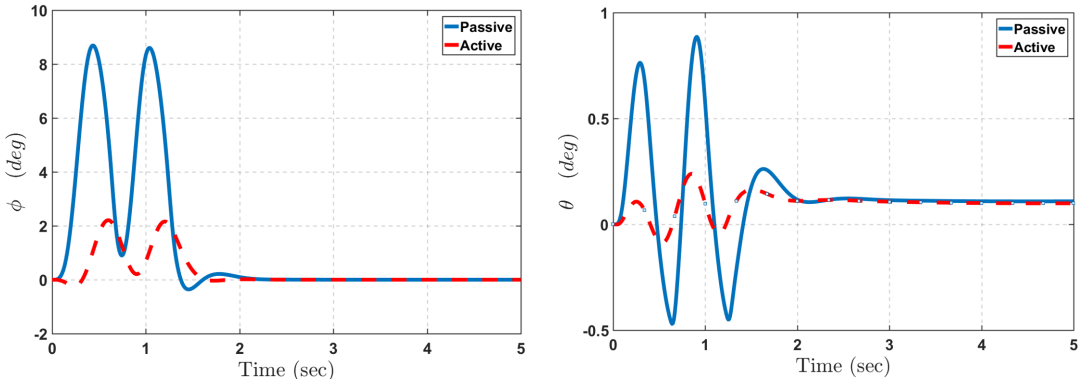

(a) Robot roll angle, ϕ

(b) Robot pitch angle, θ

(C) Robot yaw rate, r

(d) Robot's body displacement, Z_c

Figure 5.8: Comparison between robot with active and passive suspension systems.

Chapter 6

Estimation and Optimal Control of Robot Dynamics

In this chapter, we introduce a novel technique to estimate the robot dynamic model and control the active suspension system using only a noisy IMU with COM position uncertainty. The simulation results show that the observer estimates the actual behavior of the robot with 95% accuracy and up to 20% COM uncertainty. The robot's body accelerations have been reduced by 21% for bounce, 51% for pitch and 50% for roll acceleration.

6.1 Background

In recent years, particular attention has been paid to improve vehicle stability and ride comfort by using active suspension systems [40, 41, 42, 47, 51, 52, 53]. Such systems improve ride comfort by isolating the sprung mass from external disturbances that can be caused by terrain and other irregularities. They achieve vehicle stability, namely, handling stability [54], by ensuring a firm contact between tires and the road at all times. The challenge is

however that the suspension spring needs to be stiff to guarantee and satisfy several road holding criteria and in the same time the spring needs to be soft to mitigate disturbances induced by terrain and weather. In a classical vehicle suspension setting [55], the spring and the damping parameters cannot be efficiently controlled and adapted to different driving conditions. However by using an active suspension system with actuators that work along with the spring and damper, one can accumulate or dissipate energy from the system [41, 56, 57].

Active suspension systems with control techniques [58, 59, 60] have been introduced to improve the performance, handling characteristics and riding of the robot by controlling the suspension system. It has been shown that actuators controlled by optimization-based control techniques [49] are efficient for controlling the active suspension system while guaranteeing optimal performance. But in such optimization-based control techniques one needs to have full-state information to successfully control the actual model while such information is not always available in practice due to sensor cost, complexity, uncertainties, noise, or even measurement restrictions. Several observer-based techniques [59, 61, 62, 63] and modified Kalman filters [61, 64, 65, 66, 67, 68, 69] have been used to overcome such problems. A survey on how to control active and semi-active suspension system is given in [58]. In this survey, the authors used a quarter-car model for reviewing the controller design potential benefits and limitations through the application of optimal control theory with an LQ-based cost function. The work of [59] has introduced a robust control technique for an active suspension while also considering actuator constraints and uncomfortable frequency bands for bounce and pitch accelerations of the sprung mass. In [53], a nonlinear controller was used for controlling the active suspension of a quarter-car model with the ultimate goal to improve ride comfort while trying to keep the suspension deflection within the limits of the rattle space.

In [61], the authors used a Kalman filter to estimate the system states, the estimator was

based on somewhat idealized assumption of knowing exactly the road profile. The work of [64] proposed a dual extended Kalman filter to estimate the vehicle states and other parameters. In order to achieve that, the authors incorporated two parallel filters, one for estimating the main vehicle parameters and the other for estimating the vehicle states. This technique has been shown to improve the accuracy of the estimated parameters and can handle the model uncertainties. The works of [66, 67, 68] proposed similar approaches with an accuracy of the estimated states being between $70 - 90\%$.

Vehicle parameters estimation in real-time have been introduced in [70, 71], the authors used the generalized polynomial chaos based Extended Kalman Filter (gPC-EKF) for estimating the vehicle mass, the COM height, and the vehicle roll and pitch mass moment of inertia. The proposed technique has been evaluated with noisy sensors to demonstrate the robustness of the estimator in estimating the vehicle parameters in real-time.

Estimating vehicle parameters of a nonlinear half-car model has been introduced in [72, 73, 74, 75]. The authors formulated the problem by considering an unknown mass had been added to the vehicle model in an unknown position. This added mass represents the driver, passengers and any other objects in the car. The authors used the EKF for updating the polynomial chaos of the uncertain states and the uncertain parameters. This approach succeeded to estimate the values of the added mass and its position from the front axle.

The recent work of [76] has used a Kalman filter, a particle filter and artificial neural networks to estimate different states of the quarter-car model by incorporating an IMU. However, the effect of measurement uncertainties and the accuracy of the state estimation can negatively affect the higher order models. A continuous-time system identification technique in a half-car model has been proposed in [77] to estimate the robot suspension model. The aforementioned papers did not obtain the dynamic parameters of the actual robot model while taking into account the presence of measurement uncertainties. Our work is motivated by such limitations.

This chapter presents a method for estimating the robot dynamic model by using system identification techniques with a single point sensor and COM uncertainty. A combined observer/controller method has been developed to estimate the states and simultaneously improve the ride comfort and handling stability of a full robot active suspension system. We introduce an efficient solution to estimate and control the actual full robot with a limited number of sensors in the presence of noise and COM position uncertainties. A single IMU has been placed on the sprung mass, which leads us to successful estimation of all the states while at the same time controlling efficiently the suspension system to improve ride comfort and handling stability. To achieve this, we use two steps, first, estimating the robot dynamic model by analyzing all input-output paths of the transfer functions in the frequency domain, and second, applying a Kalman filter and an LQR on the estimated state-space model. The latter, allows us to calculate the optimal forces to improve the robot performance index, i.e., ride comfort and road holding stability.

The remainder of this chapter is structured as follows. In Section 6.2, we formulate the problem and introduce the full robot dynamic model with active suspension system. The proposed robot model takes into account uncertainties in the position of the center of gravity. Assuming now that the robot dynamics are unknown, Section 6.3 provides a method of estimating the mathematical model of the robot, which is based on system identification techniques. In Section 6.4, we design an observer based on a Kalman filter for estimating the robot states and feed the result in the optimal control algorithm in order to control the active suspension system. Section 6.5, provides a numerical simulation for estimating the robot dynamics behavior while controlling optimally the suspension system to simultaneously improve the ride comfort and road holding stability within the limits of the rattle space. Finally, Section 6.6 concludes and discusses future work.

Notation: The notation used here is standard. $\lambda(A)$ is the eigenvalues of a matrix A, $(.)^{\mathrm{T}}$ denotes the transpose of a matrix, $\bar{z}$ is the conjugate of the complex number z, $\hat{A}$ is

the estimated value of A in continuous time, $\hat{A}_d$ is the estimated value of A in discrete time. The superscript $*$ is used to denote the optimal solution of an optimization, the superscript/subscript k is used to denote a value at discrete time k, the subscript s denotes the sprung mass value while the subscript m denotes the IMU signals. $A \succeq 0$ denotes that the matrix A is positive semidefinite and the notation $A \succ 0$ to denote that the matrix A is positive definite. Finally, $H(s)$ denotes the transfer function H in s-domain and $H(z)$ denotes the transfer function in z-domain.

6.2 Problem Formulation

A linear full robot model with seven DOF as shown in Figure 6.1 is considered for this research because it is sufficient and enough for capturing the robot dynamical behavior [78, 79, 80]. The authors in [80] compared the results of a linear robot model with a measured data through an experimental test using the same road input. These results show a close match between the simulation model and the experimental test, which gives credence to use a linear robot model for estimating the states and optimally controlling the active suspension system to enhance ride comfort and robot stability.

The full robot model consists of a sprung mass with three DOF in the vertical Z_s-axis (bounce), rotation about X_s-axis (roll) and rotation about Y_s-axis (pitch), with four unsprung masses in front left, front right, rear left and rear right which have one DOF in the vertical directions z_1, z_2, z_3, z_4 at front left, front right, rear left and rear right respectively.

The dynamic equations of the full robot system can be derived using the Newton's second

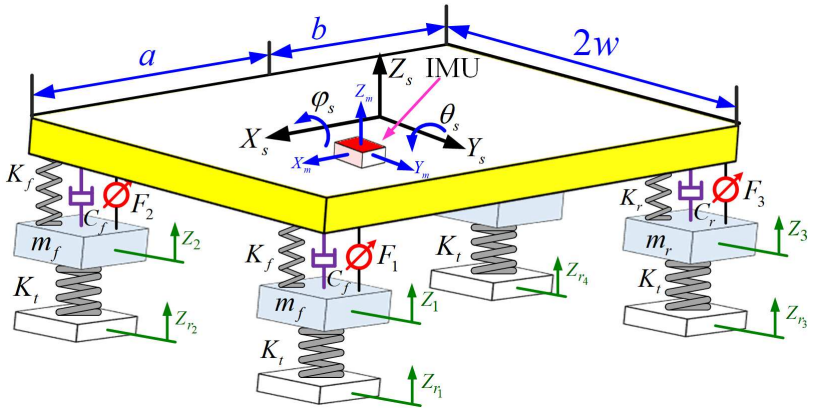

Figure 6.1: The full robot model with active suspension system.

law as follows [44, 45, 46, 47],

$$
\begin{aligned}
m_s\ddot{z}_s &= F_{fl} + F_{fr} + F_{rl} + F_{rr},\\
I_{yy}\ddot{\theta}_s &= -aF_{fl} - aF_{fr} + bF_{rl} + bF_{rr},\\
I_{xx}\ddot{\phi}_s &= wF_{fl} - wF_{fr} + wF_{rl} - wF_{rr},\\
m_f\ddot{z}_1 &= -F_{fl} - k_t(z_1 - z_{r_1}),\\
m_f\ddot{z}_2 &= -F_{fr} - k_t(z_2 - z_{r_2}),\\
m_r\ddot{z}_3 &= -F_{rl} - k_t(z_3 - z_{r_3}),\\
m_r\ddot{z}_4 &= -F_{rr} - k_t(z_4 - z_{r_4}),
\end{aligned}
\tag{6.1}
$$

where m_s is the mass of the robot body, I_{xx} is the roll moment, I_{yy} is the pitch moment of inertia about the COM, ϕ_s, θ_s are the roll and pitch angles of the sprung mass, a, b are the COM locations of the front and rear wheels, $2w$ is the wheel track, m_f, m_r stand for the unsprung mass on front and rear respectively, k_t is the tire spring stiffness, $z_{r_1}, z_{r_2}, z_{r_3}, z_{r_4}$ are the road displacements at front left, front right, rear left and rear right respectively, and $F_{fl}, F_{fr}, F_{rl}, F_{rr}$ are the forces generated between the sprung mass at each corner and the unsprung masses at front left, front right, rear left and rear right respectively.

The forces are defined as follows,

$$\begin{aligned} F_{fl} &:= -k_f(z_{fl} - z_1) - c_f(\dot{z}_{fl} - \dot{z}_1) + F_1, \\ F_{fr} &:= -k_f(z_{fr} - z_2) - c_f(\dot{z}_{fr} - \dot{z}_2) + F_2, \\ F_{rl} &:= -k_r(z_{rl} - z_3) - c_r(\dot{z}_{rl} - \dot{z}_3) + F_3, \\ F_{rr} &:= -k_r(z_{rr} - z_4) - c_r(\dot{z}_{rr} - \dot{z}_4) + F_4, \end{aligned} \tag{6.2}$$

where k_f is the front spring stiffness and k_r is the rear spring stiffness, c_f, c_r are the front and the rear shock absorber damping coefficients, and F_1, F_2, F_3, F_4 are the active suspension actuators at the front left, the front right, the rear left and the rear right respectively.

The dynamics can be simplified by applying the following assumption.

Assumption 2. The angles θ_s and ϕ_s, are small enough and we can write $\sin\theta_s \approx \theta_s$, $\sin\phi_s \approx \phi_s$.

Based on Assumption 2 the dynamic vertical displacements of the sprung mass corners can be written as,

$$\begin{aligned} z_{fl} &:= z_s + w\phi_s - a\theta_s, \\ z_{fr} &:= z_s - w\phi_s - a\theta_s, \\ z_{rl} &:= z_s + w\phi_s + b\theta_s, \\ z_{rr} &:= z_s - w\phi_s + b\theta_s. \end{aligned} \tag{6.3}$$

For simplicity let us use the following state-space assignments,

$$\begin{aligned} &x_1 := z_{fl} - z_1, && x_2 := z_{fr} - z_2, && x_3 := z_{rl} - z_3, && x_4 := z_{rr} - z_4, \\ &x_5 := z_1 - z_{r_1}, && x_6 := z_2 - z_{r_2}, && x_7 := z_3 - z_{r_3}, && x_8 := z_4 - z_{r_4}, \\ &x_9 := \dot{z}_s, && x_{10} := \dot{\theta}_s, && x_{11} := \dot{\phi}_s, \\ &x_{12} := \dot{z}_1, && x_{13} := \dot{z}_2, && x_{14} := \dot{z}_3, && x_{15} := \dot{z}_4. \end{aligned}$$

The state-space assignments rewrite (6.1)-(6.3) as follows,

$$\begin{aligned} \dot{X} &= AX + B_e Q + B_f F, \\ Y &= CX + D_e Q + D_f F, \end{aligned} \tag{6.4}$$

where,

$$\begin{aligned} X &= \begin{bmatrix} x_1 & x_2 & x_3 & ... & x_{12} & x_{13} & x_{14} \end{bmatrix}^{\mathrm{T}}, \\ Y &= \begin{bmatrix} \ddot{z}_s & \ddot{\theta}_s & \ddot{\phi}_s \end{bmatrix}^{\mathrm{T}}, \\ Q &= \begin{bmatrix} \dot{z}_{r_1} & \dot{z}_{r_2} & \dot{z}_{r_3} & \dot{z}_{r_4} \end{bmatrix}^{\mathrm{T}}, \qquad F = \begin{bmatrix} F_1 & F_2 & F_3 & F_4 \end{bmatrix}^{\mathrm{T}}. \end{aligned}$$

Matrices $A, B_e, B_f, C, D_e, D_f, Q, F$ are defined according to the sate-space representation of robot model as follows,

$$A = \begin{bmatrix} A_1 & A_2 & \cdots & A_{14} & A_{15} \end{bmatrix}.$$

Where,

$$A_1 = \begin{bmatrix} 0\ 0\ 0\ 0\ 0\ 0\ 0\ 0\ 1\ -a\ w\ -1\ 0\ 0\ 0 \end{bmatrix}, \quad A_2 = \begin{bmatrix} 0\ 0\ 0\ 0\ 0\ 0\ 0\ 0\ 1\ -a\ -w\ 0\ -1\ 0\ 0 \end{bmatrix},$$

$$A_3 = \begin{bmatrix} 0\ 0\ 0\ 0\ 0\ 0\ 0\ 0\ 1\ b\ w\ 0\ 0\ -1\ 0 \end{bmatrix}, \qquad A_4 = \begin{bmatrix} 0\ 0\ 0\ 0\ 0\ 0\ 0\ 0\ 1\ b\ -w\ 0\ 0\ 0\ -1 \end{bmatrix},$$

$$A_5 = \begin{bmatrix} 0\ 0\ 0\ 0\ 0\ 0\ 0\ 0\ 0\ 0\ 0\ 0\ 1\ 0\ 0\ 0 \end{bmatrix}, \quad A_6 = \begin{bmatrix} 0\ 0\ 0\ 0\ 0\ 0\ 0\ 0\ 0\ 0\ 0\ 0\ 0\ 1\ 0\ 0 \end{bmatrix},$$

$$A_7 = \begin{bmatrix} 0\ 0\ 0\ 0\ 0\ 0\ 0\ 0\ 0\ 0\ 0\ 0\ 0\ 0\ 1\ 0 \end{bmatrix}, \quad A_8 = \begin{bmatrix} 0\ 0\ 0\ 0\ 0\ 0\ 0\ 0\ 0\ 0\ 0\ 0\ 0\ 0\ 0\ 1 \end{bmatrix},$$

$$A_9 = \frac{1}{m_s}\begin{bmatrix} -k_f \\ -k_f \\ -k_r \\ -k_r \\ 0 \\ 0 \\ 0 \\ 0 \\ -2(c_f + c_r) \\ 2(ac_f - bc_r) \\ 0 \\ c_f \\ c_f \\ c_r \\ c_r \end{bmatrix}^{\mathrm{T}}, \; A_{10} = \frac{1}{I_y}\begin{bmatrix} ak_f \\ ak_f \\ bk_r \\ bk_r \\ 0 \\ 0 \\ 0 \\ 0 \\ 2(ac_f - bc_r) \\ -2(a^2c_f + b^2c_r) \\ 0 \\ -ac_f \\ -ac_f \\ bc_r \\ bc_r \end{bmatrix}^{\mathrm{T}}, \; A_{11} = \frac{w}{I_x}\begin{bmatrix} -k_f \\ k_f \\ -k_r \\ k_r \\ 0 \\ 0 \\ 0 \\ 0 \\ 0 \\ 0 \\ -2w(c_f + c_r) \\ c_f \\ -c_f \\ c_r \\ -c_r \end{bmatrix}^{\mathrm{T}},$$

$$A_{12} = \frac{1}{m_f}\begin{bmatrix} k_f \\ 0 \\ 0 \\ 0 \\ -k_t \\ 0 \\ 0 \\ 0 \\ c_f \\ -ac_f \\ wc_f \\ -c_f \\ 0 \\ 0 \\ 0 \end{bmatrix}^{\mathrm{T}}, \; A_{13} = \frac{1}{m_f}\begin{bmatrix} 0 \\ k_f \\ 0 \\ 0 \\ 0 \\ -k_t \\ 0 \\ 0 \\ c_f \\ -ac_f \\ -wc_f \\ 0 \\ -c_f \\ 0 \\ 0 \end{bmatrix}^{\mathrm{T}}, \quad A_{14} = \frac{1}{m_r}\begin{bmatrix} 0 \\ 0 \\ k_r \\ 0 \\ 0 \\ 0 \\ -k_t \\ 0 \\ c_r \\ bc_r \\ wc_r \\ 0 \\ 0 \\ -c_r \\ 0 \end{bmatrix}^{\mathrm{T}}, \quad A_{15} = \frac{1}{m_r}\begin{bmatrix} 0 \\ 0 \\ k_r \\ 0 \\ 0 \\ 0 \\ -k_t \\ 0 \\ 0 \\ 0 \\ c_r \\ bc_r \\ -wc_r \\ -c_r \end{bmatrix}^{\mathrm{T}},$$

$$C = \begin{bmatrix} A_9 & A_{10} & A_{11} \end{bmatrix}^{\mathrm{T}}, \qquad D_e = \begin{bmatrix} 0 & 0 & 0 & 0 \\ 0 & 0 & 0 & 0 \\ 0 & 0 & 0 & 0 \end{bmatrix}, \qquad D_f = \begin{bmatrix} \frac{1}{m_s} & \frac{1}{m_s} & \frac{1}{m_s} & \frac{1}{m_s} \\ \frac{-a}{I_y} & \frac{-a}{I_y} & \frac{b}{I_y} & \frac{b}{I_y} \\ \frac{w}{I_x} & \frac{-w}{I_x} & \frac{w}{I_x} & \frac{-w}{I_x}. \end{bmatrix}$$

$$B_e = \begin{bmatrix} 0 & 0 & 0 & 0 \\ 0 & 0 & 0 & 0 \\ 0 & 0 & 0 & 0 \\ 0 & 0 & 0 & 0 \\ -1 & 0 & 0 & 0 \\ 0 & -1 & 0 & 0 \\ 0 & 0 & -1 & 0 \\ 0 & 0 & 0 & -1 \\ 0 & 0 & 0 & 0 \\ 0 & 0 & 0 & 0 \\ 0 & 0 & 0 & 0 \\ 0 & 0 & 0 & 0 \\ 0 & 0 & 0 & 0 \\ 0 & 0 & 0 & 0 \\ 0 & 0 & 0 & 0 \end{bmatrix}, \qquad B_f = \begin{bmatrix} 0 & 0 & 0 & 0 \\ 0 & 0 & 0 & 0 \\ 0 & 0 & 0 & 0 \\ 0 & 0 & 0 & 0 \\ 0 & 0 & 0 & 0 \\ 0 & 0 & 0 & 0 \\ 0 & 0 & 0 & 0 \\ 0 & 0 & 0 & 0 \\ \frac{1}{m_s} & \frac{1}{m_s} & \frac{1}{m_s} & \frac{1}{m_s} \\ \frac{-a}{I_y} & \frac{-a}{I_y} & \frac{b}{I_y} & \frac{b}{I_y} \\ \frac{w}{I_x} & \frac{-w}{I_x} & \frac{w}{I_x} & \frac{-w}{I_x} \\ \frac{-1}{m_f} & 0 & 0 & 0 \\ 0 & \frac{-1}{m_f} & 0 & 0 \\ 0 & 0 & \frac{-1}{m_r} & 0 \\ 0 & 0 & 0 & \frac{-1}{m_r} \end{bmatrix}.$$

And,

The active suspension system is designed to improve ride comfort and road holding stability within the limits of the suspension deflection. Hence, three aspects are going to be considered in our work:

1. Ride comfort which is related to the sprung mass bounce, roll, and pitch accelerations. By reducing these accelerations, good ride comfort will be experienced by the passengers.

2. Road holding stability which is defined by the tire dynamic load; where to ensure robot stability, the dynamic tire load should not exceed its static load to maintain

uninterrupted contact with the road, which can be expressed as the relative tire loads and is given by,

$$\eta_1 := \frac{k_t(z_1 - z_{r_1})}{g\left(\frac{bm_s}{2(a+b)} + m_f\right)} < 1,$$
$$\eta_2 := \frac{k_t(z_2 - z_{r_2})}{g\left(\frac{bm_s}{2(a+b)} + m_f\right)} < 1,$$
$$\eta_3 := \frac{k_t(z_3 - z_{r_3})}{g\left(\frac{am_s}{2(a+b)} + m_r\right)} < 1,$$
$$\eta_4 := \frac{k_t(z_4 - z_{r_4})}{g\left(\frac{am_s}{2(a+b)} + m_r\right)} < 1,$$

where $\eta_1, \eta_2, \eta_3, \eta_4$ are the relative tire loads at front left, front right, rear left and rear right, and g is the gravitational acceleration.

3. And finally, the suspension deflection which is limited by the available rattle space as follow,

$$\mu_1 := \frac{|z_{fl} - z_1|}{z_{max}} < 1, \qquad \mu_2 := \frac{|z_{fr} - z_2|}{z_{max}} < 1,$$
$$\mu_3 := \frac{|z_{rl} - z_3|}{z_{max}} < 1, \qquad \mu_4 := \frac{|z_{rr} - z_4|}{z_{max}} < 1,$$

where $\mu_1, \mu_2, \mu_3, \mu_4$ are the relative suspension deflections at front left, front right, rear left and rear right, and z_{max} is the maximum rattle space hard limit.

Figure 6.2, in addition to Figure 6.1, shows the location of the IMU. The measured signals for bounce acceleration, roll and pitch velocities are governed by the measurement model of IMU, where the position uncertainties are denoted by r_m. We differentiate the IMU angular velocities to get the angular accelerations.

Referring to (6.5)-(6.7), the IMU position, the velocity and the acceleration vectors $r, \dot{r}$, and

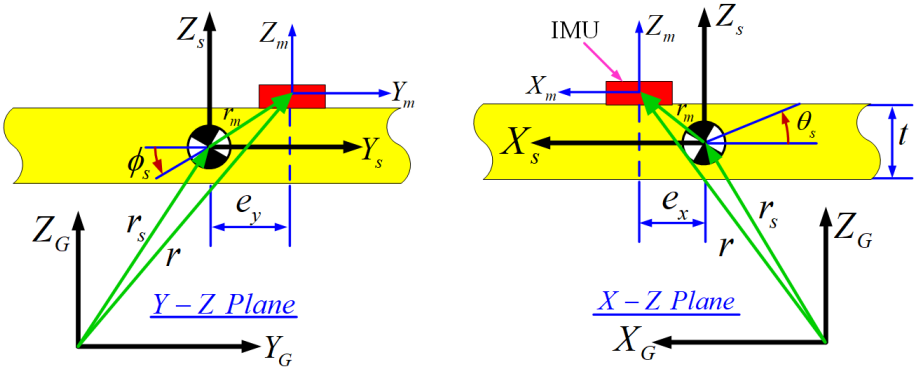

Figure 6.2: An IMU is placed on the robot's body with distance $(e_x, e_y, t/2)$ from the real COM position.

$\ddot{r}$ respectively, can be calculated with respect to the world-fixed frame (X_G, Y_G, Z_G) as,

$$r = r_{\mathrm{s}} + A_{\mathrm{r}}(\phi, \theta)\ r_{\mathrm{m}}, \tag{6.5}$$

$$\begin{aligned} \dot{r} = \dot{r}_s + \Bigg(\dot{\phi}_s \begin{bmatrix} 0 & 0 & 0 \\ \cos\phi_s \sin\theta_s & -\sin\phi_s & -\cos\phi_s \cos\theta_s \\ \sin\phi_s \sin\theta_s & \cos\phi_s & -\sin\phi_s \cos\theta_s \end{bmatrix} \\ + \dot{\theta}_s \begin{bmatrix} -\sin\theta_s & 0 & \cos\theta_s \\ \sin\phi_s \cos\theta_s & 0 & \sin\phi_s \sin\theta_s \\ -\cos\phi_s \cos\theta_s & 0 & -\cos\phi_s \sin\theta_s \end{bmatrix} \Bigg) r_m, \end{aligned} \tag{6.6}$$

and,

$$\begin{aligned} \ddot{r} = \ddot{r}_s + \Bigg(\ddot{\phi}_s \begin{bmatrix} 0 & 0 & 0 \\ \cos\phi_s \sin\theta_s & -\sin\phi_s & -\cos\phi_s \cos\theta_s \\ \sin\phi_s \sin\theta_s & \cos\phi_s & -\sin\phi_s \cos\theta_s \end{bmatrix} - \dot{\phi}_s^2 \begin{bmatrix} 0 & 0 & 0 \\ \sin\phi_s \sin\theta_s & \cos\phi_s & -\sin\phi_s \cos\theta_s \\ -\cos\phi_s \sin\theta_s & \sin\phi_s & \cos\phi_s \cos\theta_s \end{bmatrix} \\ + \ddot{\theta}_s \begin{bmatrix} -\sin\theta_s & 0 & \cos\theta_s \\ \sin\phi_s \cos\theta_s & 0 & \sin\phi_s \sin\theta_s \\ -\cos\phi_s \cos\theta_s & 0 & -\cos\phi_s \sin\theta_s \end{bmatrix} - \dot{\theta}_s^2 \begin{bmatrix} \cos\theta_s & 0 & \sin\theta_s \\ \sin\phi_s \sin\theta_s & 0 & -\sin\phi_s \cos\theta_s \\ -\cos\phi_s \sin\theta_s & 0 & \cos\phi_s \cos\theta_s \end{bmatrix} \end{aligned}$$

$$+ 2\dot{\phi}_s\dot{\theta}_s \begin{bmatrix} 0 & 0 & 0 \\ \cos\phi_s\cos\theta_s & 0 & \cos\phi_s\sin\theta_s \\ \sin\phi_s\cos\theta_s & 0 & \sin\phi_s\sin\theta_s \end{bmatrix} \Big) r_m, \tag{6.7}$$

where the rotation matrix is,

$$A_{\mathrm{r}}(\phi,\theta) = \begin{bmatrix} \cos\theta_s & 0 & \sin\theta_s \\ \sin\phi_s\sin\theta_s & \cos\phi_s & -\sin\theta_s\cos\theta_s \\ -\cos\phi_s\sin\theta_s & \sin\phi_s & \cos\theta_s\cos\theta_s \end{bmatrix},$$

and the position vectors are defined as,

$$r := \begin{bmatrix} X_{\mathrm{m}} & Y_{\mathrm{m}} & Z_{\mathrm{m}} \end{bmatrix}^{\mathrm{T}}, \qquad r_s := \begin{bmatrix} X_{\mathrm{s}} & Y_{\mathrm{s}} & Z_{\mathrm{s}} \end{bmatrix}^{\mathrm{T}}, \qquad r_m := \begin{bmatrix} e_{\mathrm{x}} & e_{\mathrm{y}} & 0.5t \end{bmatrix}^{\mathrm{T}}.$$

In order to model a potentially noisy IMU, a white Gaussian noise with zero mean and variance σ_ν is added to the IMU signals as,

$$y_{\mathrm{m}} = s_{\mathrm{m}} + \nu, \tag{6.8}$$

where,

$$s_{\mathrm{m}} := \begin{bmatrix} \ddot{z}_{\mathrm{m}} & \ddot{\theta}_{\mathrm{s}} & \ddot{\phi}_{\mathrm{s}} \end{bmatrix}^{\mathrm{T}}, \qquad \nu \sim \mathcal{N}(0,\, \sigma_\nu^2).$$

By writing (6.8) in the frequency domain one has,

$$Y_{\mathrm{m}}(s) = H(s)U(s) + \nu, \qquad U(s) = \begin{bmatrix} Q & F \end{bmatrix}^{\mathrm{T}}, \tag{6.9}$$

where $H(s)$ is the transfer function and $U(s)$ is the input signal.

Since the IMU signals are in discrete-time domain, the bilinear transformation is employed to

transform the system from continuous-time to discrete-time [81]. In other words, all transfer functions in (6.9) can be written as,

$$H(z) = H(s)\left(\frac{2}{T_s}\left(\frac{z-1}{z+1}\right)\right), \tag{6.10}$$

where $H(z)$ is the transfer function in the discrete-time domain, and $T_s \in \mathbb{R}^+$ is the sampling time.

6.3 Robot Dynamic Model Estimation

In this section, the robot state-space model is estimated by analyzing the input-output paths to estimate the FRF for each path in frequency domain.

The system identification technique proposed in this section is based on exciting the full robot model at the wheels, and the active suspension actuators. A diagram of the proposed technique is shown in Figure 6.3.

The excitation signals are filtered white noises with zero mean and variance σ_u [82] as follows,

$$u(t) = L(q)e(t),$$

where, q is the backward shift operator, i.e., $q = z^{-1}$, and $L(q)$ is a first order low pass filter, i.e., $L(z^{-1}) = \frac{z^{-1}+1}{\frac{\pi-2}{\pi}z^{-1}-\frac{2}{\pi}}$, with breaking frequency $\omega_b = \frac{\pi}{T_s}$ used to eliminate the false response at the Nyquist frequency.

The channel-by-channel excitation signals are shown in Figure 6.4, where, filtered signals of amplitude $|Z_r| \leq 0.1$m and frequency $0.05 : 100$Hz, and of amplitude $|F_i| \leq 100$N and frequency $0.05 : 100$Hz are generated at the wheels, and the actuators respectively.

During this process, the excitations and the IMU signals are recorded for further analysis.

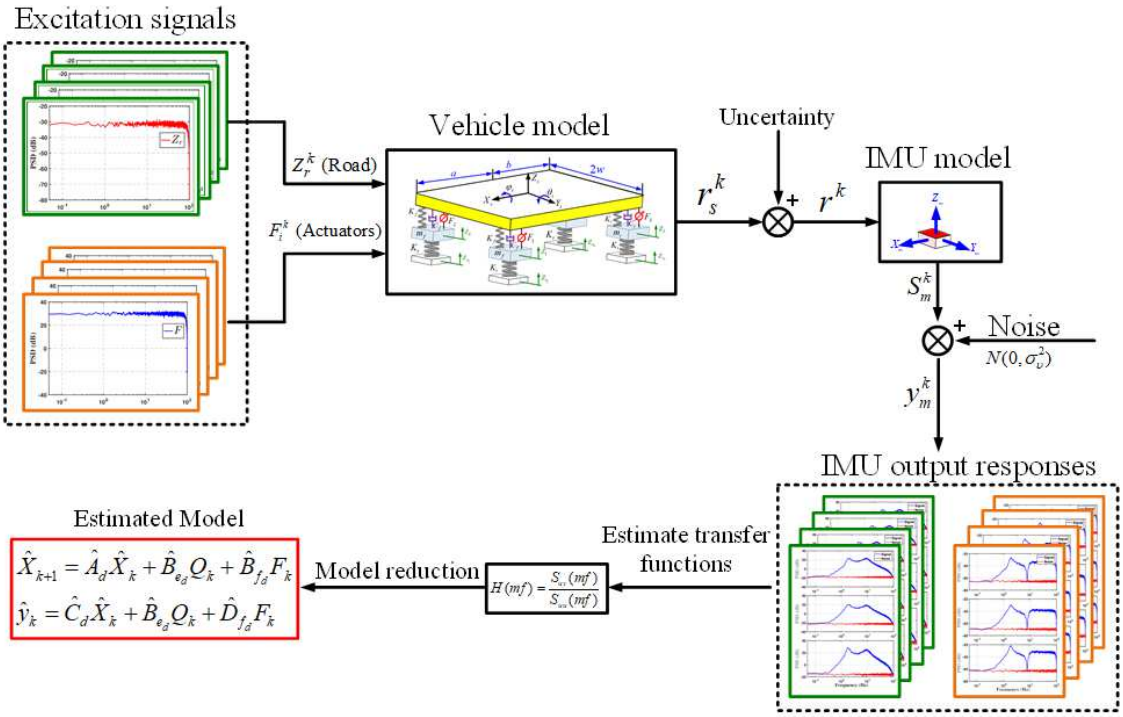

Figure 6.3: Dynamic model estimation diagram. It is shown the steps of estimating the robot dynamic model using only IMU.

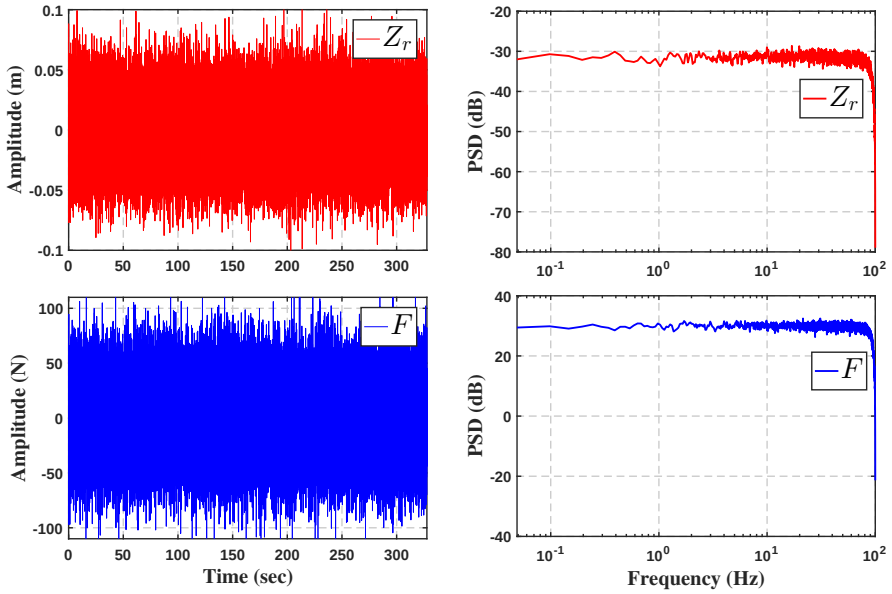

Figure 6.4: The excitation signals in time and frequency domains.

Here, the transfer functions are estimated by analyzing the IMU signals in the frequency domain to determine the locations and numbers of poles and zeros. In order to estimate the noise power of the IMU, all the excitation signals are set to zero, i.e., $Z_r = 0$ and $F_i = 0$, and the IMU signals are recorded at the steady-state in order to calculate the bias and the standard deviation σ_ν as a calibration process for the IMU.

The noise power can now be estimated by using,

$$\sigma_\nu^2 = E\Big[y_m^2 | s_m = 0\Big].$$

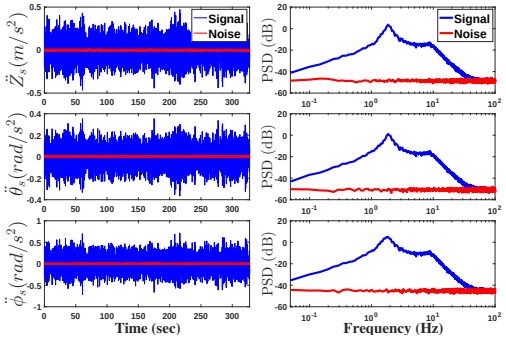

(a) Front left wheel.

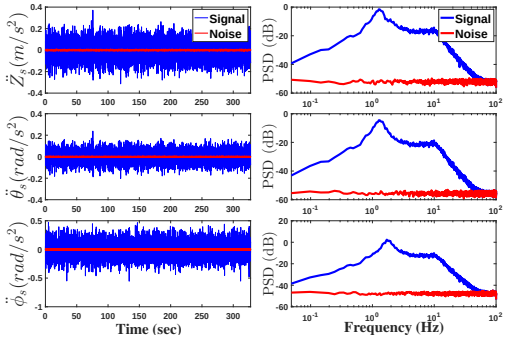

(b) Rear right wheel.

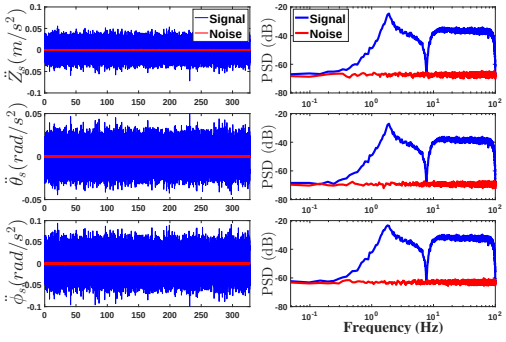

(c) Front left actuator.

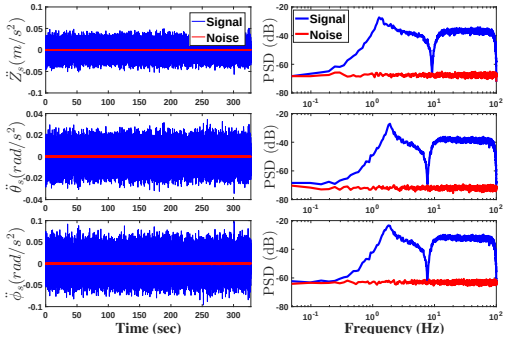

(d) Rear right actuator.

Figure 6.5: IMU output responses during the excitation process.

The IMU response signal and the noise in the time and the frequency domains are shown in Figure 6.5 during the excitation process, where, the discrete Fourier transform [83] is used to transform the signals from the time to the frequency domain and to calculate the power

spectral density of the IMU signals.

Assuming that the noise ν is uncorrelated with the output signal s_m, then the power of the output signals can be calculated from (6.8) as follows,

$$\sigma_y^2 = E\Big[y_m^2\Big] = E\Big[(S_m + \nu)^2\Big] = E\Big[S_m^2 + 2S_m\nu + \nu^2\Big],$$

$$\sigma_y^2 = E\Big[s_m^2\Big] + E\Big[\nu^2\Big] = \sigma_s^2 + \sigma_\nu^2,$$
$$\sigma_s^2 = \sigma_y^2 - \sigma_\nu^2.$$

In order to identify the unknown system dynamics given by (6.4), we have to estimate 24 input-output paths o frequency response functions (FRFs) in (6.11),

$$\begin{bmatrix} Z_{\mathrm{m}}^a \\ \\ \theta_{\mathrm{s}}^a \\ \\ \phi_{\mathrm{s}}^a \end{bmatrix} = \begin{bmatrix} H_{11} & H_{12} & \ldots & H_{17} & H_{18} \\ \\ H_{21} & H_{22} & \ldots & H_{27} & H_{28} \\ \\ H_{31} & H_{32} & \ldots & H_{37} & H_{38} \end{bmatrix} \begin{bmatrix} Z_{\mathrm{r}_1} \\ \vdots \\ Z_{\mathrm{r}_4} \\ F_1 \\ \vdots \\ F_4 \end{bmatrix}, \tag{6.11}$$

where $Z_{\mathrm{m}}^a, \theta_{\mathrm{s}}^a, \phi_{\mathrm{s}}^a$ represent the acceleration values of the IMU in frequency domain.

After applying the discrete Fourier transform, we can rewrite (6.9) as,

$$Y_{\mathrm{m}}(mf) = H(mf)U(mf) + \nu(mf), \tag{6.12}$$

where f is the frequency resolution given as $f = \frac{1}{NT_s}$, and N, is the number of data samples used.

The next step is to multiply (6.12) with the input conjugate $\bar{U}$ while assuming that the input is uncorrelated with the noise signal to write,

$$\begin{aligned}\bar{U}(mf)Y_{\mathrm{m}}(mf) &= H(mf)\bar{U}(mf)U(mf) + \bar{U}(mf)\nu(mf),\\ S_{\mathrm{uy}}(mf) &= H(mf)S_{\mathrm{uu}}(mf) + S_{\mathrm{u}\nu}(mf).\end{aligned} \tag{6.13}$$

Using (6.13), the FRF can be estimated as follows,

$$H(mf) = \frac{S_{\mathrm{uy}}(mf)}{S_{\mathrm{uu}}(mf)}, \tag{6.14}$$

where $S_{\mathrm{uu}}(mf)$, $S_{\mathrm{uy}}(mf)$ are the auto-spectrum and cross-spectrum of the input-input and input-output signals respectively.

From (6.11) and (6.14), the FRFs can be estimated as,

$$\begin{aligned}
H_{11}(mf) &= \frac{S_{Z_{r_1}\ddot{Z}_m}(mf)}{S_{Z_{r_1}Z_{r_1}}(mf)}, & H_{12}(mf) &= \frac{S_{Z_{r_2}\ddot{Z}_m}(mf)}{S_{Z_{r_2}Z_{r_2}}(mf)}, & H_{13}(mf) &= \frac{S_{Z_{r_3}\ddot{Z}_m}(mf)}{S_{Z_{r_3}Z_{r_3}}(mf)},\\
H_{14}(mf) &= \frac{S_{Z_{r_4}\ddot{Z}_m}(mf)}{S_{Z_{r_4}Z_{r_4}}(mf)}, & H_{15}(mf) &= \frac{S_{F_1\ddot{Z}_m}}{S_{F_1F_1}(mf)}, & H_{16}(mf) &= \frac{S_{F_2\ddot{Z}_m}}{S_{F_2F_2}(mf)},\\
H_{17}(mf) &= \frac{S_{F_3\ddot{Z}_m}}{S_{F_3F_3}(mf)}, & H_{18}(mf) &= \frac{S_{F_4\ddot{Z}_m}}{S_{F_4F_4}(mf)}, & H_{21}(mf) &= \frac{S_{Z_{r_1}\ddot{\theta}_s}(mf)}{S_{Z_{r_1}Z_{r_1}}(mf)},\\
H_{22}(mf) &= \frac{S_{Z_{r_2}\ddot{\theta}_s}(mf)}{S_{Z_{r_2}Z_{r_2}}(mf)}, & H_{23}(mf) &= \frac{S_{Z_{r_3}\ddot{\theta}_s}(mf)}{S_{Z_{r_3}Z_{r_3}}(mf)}, & H_{24}(mf) &= \frac{S_{Z_{r_4}\ddot{\theta}_s}(mf)}{S_{Z_{r_4}Z_{r_4}}(mf)},\\
H_{25}(mf) &= \frac{S_{F_1\ddot{\theta}_s}(mf)}{S_{F_1F_1}(mf)}, & H_{26}(mf) &= \frac{S_{F_2\ddot{\theta}_s}(mf)}{S_{F_2F_2}(mf)}, & H_{27}(mf) &= \frac{S_{F_3\ddot{\theta}_s}(mf)}{S_{F_3F_3}(mf)},\\
H_{28}(mf) &= \frac{S_{F_4\ddot{\theta}_s}(mf)}{S_{F_4F_4}(mf)}, & H_{31}(mf) &= \frac{S_{Z_{r_1}\ddot{\phi}_s}(mf)}{S_{Z_{r_1}Z_{r_1}}(mf)}, & H_{32}(mf) &= \frac{S_{Z_{r_2}\ddot{\phi}_s}(mf)}{S_{Z_{r_2}Z_{r_2}}(mf)},\\
H_{33}(mf) &= \frac{S_{Z_{r_3}\ddot{\phi}_s}(mf)}{S_{Z_{r_3}Z_{r_3}}(mf)}, & H_{34}(mf) &= \frac{S_{Z_{r_4}\ddot{\phi}_s}(mf)}{S_{Z_{r_4}Z_{r_4}}(mf)}, & H_{35}(mf) &= \frac{S_{F_1\ddot{\phi}_s}(mf)}{S_{F_1F_1}(mf)},\\
H_{36}(mf) &= \frac{S_{F_2\ddot{\phi}_s}(mf)}{S_{F_2F_2}(mf)}, & H_{37}(mf) &= \frac{S_{F_3\ddot{\phi}_s}(mf)}{S_{F_3F_3}(mf)}, & H_{38}(mf) &= \frac{S_{F_4\ddot{\phi}_s}(mf)}{S_{F_4F_4}(mf)}.
\end{aligned} \tag{6.15}$$

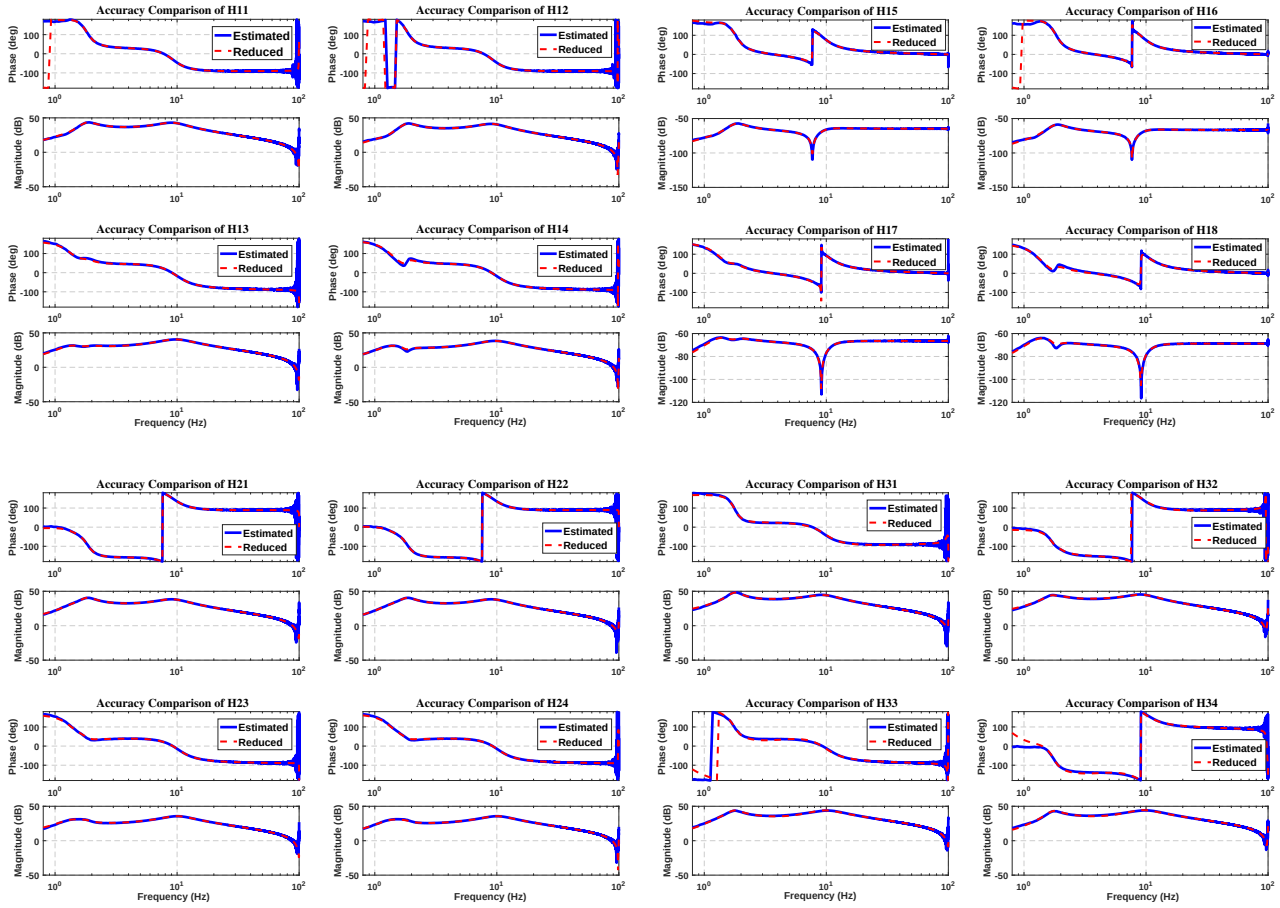

Figure 6.6: Comparison between the estimated and the reduced frequency response functions.

The estimated FRFs using (6.15) are shown in Figure 6.6. Such FRFs can be represented in a rational form by following [84] as,

$$H(z,\theta) = \frac{S_{\mathrm{m}}(z,\theta)}{U(z,\theta)} = \frac{\sum_{r=0}^{n_b} b_r z^{-r}}{\sum_{r=0}^{n_a} a_r z^{-r}}, \tag{6.16}$$

where a_r, b_r are the polynomial coefficients of poles and zeros respectively, and $\theta = [a_0\, a_1 \ldots a_{n_a}\, b_0\, b_1 \ldots b_{n_b}]^T$.

Now by using (6.8) and (6.16), we can write the input-output function as,

$$
\begin{aligned}
S_m^k(z) &= \sum_{i=0}^{N_p} \theta_i \; U_{k-i}(z), \\
Y_m^k(z) &= S_m^k(z) + \nu_k = \sum_{i=0}^{N_p} \theta_i \; U_{k-i}(z) + \nu_k, \\
Y_m^k(z) &= T_k(z) \; \theta_k(z) + \nu_k,
\end{aligned} \tag{6.17}
$$

where,

$$
\underbrace{\begin{bmatrix} Y_m^N \\ Y_m^{(N-1)} \\ \vdots \\ Y_m^{(N_p)} \\ \vdots \\ Y_m^2 \\ Y_m^1 \end{bmatrix}}_{Y_m} = \underbrace{\begin{bmatrix} U^{(N-1)} & U^{(N-2)} & \dots & U^{(N-N_p+1)} & U^{(N-N_p)} \\ U^{(N-2)} & U^{(N-3)} & \dots & U^{(N-N_p)} & U^{(N-N_p-1)} \\ \vdots & \vdots & & \vdots & \\ U^{(N_p-1)} & U^{(N_p-2)} & \dots & U^1 & U^0 \\ \vdots & \vdots & & \vdots & \\ U^1 & U^0 & \dots & U^{(2-N_p+1)} & U^{(2-N_p)} \\ U^0 & U^{-1} & \dots & U^{(1-N_p+1)} & U^{(1-N_p)} \end{bmatrix}}_{T} \underbrace{\begin{bmatrix} b_1 \\ b_2 \\ \vdots \\ b_{N_p-1} \\ \vdots \\ b_{N_p} \end{bmatrix}}_{\theta} + \underbrace{\begin{bmatrix} \nu^N \\ \nu^{(N-1)} \\ \vdots \\ \nu^{(N_p)} \\ \vdots \\ \nu^2 \\ \nu^1 \end{bmatrix}}_{\nu}.
$$

We are now able to rewrite the system as a series of output and input measurements Y_m^k and U_{k-i} at each sample $k = N$ with an undefined number of coefficients θ_i equal to N_p.

We are ready to solve these equations by applying the weighted least-squares approach to (6.17) for estimating coefficients $\hat{\theta}_{WLS}$, where the weighted matrix will be the series of

coherence values γ^2_{yu} which measures how the response is correlated to the excitation,

$$\begin{aligned} \text{Coherence} : \gamma^2_{\text{yu}}(mf) &= \frac{|S_{\text{yu}}(mf)|^2}{S_{\text{uu}}(mf)S_{\text{yy}}(mf)}, \\ \text{Estimated measurement} : \hat{Y}^k_m(z) &= T_k(z)\hat{\theta}_k(z), \\ \text{Estimated measurement error} : \tilde{Y}^k_m(z) &= Y^k_m(z) - \hat{Y}^k_m(z), \end{aligned} \tag{6.18}$$

In order to have a good model estimator, the estimated measurement error in (6.18) should be very small as an indication that the proposed estimated signals equal the true value. So, the cost function will be in the quadratic form as follows,

$$J_{WLS} := [\tilde{Y}^k_m]^T \ (\gamma^2_{\text{yu}})^k \ \tilde{Y}^k_m.$$

Taking now the gradient, $\frac{\partial J_{WLS}}{\partial \hat{\theta}_{WLS}} = 0$ we get the following,

$$\hat{\theta}_{WLS} = \left[T^T_k \ (\gamma^2_{\text{yu}})^k \ T_k\right]^{-1} T^T_k \ (\gamma^2_{\text{yu}})^k \ T_k. \tag{6.19}$$

Remark 6.1. Note that the poles in the z-domain for all transfer functions are estimated by solving (6.19). Theoretically, all 24 transfer functions must have the exact same set of poles since they are all associated with the same dynamical system. But, each transfer function was estimated independently, the poles may not be exactly at the same locations as shown in Figure 6.7. For that reason, we will use a model reduction technique to eliminate the weak states which will have small effect on the overall response.

The derived reduced model is based on the Hankel singular values for the estimated model by using the Lyapunov balancing model [85]. The Hankel singular values σ_i can be computed

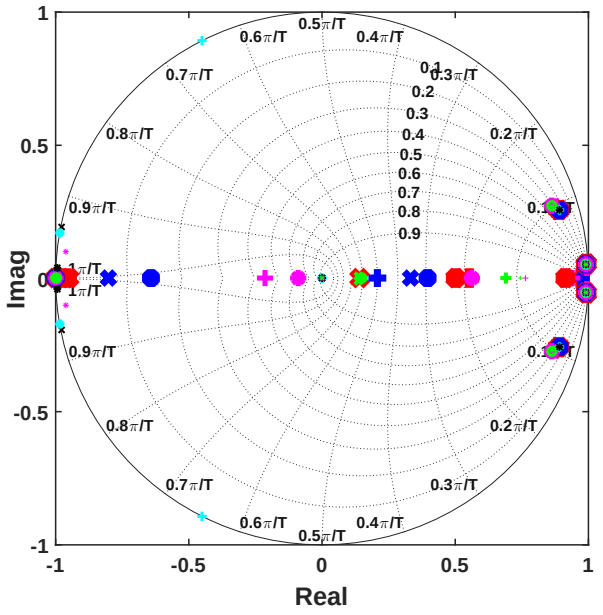

Figure 6.7: The locations of the poles of all the transfer functions in the Z-domain. It is shown that the poles for different transfer function are clustered at the same locations.

as,

$$\sigma_i = \sqrt{\lambda_i(\mathcal{P}\mathcal{O})},$$

$$\mathcal{P}(\hat{A}_d, \hat{B}_d) = \begin{bmatrix} \hat{B}_d & \hat{A}_d\hat{B}_d & \dots & \hat{A}_d^{n-1}\hat{B}_d \end{bmatrix}, \quad \mathcal{O}(\hat{A}_d, \hat{C}_d) = \begin{bmatrix} \hat{C}_d \\ \hat{C}_d\hat{A}_d \\ \vdots \\ \hat{C}_d^{n-1}\hat{A}_d \end{bmatrix},$$

where $\lambda_i(\cdot)$ is the eigenvalues of the product of controllability and observability grammians $\mathcal{P}$, and $\mathcal{O}$ respectively. The relative strength for each state in the estimated model is shown in Figure 6.8. Based on the strongest 14 states, the reduced model is calculated and evaluated as shown in Figure 6.6, which demonstrates the accuracy of the reduced model in comparison with the estimated model.

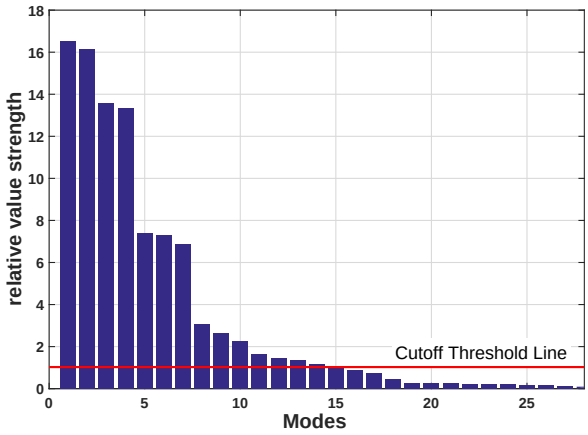

Figure 6.8: The Hankel singular values for each state. The model reduction has been calculated based on the strongest 14 states while at the same time eliminating the weak states which are under the cutoff threshold line.

6.4 Optimization-Based Control

In this section, the duality between the Kalman filter and the linear quadratic regulator (LQR) is used as a tool for improving the ride comfort and the road holding stability of a full robot model.

6.4.1 Observer Design

The goal of the observer is to estimate the plant states and dynamics with an acceptable level of accuracy at different driving and operating conditions. In order to achieve that, we will formulate an optimal output tracking problem.

Using (6.20) and (6.21), the observer dynamics are given by,

$$\hat{X}_{k+1} = \hat{A}_d \hat{X}_k + \hat{B}_{e_d} Q_k + \hat{B}_{f_d} F_k, \tag{6.20}$$

$$\hat{y}_k = \hat{C}_d \hat{X}_k + \hat{D}_{e_d} Q_k + \hat{D}_{e_d} F_k. \tag{6.21}$$

Remark 6.2. Note that the observer dynamics is the estimated model in Section 6.3, Where

$\hat{A}_d$, $\hat{B}_{e_d}$, $\hat{B}_{f_d}$, $\hat{C}_d$, $\hat{D}_{e_d}$, $\hat{D}_{f_d}$ are the estimated discrete state matrices from the reduced model (see Figure 6.3). According to the well known separation principle the observer and the controller can be designed separately, i.e., the controller gain can be computed independently of the observer gain.

We assume that Q_k is the disturbance input for the actual plant and it is not available for measurement. We can then rewrite (6.20) and (6.21) as,

$$\hat{X}_{k+1} = \hat{A}_d\hat{X}_k + \hat{B}_{f_d}F_k + L(y_{m_k} - \hat{y}_k), \tag{6.22}$$

$$\hat{y}_k = \hat{C}_d\hat{X}_k + \hat{D}_{f_d}F_k, \tag{6.23}$$

where L is a correction term added to the observer states to achieve $y_{m_k} \to \hat{y}_k$.

It is desired to obtain the optimal value L which minimizes the following cost function over infinite horizon,

$$J_L = \frac{1}{2}\sum_{k=0}^{\infty}[(y_{m_k} - \hat{y}_k)^{\mathrm{T}}M(y_{m_k} - \hat{y}_k) + L^{\mathrm{T}}RL], \tag{6.24}$$

where $R \succ 0$, $M \succeq 0$ are symmetric matrices. (6.24) can be solved in terms of the constraints (6.22) and (6.23) using optimal control theory [48, 49].

The Hamiltonian for the system is,

$$H_L = \lambda^{\mathrm{T}}[\hat{A}_d\hat{X}_k + \hat{B}_{f_d}F_k + L(y_{m_k} - \hat{y}_k)] + \frac{1}{2}[(y_{m_k} - \hat{y}_k)^{\mathrm{T}}M(y_{m_k} - \hat{y}_k) + L^{\mathrm{T}}RL].$$

The optimal control can be found by using the stationarity condition $\frac{\partial H_L}{\partial L} = 0$ as follows,

$$L^* = -\big(R + \hat{B}_{f_d}^{\mathrm{T}}P\hat{B}_{f_d}\big)^{-1}$$
$$\hat{B}_{f_d}^{\mathrm{T}}\big(P\hat{A}_d\hat{X}_k + g\big).$$

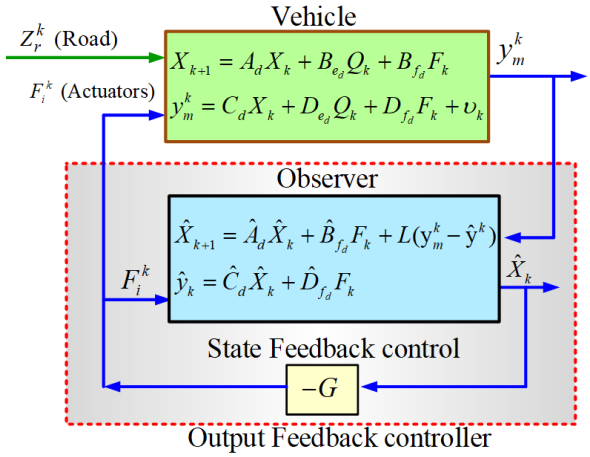

Figure 6.9: Optimal control diagram based on the augmented system of the actual robot model, the observer and the LQR state-feedback controller.

Now, we need to solve the following coupled equations,

$$\hat{A}_d^{\mathrm{T}} P \hat{A}_d - P - \hat{A}_d^{\mathrm{T}} P \hat{B}_{f_d} \left(R^{-1} + \hat{B}_{f_d}^{\mathrm{T}} P \hat{B}_{f_d}\right)^{-1} \hat{B}_{f_d}^{\mathrm{T}} P \hat{A}_d + \hat{C}_d^{\mathrm{T}} M \hat{C}_d = 0, \tag{6.25}$$

$$g = \hat{A}_d^{\mathrm{T}} \left(I + P \hat{B}_{f_d} R^{-1} \hat{B}_{f_d}^{\mathrm{T}}\right)^{-1} g - \hat{C}_d^{\mathrm{T}} M y_{m_k}.$$

6.4.2 Control Design

After estimating the plant states using the observer model, the controller can be computed by using LQR. In order to improve the ride comfort and the road holding stability, the aim of this controller is to minimize the sprung mass bounce, pitch and roll accelerations and the dynamic tire loads without violating the maximum limits of the rattle space by including the states in the weighted matrix M. In other words, the goal is to find a controller $F = [F_1, F_2, F_3, F_4]^{\mathrm{T}}$ that minimizes the cost function,

$$J_F = \frac{1}{2}\sum_{k=0}^{\infty}[\hat{X}_k^{\mathrm{T}} M \hat{X}_k + F_k^{\mathrm{T}} R F_k], \tag{6.26}$$

$$\tag{6.27}$$

which can be solved in terms of the constraints (6.22) using the differential Riccati equation (6.25) to find G,

$$F_k = -G\hat{X}_k,$$

where,

$$G = \left(R^{-1} + \hat{B}_{f_d}^{\mathrm{T}} P \hat{B}_{f_d}\right)^{-1} \hat{B}_{f_d}^{\mathrm{T}} P \hat{A}_d,$$
$$\hat{A}_d^{\mathrm{T}} P \hat{A}_d - P - \hat{A}_d^{\mathrm{T}} P \hat{B}_{f_d}\left(R^{-1} + \hat{B}_{f_d}^{\mathrm{T}} P \hat{B}_{f_d}\right)^{-1} \hat{B}_{f_d}^{\mathrm{T}} P \hat{A}_d + M = 0.$$

Based on the output feedback controller design described in Figure 6.9, the augmented system has the following form,

$$\begin{bmatrix} X_{k+1} \\ \hat{X}_{k+1} \end{bmatrix} = \underbrace{\begin{bmatrix} A_d & -B_{f_d} G_k \\ L_k C_d & \hat{A}_d - L_k \hat{C}_d - \hat{B}_{f_d} G_k - L_k (D_{f_d} - \hat{D}_{f_d}) G_k \end{bmatrix}}_{A_{aug}} \begin{bmatrix} X_k \\ \hat{X}_k \end{bmatrix} + \underbrace{\begin{bmatrix} B_{e_d} \\ 0 \end{bmatrix}}_{B_{aug}} \begin{bmatrix} Z_{r_1}^k \\ Z_{r_2}^k \\ Z_{r_3}^k \\ Z_{r_4}^k \end{bmatrix} \tag{6.28}$$

$$\begin{bmatrix} y_{m_k} \\ \hat{y}_k \end{bmatrix} = \underbrace{\begin{bmatrix} C_d & -D_{f_d} G_k \\ 0 & \hat{C}_d - \hat{D}_{f_d} G_k \end{bmatrix}}_{C_{aug}} \begin{bmatrix} X_k \\ \hat{X}_k \end{bmatrix} + \underbrace{\begin{bmatrix} D_{e_d} \\ 0 \end{bmatrix}}_{D_{aug}} \begin{bmatrix} Z_{r_1}^k \\ Z_{r_2}^k \\ Z_{r_3}^k \\ Z_{r_4}^k \end{bmatrix} + \begin{bmatrix} \nu_k \\ 0 \end{bmatrix}. \tag{6.29}$$

6.5 Simulation Results

In order to show the effectiveness and the robustness of the proposed framework, a numerical simulation has been used for validation. Where, we will firstly introduce two types of road excitation. Then, evaluating the observer performance for estimating the actual robot states with different center of gravity (CG) uncertainties. Finally, demonstrating the LQG framework for controlling the active suspension system to improve the ride comfort and the road holding stability.

The robot parameters that were considered for the simulation are shown in Table 6.1. These parameters are adopted from [47] with maximum rattle space 8 cm. The Performance Index (PI) is assessed in terms of the following aspects:

- The peak and RMS values of the sprung mass accelerations;

$$RMS\left(\ddot{z}_{\mathrm{m}}, \ddot{\theta}_{\mathrm{s}}, \ddot{\phi}_{\mathrm{s}}\right) = \sqrt{\frac{1}{k}\sum_{i=1}^{k}\left(\ddot{z}_{\mathrm{m}}^k, \ddot{\theta}_{\mathrm{s}}^k, \ddot{\phi}_{\mathrm{s}}^k\right)^2}.$$

- The RMS values of the relative tire loads;

$$RMS\left(\eta_1, \eta_2, \eta_3, \eta_4\right) = \sqrt{\frac{1}{k}\sum_{i=1}^{k}\left(\eta_1^k, \eta_2,^k \eta_3^k, \eta_4^k\right)^2}.$$

- The peak values of the relative suspension deflection; $(\mu_1, \mu_2, \mu_3, \mu_4)$.

Table 6.1: Vehicle Parameters.

Sprung mass (m_s)	2160 Kg
Front unsprung mass ($m_{1,2}$)	85 Kg
Rear unsprung mass ($m_{3,4}$)	60 Kg
Front spring stiffness (K_f)	96861 N/m
Rear spring stiffness (K_r)	52310 N/m
Tire spring stiffness (K_t)	200000 N/m
Front damping coefficient (C_f)	2460 Ns/m
Rear damping coefficient (C_r)	2281 Ns/m
CG location from front axle (a)	1.524 (m)
CG location from rear axle (b)	1.156 (m)
Wheel track ($2w$)	1.450 (m)
Pitch mass moment of inertia (I_y)	4140 ($Kg.m^2$)
Roll mass moment of inertia (I_x)	946 ($Kg.m^2$)
Rattle space limit(Z_{max})	8 (cm)

6.5.1 Road Excitation

Two road profiles are considered for analyzing the performance of the proposed scheme:

1. A bumpy road profile.

2. A road profile of class C of ISO-8608.

The two road profiles are applied to the actual system (6.4) and (6.8) with different robot speeds.

Bumpy Road

This road profile consists of two successive sinusoidal road excitation signals as illustrated in (6.30) and in Figure 6.10a. This formulation of road profile will introduce bounce, pitch and roll motion simultaneously and is given by,

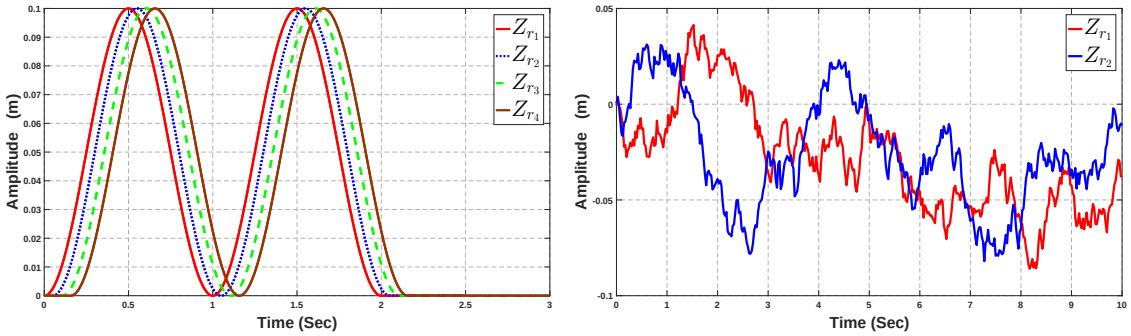

(a) Bumpy road profile. (b) ISO class C road profile.

Figure 6.10: Two road profiles used for evaluating the proposed framework. (a) a bumpy road profile with robot speed 20 m/s, (b) ISO-8606 class C road profile with robot speed 10 m/s.

$$z_{r_{1,2}} = \begin{cases} \frac{h}{2}(1 - cos\ \omega t) & \text{if} \quad 0 \leqslant t \leqslant \frac{2\lambda}{V} \\ 0 & \text{otherwise,} \end{cases}$$
$$z_{r_{3,4}} = \begin{cases} \frac{h}{2}(1 - cos\ \omega(t-\tau)) & \text{if} \quad \tau \leqslant t \leqslant \left(\tau + \frac{2\lambda}{V}\right) \\ 0 & \text{otherwise,} \end{cases} \tag{6.30}$$

where, the bump height is $h = 0.1\ m$ with wave length $\lambda = 20\ m$ and the robot speed $V = 20\ m/s$ are used for the analysis, τ is the time lag between front and rear wheels, i.e., $\tau = \frac{a+b}{V}$, with ω is the road profile frequency, i.e., $\omega = \frac{2\pi V}{\lambda}$.This road profile has an amplitude of 10 cm, which is 25% higher than the rattle space limit.

ISO Class C Road Profile

According to ISO-8608, all roads are classified from class A to class H [86] based on the power spectral density (PSD) of the road profile. Class A road has a minor degree of roughness and class H are included all roads with a high degree of roughness.

The PSD of the road profile can be calculated as [87],

$$G_d(n) = G_d(n_0).\left(\frac{n}{n_0}\right)^{-2}. \tag{6.31}$$

where, $G_d(n_0)$ is the road roughness coefficient, n is the spatial frequency, n_0 is the reference spatial frequency. In this simulation, we selected class C road which can be classified as an average degree of road roughness as shown in Figure 6.10b. Two different road profiles are applied on front left tire and front right tire with a time lag τ between front and rear wheels, i.e., $\tau = \frac{a+b}{V}$, with robot speed $V = 10\ m/s$.

6.5.2 Dynamic Behavior

In order to demonstrate the performance of the estimated model we applied the bumpy road profile as excitation signals to the actual and estimated models after setting the active suspension actuators to zero as shown in Figure 6.11a.

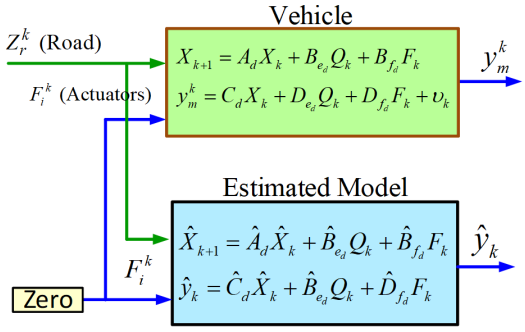

(a) The open loop diagram.

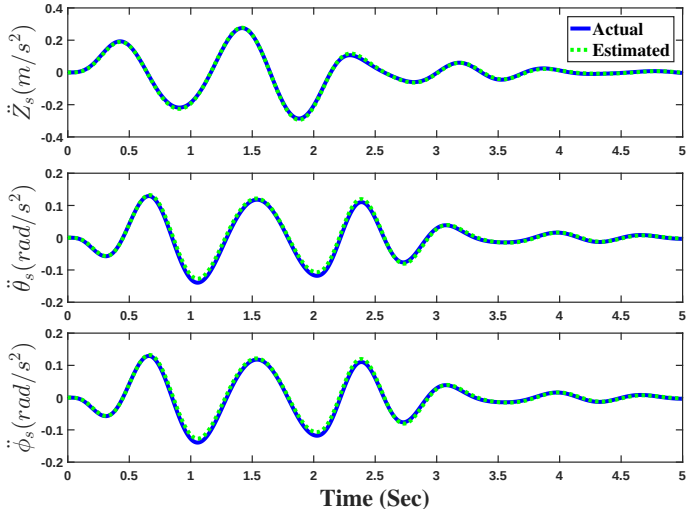

(b) Comparison between actual and estimated model.

Figure 6.11: Open loop validation. It is shown that the response of the estimated model matches the response of the actual robot model.

The response of the actual and the estimated signals are demonstrated in Figure 6.11b, where it reveals a successful matching between the estimated model and the actual model. The estimated model from Section 6.3 succeeded to capture the actual robot dynamics in estimating the sprung mass accelerations, which will allow using this estimated model in controlling the active suspension system of the actual robot to improve the ride comfort and road holding stability.

The observer behavior using the Kalman filter is evaluated first by setting the actual model at different initial conditions with respect to the estimated model. It can be seen from Figure 6.12 that the observer succeeded to track the actual model after 0.3 second.

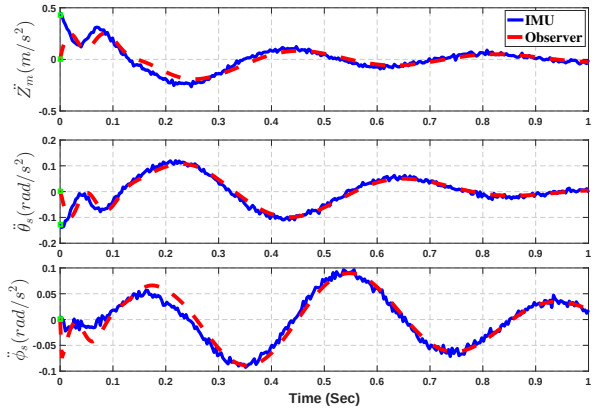

Figure 6.12: Observer behavior.

In order to evaluate the accuracy of the observer for robustly estimating the actual robot states with COM uncertainties, we calculated the estimated error, $y_s - \hat{y}$, for different positions of IMU as shown in Figure 6.13. We evaluated the observer behavior with $r_m = 0\%, 5\%, 10\%, 15\%$ and 20% with respect to the COM position. The results of the estimated error and its probability distribution illustrate that the observer can estimate the actual behavior of the robot model with 95% accuracy with up to 20% COM uncertainty.

Remark 6.3. Note that the COM position uncertainty that considered in this simulation is limited to the COM location uncertainty in the horizontal plane only $(x - y)$, and does not

evaluate the observer performance with the COM uncertainty in the entire 3-d workspace.

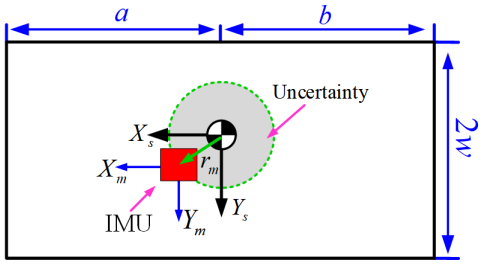

(a) CG position uncertainties.

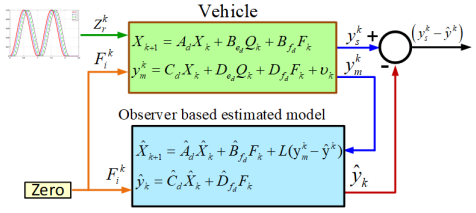

(b) Block digram for evaluating the model uncertainties.

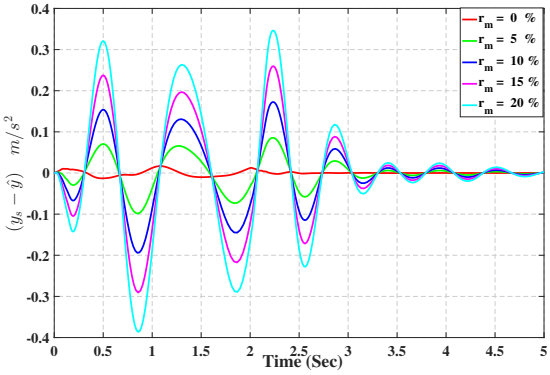

(c) Estimated error for different COM position uncertainties.

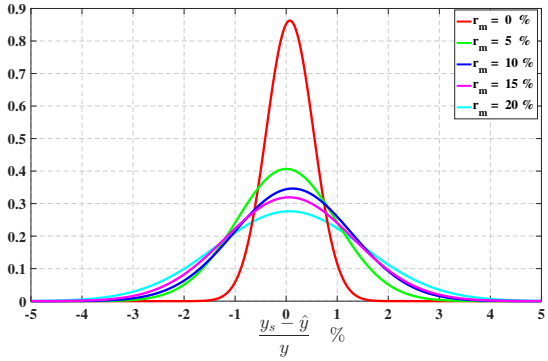

(d) Probability distribution for the estimated error.

Figure 6.13: The robustness of the observer for estimating the actual states with 0%, 5%, 10%, 15% and 20% CG uncertainties.

In terms of evaluating the improvement of ride comfort and road holding stability of the active system over the passive system, we firstly applied the bumpy road profile to the proposed augmented system in (6.28) and (6.29). It can be seen from Figure 6.14 that the Kalman filter and LQR succeed to minimize the sprung mass accelerations and the relative tire loads within the limits of the suspension rattle space.

Figure 6.15 shows the results of sprung mass accelerations, relative suspension deflection and relative tire loads using ISO class C road profile. The proposed controller scheme gives a better ride comfort than the passive system and keeps the relative tire loads and the relative suspension deflections within the hard limits to ensure road holding stability and safety. the simulation results for the two road profiles are summarized in Table 6.2.

Table 6.2: Summary of simulation results for the two road profiles.

Performance index	Measure	Bumpy Road		ISO Road	
		passive	active	passive	active
Ride Comfort	Peak $\ddot{Z}_m$	3.855	0.662	1.397	0.624
	RMS $\ddot{Z}_m$	1.638	0.302	0.454	0.193
	Peak $\ddot{\theta}_s$	2.163	0.215	1.242	0.563
	RMS $\ddot{\theta}_s$	0.971	0.107	0.443	0.164
	Peak $\ddot{\phi}_s$	0.969	0.089	1.797	0.740
	RMS $\ddot{\phi}_s$	0.420	0.043	0.595	0.225
Road Holding	RMS η_1	0.202	0.067	0.122	0.115
	RMS η_2	0.146	0.021	0.121	0.128
	RMS η_3	0.217	0.029	0.071	0.092
	RMS η_4	0.249	0.042	0.072	0.095
Rattle Space	Peak μ_1	0.322	0.802	0.198	0.252
	Peak μ_2	0.230	0.747	0.192	0.379
	Peak μ_3	0.690	0.854	0.202	0.310
	Peak μ_4	0.772	0.865	0.226	0.372

The robustness of the proposed approach was examined through a parametric study. The reduction of the RMS values of the sprung mass accelerations and the dynamic tire loads are evaluated with different robot speeds from 15 m/s up to 50 m/s using the bumpy road profile. The results are illustrated in Figure 6.16, where the average reduction of RMS values for the sprung mass accelerations and the relative tire loads were not significantly impacted by the robot speed which ascertain the applicability of the proposed approach in estimating the robot dynamics with simultaneously improving the ride comfort and road holding stability.

6.6 Summary

The robot dynamics estimation and optimal control techniques are introduced for a full robot active suspension system using a noisy IMU with COM position uncertainties. We have estimated the dynamics and the states by using system identification techniques on separate channels. Such identification techniques used excitation signals that let us to esti-

mate the system transfer functions. The response of the estimated model shows satisfactory performance in the presence of measurement uncertainties with a 95% accuracy. Then, an output-feedback controller was designed to improve ride comfort and road holding stability. Finally, simulation results are presented to demonstrate the efficiency and quantified performance of the proposed scheme.

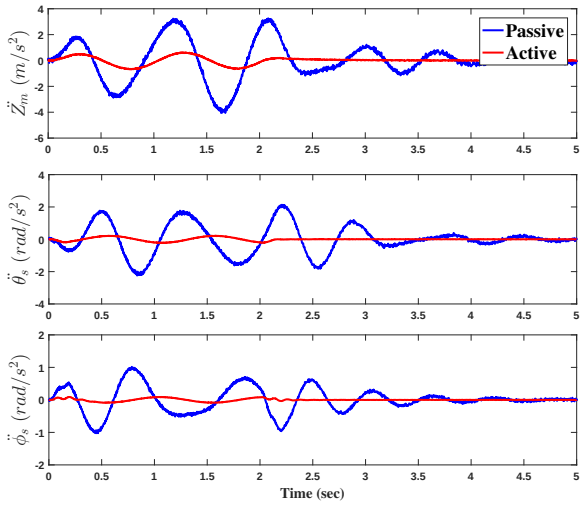

(a) Sprung mass accelerations.

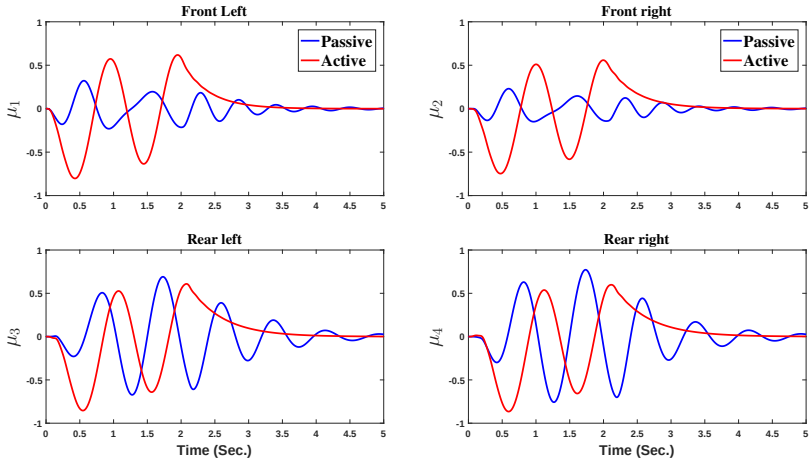

(b) Relative suspension deflections.

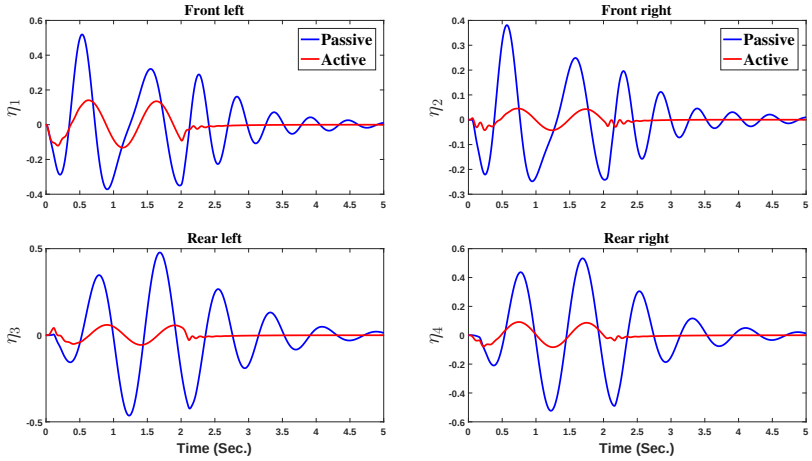

(c) Relative tire loads.

Figure 6.14: Comparison between active and passive system using a bumpy road profile. (a) sprung mass accelerations, (b) relative suspension deflection, (c) relative tire loads. It is shown that the sprung mass accelerations and the relative tire loads for the active suspension have been reduced within the limits of the available rattle space.

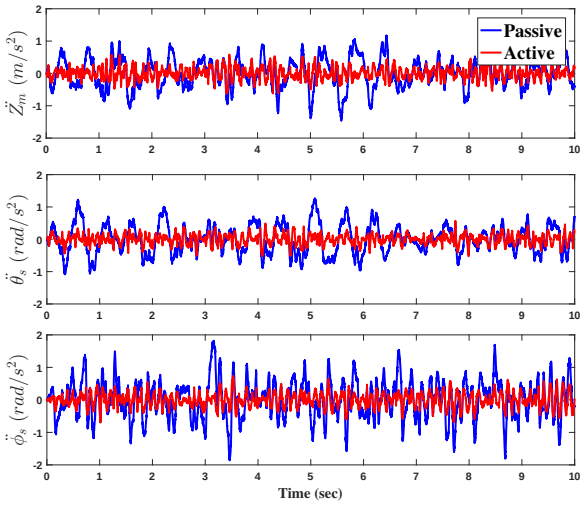

(a) Sprung mass accelerations.

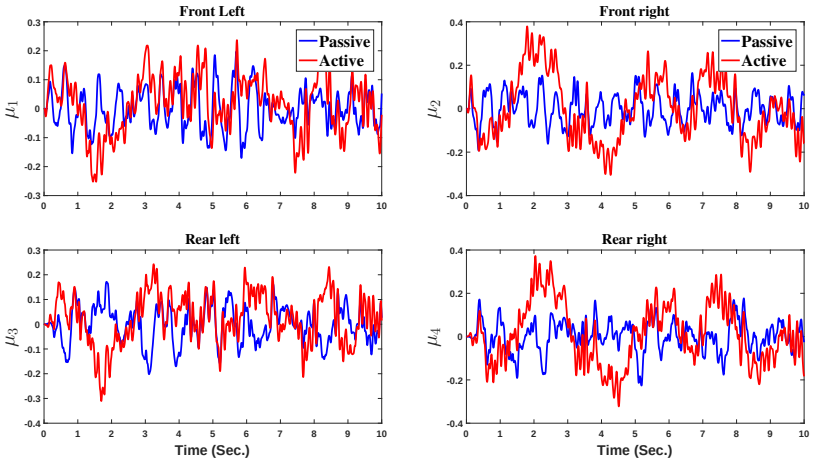

(b) Relative suspension deflections.

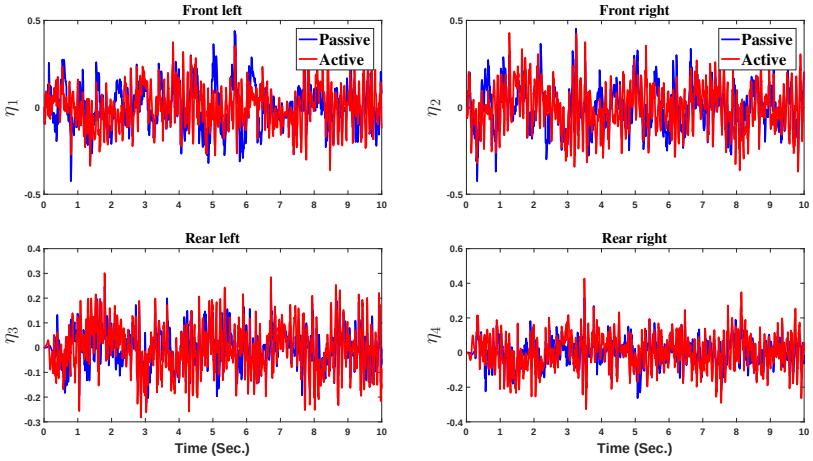

(c) Relative tire loads.

Figure 6.15: Comparison between active and passive system using ISO class C road profile. (a) sprung mass accelerations, (b) relative suspension deflection, (c) relative tire loads. It is shown that the sprung mass accelerations and the relative tire loads for the active suspension have been reduced within the limits of the available rattle space.

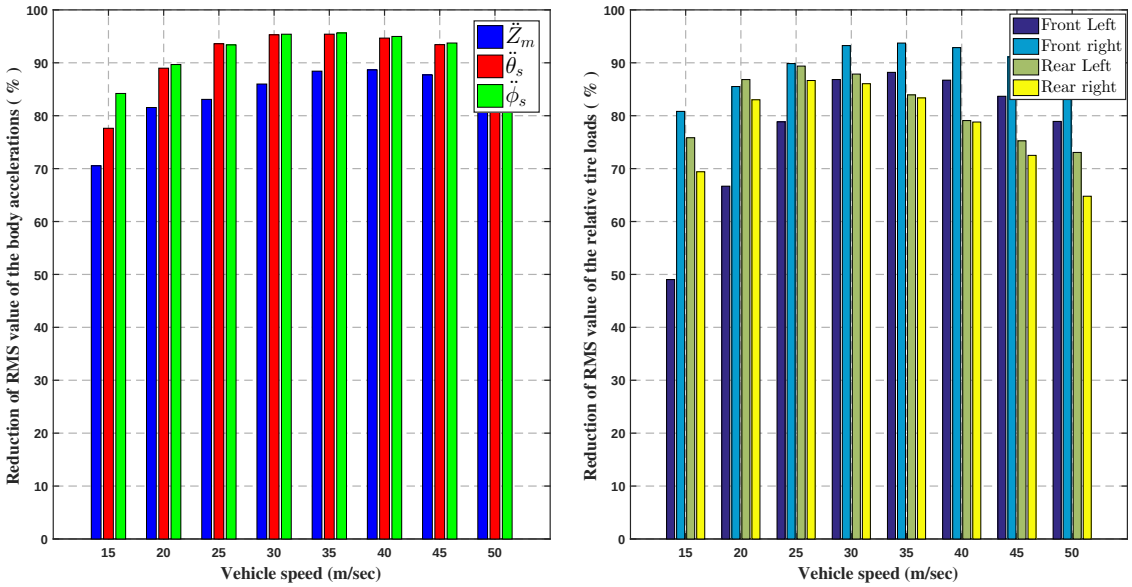

Figure 6.16: Improvement of ride comfort and road holding stability based on active suspension. It is shown that the sprung mass accelerations and the relative tire loads have been reduced at different robot speed with respect to passive system.

Chapter 7

Conclusions and Future Works

7.1 Conclusions

Wheeled mobile robots are being used for rough terrain applications in the field of robotics as a practical solution to accomplish various tasks. Unfortunately, most of the wheeled robots are not able to perform high dynamically tasks with high speed in rough terrain due to complex suspension design, high power-to-weight ratio, high cost and complexity of controlling highly nonlinear model in real-time.

The objective of this dissertation was to introduce a contribution to the robotic community by developing a novel reconfigurable wheeled robot can work in rough terrain with high stability and high speed. Following aims have been achieved in this study to meet the research objectives:

- High speed reconfigurable wheeled robot with EAM, TIGER, had been designed and developed.
- Kinematic/Dynamic simulation models for the TIGER robot with actuated suspension

system have been developed and implemented in the MATLAB/Simulink environment with validation results.

- Robot dynamic stability had been improved with the proposed suspension design in the simulation environment.
- Evaluating the robot performance in traversing slopes on rough terrain.
- Experimental tests had been carried out to demonstrate the efficiency and quantified performance of the proposed mathematical model, estimation approach and controller framework.
- The robot state-space dynamic model had been estimated with high accuracy using only a noisy single point sensor, IMU, with COM position uncertainty in the horizontal plane.

7.2 Future Work

This research can be considered as a launching point for introducing agile reconfigurable wheeled robot working on rough terrain, which has the capabilities to adapt and interact with terrain irregularities. The following directions could be pursued for improving the present research using the TIGER robot platform:

- Improving the suspension dynamics by adding a powerful actuator that has high speed/force capabilities.
- Design and implementation of steering/braking systems to improve the robot maneuverability and reduce the power consumption.
- Experimental assessment of the robot dynamic performance in rough terrain with a new powerful actuated suspension system.

- Develop a high-level control algorithm that allows the robot to operate autonomously in complex terrain.
- Applying traction control approach for improving mobility in loose terrain.
- Design a real-time parameters estimator for estimating the robot COM location, the suspension forces, and the tire forces.
- Applying plug-n-play learning techniques that do not require any offline computations to the robot nonlinear model for controlling the suspension system.

Bibliography

[1] We-Sub Eom, Youn-Kyu Kim, Joo-Hee Lee, Gi-Hyuk Choi, and Eun-Sup Sim. Study on a suspension of a planetary exploration rover to improve driving performance during overcoming obstacles. *Journal of Astronomy and Space Sciences*, 29(4):381–387, 2012.

[2] Kyungdeuk Min, Yeun-Sub Byun, and Young Chol Kim. Modelling and validation of 16 dof full vehicle model for guidance control. *International Journal of Vehicle Systems Modelling and Testing*, 10(4):392–416, 2015.

[3] Bruno Siciliano and Oussama Khatib. *Springer handbook of robotics*. Springer, 2016.

[4] D Guha-Sapir, P Hoyois, and R Below. Annual disaster statistical review 2016: the numbers and trends. cred: Brussels; 2016. *Google Scholar*.

[5] Robin R Murphy, Satoshi Tadokoro, and Alexander Kleiner. Disaster robotics. In *Springer Handbook of Robotics*, pages 1577–1604. Springer, 2016.

[6] Keiji Nagatani, Seiga Kiribayashi, Yoshito Okada, Satoshi Tadokoro, Takeshi Nishimura, Tomoaki Yoshida, Eiji Koyanagi, and Yasushi Hada. Redesign of rescue mobile robot quince. In *Safety, Security, and Rescue Robotics (SSRR), 2011 IEEE International Symposium on*, pages 13–18. IEEE, 2011.

[7] Keiji Nagatani, Seiga Kiribayashi, Yoshito Okada, Kazuki Otake, Kazuya Yoshida, Satoshi Tadokoro, Takeshi Nishimura, Tomoaki Yoshida, Eiji Koyanagi, Mineo

Fukushima, et al. Emergency response to the nuclear accident at the fukushima daiichi nuclear power plants using mobile rescue robots. *Journal of Field Robotics*, 30(1):44–63, 2013.

[8] Michael Brunner, Torsten Fiolka, Dirk Schulz, and Christopher M Schlick. Design and comparative evaluation of an iterative contact point estimation method for static stability estimation of mobile actively reconfigurable robots. *Robotics and Autonomous Systems*, 63:89–107, 2015.

[9] A Hemanth Reddy, Balla Kalyan, and Ch SN Murthy. Mine rescue robot system–a review. *Procedia Earth and Planetary Science*, 11:457–462, 2015.

[10] Dwayne Brown, Steve Cole, Guy Webster, DC Agle, Ruth Ann Chicoine, James Rickman, Rachel Hoover, Igor Mitrofanov, Michael Ravine, Donald Hassler, et al. The mars science laboratory landing. *World neurosurgery*, 79(2):223–242, 2013.

[11] Mahmoud Tarokh, G McDermott, Samad Hayati, and J Hung. Kinematic modeling of a high mobility mars rover. In *Robotics and Automation, 1999. Proceedings. 1999 IEEE International Conference on*, volume 2, pages 992–998. IEEE, 1999.

[12] Junqiang Zheng, Haibo Gao, Baofeng Yuan, Zhen Liu, Haitao Yu, Liang Ding, and Zongquan Deng. Design and terramechanics analysis of a mars rover utilising active suspension. *Mechanism and Machine Theory*, 128:125–149, 2018.

[13] Paul S Schenker, Terry L Huntsberger, Paolo Pirjanian, Eric T Baumgartner, and Eddie Tunstel. Planetary rover developments supporting mars exploration, sample return and future human-robotic colonization. *Autonomous Robots*, 14(2-3):103–126, 2003.

[14] Paul S Schenker, Paolo Pirjanian, J Balaram, KS Ali, Ashitey Trebi-Ollennu, Terrance L Huntsberger, Hrand Aghazarian, Brett A Kennedy, Eric T Baumgartner, Karl D Iagnemma, et al. Reconfigurable robots for all-terrain exploration. In *Sensor Fusion and*

Decentralized Control in Robotic Systems III, volume 4196, pages 454–469. International Society for Optics and Photonics, 2000.

[15] Karl D Iagnemma, Adam Rzepniewski, Steven Dubowsky, Paolo Pirjanian, Terrance L Huntsberger, and Paul S Schenker. Mobile robot kinematic reconfigurability for rough terrain. In *Sensor Fusion and Decentralized Control in Robotic Systems III*, volume 4196, pages 413–421. International Society for Optics and Photonics, 2000.

[16] David Wettergreen, Scott Moreland, Krzysztof Skonieczny, Dominic Jonak, David Kohanbash, and James Teza. Design and field experimentation of a prototype lunar prospector. *The International Journal of Robotics Research*, 29(12):1550–1564, 2010.

[17] Hiroaki Inotsume, Masataku Sutoh, Kenji Nagaoka, Keiji Nagatani, and Kazuya Yoshida. Modeling, analysis, and control of an actively reconfigurable planetary rover for traversing slopes covered with loose soil. *Journal of Field Robotics*, 30(6):875–896, 2013.

[18] Hiroaki Inotsume, Masataku Sutoh, Kenji Nagaoka, Keiji Nagatani, and Kazuya Yoshida. Evaluation of the reconfiguration effects of planetary rovers on their lateral traversing of sandy slopes. In *ICRA*, pages 3413–3418, 2012.

[19] Gustavo Freitas, Fernando Lizarralde, Liu Hsu, and Marcel Bergerman. Terrain model-based anticipative control for articulated vehicles with low bandwidth actuators. In *Robotics and Automation (ICRA), 2013 IEEE International Conference on*, pages 382–389. IEEE, 2013.

[20] John Billingsley, Arto Visala, and Mark Dunn. Robotics in agriculture and forestry. In *Springer handbook of robotics*, pages 1065–1077. Springer, 2008.

[21] Gustavo Freitas, Gabriel Gleizer, Fernando Lizarralde, Liu Hsu, and Ney Robinson Salvi

dos Reis. Kinematic reconfigurability control for an environmental mobile robot operating in the amazon rain forest. *Journal of Field Robotics*, 27(2):197–216, 2010.

[22] James Trevelyan, William R Hamel, and Sung-Chul Kang. Robotics in hazardous applications. In *Springer handbook of robotics*, pages 1521–1548. Springer, 2016.

[23] Gustavo Freitas, Gabriel Gleizer, Fernando Lizarralde, and Liu Hsu. Multi-objective optimization for kinematic reconfiguration of mobile robots. In *Automation Science and Engineering (CASE), 2010 IEEE Conference on*, pages 686–691. IEEE, 2010.

[24] Gustavo Freitas, Fernando Lizarralde, Liu Hsu, and Ney R Salvi Dos Reis. Kinematic reconfigurability of mobile robots on irregular terrains. In *Robotics and Automation, 2009. ICRA'09. IEEE International Conference on*, pages 1340–1345. IEEE, 2009.

[25] William Reid, Francisco Javier Pérez-Grau, Ali Haydar Göktoğan, and Salah Sukkarieh. Actively articulated suspension for a wheel-on-leg rover operating on a martian analog surface. In *Robotics and Automation (ICRA), 2016 IEEE International Conference on*, pages 5596–5602. IEEE, 2016.

[26] Edgar A Martinez-Garcia, Erik Lerín-García, and Rafael Torres-Cordoba. A multi-configuration kinematic model for active drive/steer four-wheel robot structures. *Robotica*, 34(10):2309–2329, 2016.

[27] Bahareh Ghotbi, Francisco González, József Kövecses, and Jorge Angeles. Mobility evaluation of wheeled robots on soft terrain: Effect of internal force distribution. *Mechanism and Machine Theory*, 100:259–282, 2016.

[28] Bahareh Ghotbi, Francisco González, József Kövecses, and Jorge Angeles. Effect of normal force dispersion on the mobility of wheeled robots operating on soft soil. In *Robotics and Automation (ICRA), 2014 IEEE International Conference on*, pages 6612–6617. IEEE, 2014.

[29] William Reid, AH Goktogan, and Salah Sukkarieh. Moving mammoth: Stable motion for a reconfigurable wheel-on-leg rover. In *Proceedings of Australasian Conference on Robotics and Automation*, pages 1–10, 2014.

[30] Christophe Grand, Faïz Benamar, Frédéric Plumet, and Philippe Bidaud. Stability and traction optimization of a reconfigurable wheel-legged robot. *The International Journal of Robotics Research*, 23(10-11):1041–1058, 2004.

[31] PetersenRol Josh SentisEmail, Luis and Roland Philippsen. Implementation and stability analysis of prioritized whole-body compliant controllers on a wheeled humanoid robot in uneven terrains. *Autonomous Robots*, 35(4):301–319, 2010.

[32] Luis Sentis, Josh Petersen, and Roland Philippsen. Experiments with balancing on irregular terrains using the dreamer mobile humanoid robot. In *Robotics: Science and Systems (RSS) 2012, University of Sydney, Sydney, NSW, Australia, July 09-13, 2012*, volume 8, pages 393–400. MIT Press, 2013.

[33] Salvador Rojas, He Shen, Holly Griffiths, Ni Li, and Lanchun Zhang. Motion and gesture compliance control for high performance of a wheeled humanoid robot. In *ASME 2017 International Mechanical Engineering Congress and Exposition*, pages V04AT05A058–V04AT05A058. American Society of Mechanical Engineers, 2017.

[34] Tom B Lauwers, George A Kantor, and Ralph L Hollis. A dynamically stable single-wheeled mobile robot with inverse mouse-ball drive. In *Robotics and Automation, 2006. ICRA 2006. Proceedings 2006 IEEE International Conference on*, pages 2884–2889. IEEE, 2006.

[35] Songyan Xin, Yangwei You, Chengxu Zhou, Cheng Fang, and Nikos Tsagarakis. A torque-controlled humanoid robot riding on a two-wheeled mobile platform. In *Intelli-*

gent Robots and Systems (IROS), 2017 IEEE/RSJ International Conference on, pages 1435–1442. IEEE, 2017.

[36] Bernd Henze, Máximo A Roa, and Christian Ott. Passivity-based whole-body balancing for torque-controlled humanoid robots in multi-contact scenarios. *The International Journal of Robotics Research*, 35(12):1522–1543, 2016.

[37] Scott Kuindersma, Robin Deits, Maurice Fallon, Andrés Valenzuela, Hongkai Dai, Frank Permenter, Twan Koolen, Pat Marion, and Russ Tedrake. Optimization-based locomotion planning, estimation, and control design for the atlas humanoid robot. *Autonomous Robots*, 40(3):429–455, 2016.

[38] Hongkai Dai and Russ Tedrake. Planning robust walking motion on uneven terrain via convex optimization. In *Humanoid Robots (Humanoids), 2016 IEEE-RAS 16th International Conference on*, pages 579–586. IEEE, 2016.

[39] Manuel Kudruss, Maximilien Naveau, Olivier Stasse, Nicolas Mansard, Christian Kirches, Philippe Soueres, and K Mombaur. Optimal control for whole-body motion generation using center-of-mass dynamics for predefined multi-contact configurations. In *Humanoid Robots (Humanoids), 2015 IEEE-RAS 15th International Conference on*, pages 684–689. IEEE, 2015.

[40] Mirko Čorić, Joško Deur, Li Xu, H Eric Tseng, and Davor Hrovat. Optimisation of active suspension control inputs for improved vehicle ride performance. *Vehicle system dynamics*, 54(7):1004–1030, 2016.

[41] Jianbo Lu and Mark DePoyster. Multiobjective optimal suspension control to achieve integrated ride and handling performance. *IEEE Transactions on Control Systems Technology*, 10(6):807–821, 2002.

[42] Weichao Sun, Huijun Gao, and Bin Yao. Adaptive robust vibration control of full-car active suspensions with electrohydraulic actuators. *IEEE Transactions on Control Systems Technology*, 21(6):2417–2422, 2013.

[43] Edward J Haug. *Computer aided kinematics and dynamics of mechanical systems*, volume 1. Allyn and Bacon Boston, 1989.

[44] Honghai Liu, Huijin Gao, and Ping Li. *Handbook of vehicle suspension control systems*. Institution of Engineering and Technology, 2013.

[45] Reza N Jazar. *Vehicle dynamics*. Springer, 2008.

[46] Rajesh Rajamani. *Vehicle dynamics and control*. Springer Science & Business Media, 2011.

[47] Anil Shirahatti, PSS Prasad, Pravin Panzade, and MM Kulkarni. Optimal design of passenger car suspension for ride and road holding. *Journal of the Brazilian Society of Mechanical Sciences and Engineering*, 30(1):66–76, 2008.

[48] Feng Lin. *Robust control design: an optimal control approach*, volume 18. John Wiley & Sons, 2007.

[49] Frank L Lewis, Draguna Vrabie, and Vassilis L Syrmos. *Optimal Control*. John Wiley & Sons, 2012.

[50] Egbert Bakker, Lars Nyborg, and Hans B Pacejka. Tyre modelling for use in vehicle dynamics studies. Technical report, SAE Technical Paper, 1987.

[51] Etsuo Katsuyama and Ayana Omae. Improvement of ride comfort by unsprung negative skyhook damper control using in-wheel motors. *SAE International Journal of Alternative Powertrains*, 5(2016-01-1678):214–221, 2016.

[52] MA Ajaj, AM Sharaf, SA Hegazy, and YH Hossamel-deen. Investigation of control algorithms for semi-active suspension systems based on a full vehicle model. In *ASME 2011 International Mechanical Engineering Congress and Exposition*, pages 187–197. American Society of Mechanical Engineers, 2011.

[53] Vaijayanti S Deshpande, PD Shendge, and SB Phadke. Dual objective active suspension system based on a novel nonlinear disturbance compensator. *Vehicle System Dynamics*, 54(9):1269–1290, 2016.

[54] Jo Yung Wong. *Theory of ground vehicles*. John Wiley & Sons, 2008.

[55] Wuwei Chen, Hansong Xiao, Qidong Wang, Linfeng Zhao, and Maofei Zhu. *Integrated vehicle dynamics and control*. John Wiley & Sons, 2016.

[56] Mohamed Bouazara and Marc J Richard. An optimization method designed to improve 3-d vehicle comfort and road holding capability through the use of active and semi-active suspensions. *European journal of mechanics-A/Solids*, 20(3):509–520, 2001.

[57] Yingbo Huang, Jing Na, Xing Wu, Xiaoqin Liu, and Yu Guo. Adaptive control of nonlinear uncertain active suspension systems with prescribed performance. *ISA transactions*, 54:145–155, 2015.

[58] H Eric Tseng and Davor Hrovat. State of the art survey: active and semi-active suspension control. *Vehicle system dynamics*, 53(7):1034–1062, 2015.

[59] Fumiaki Yamada, Kohei Suzuki, Tatsuo Toda, Gan Chen, and Isao Takami. Robust control of active suspension to improve ride comfort with structural constraints. In *Advanced Motion Control (AMC), 2016 IEEE 14th International Workshop on*, pages 103–108. IEEE, 2016.

[60] Sebastian Spirk and Boris Lohmann. Controlling an active suspension using methods of

optimal control. In *Decision and Control (CDC), 2012 IEEE 51st Annual Conference on*, pages 6333–6339. IEEE, 2012.

[61] S Thenmozhi and K Rajeswari. Kalman estimator for an active suspension system. In *Advances in Engineering, Science and Management (ICAESM), 2012 International Conference on*, pages 155–160. IEEE, 2012.

[62] Jing Na, Guido Herrmann, and Kyriakos G Vamvoudakis. Adaptive optimal observer design via approximate dynamic programming. In *American Control Conference (ACC), 2017*, pages 3288–3293. IEEE, 2017.

[63] Tamer Attia, Kevin Kochersberger, John Bird, and Steve C Southward. System identification and optimal control of half-car active suspension system using a single noisy imu with position uncertainty. In *ASME 2017 Dynamic Systems and Control Conference*, pages V002T04A002–V002T04A002. American Society of Mechanical Engineers, 2017.

[64] Thomas A Wenzel, KJ Burnham, MV Blundell, and RA Williams. Dual extended kalman filter for vehicle state and parameter estimation. *Vehicle System Dynamics*, 44(2):153–171, 2006.

[65] Guido Koch, Tobias Kloiber, and Boris Lohmann. Nonlinear and filter based estimation for vehicle suspension control. In *Decision and Control (CDC), 2010 49th IEEE Conference on*, pages 5592–5597. IEEE, 2010.

[66] Nils Pletschen and Klaus J Diepold. Nonlinear state estimation for suspension control applications: A takagi-sugeno kalman filtering approach. *Control Engineering Practice*, 61:292–306, 2017.

[67] Nils Pletschen, Stefan Barthelmes, and Boris Lohmann. Joint state-parameter estimation for active vehicle suspensions: A takagi-sugeno kalman filtering approach. In

Decision and Control (CDC), 2015 IEEE 54th Annual Conference on, pages 1545–1550. IEEE, 2015.

[68] Nils Pletschen and Patrick Badur. Nonlinear state estimation in suspension control based on takagi-sugeno model. *IFAC Proceedings Volumes*, 47(3):11231–11237, 2014.

[69] Christian Graf, Rüdiger Kieneke, and Jürgen Maas. Online force estimation for an active suspension control. In *Advanced Intelligent Mechatronics (AIM), 2012 IEEE/ASME International Conference on*, pages 544–549. IEEE, 2012.

[70] Jeremy Kolansky and Corina Sandu. Enhanced polynomial chaos-based extended kalman filter technique for parameter estimation. *Journal of Computational and Nonlinear Dynamics*, 13(2):021012, 2018.

[71] Jeremy Kolansky, Corina Sandu, Theunis Botha, and Schalk Els. Real-time vehicle parameters estimation. In *ASME 2013 International Design Engineering Technical Conferences and Computers and Information in Engineering Conference*, pages V001T01A025–V001T01A025. American Society of Mechanical Engineers, 2013.

[72] Emmanuel Blanchard, Adrian Sandu, and Corina Sandu. Parameter estimation for mechanical systems using an extended kalman filter. 2008.

[73] Emmanuel D Blanchard, Adrian Sandu, and Corina Sandu. Parameter estimation method using an extended kalman filter. 2007.

[74] Emmanuel Blanchard, Corina Sandu, and Adrian Sandu. A polynomial-chaos-based bayesian approach for estimating uncertain parameters of mechanical systems. In *ASME 2007 International Design Engineering Technical Conferences and Computers and Information in Engineering Conference*, pages 1041–1048. American Society of Mechanical Engineers, 2007.

[75] Emmanuel Blanchard, Adrian Sandu, and Corina Sandu. A polynomial chaos based bayesian approach for estimating uncertain parameters of mechanical systems-part ii: Applications to vehicle systems. 2007.

[76] Sara D García and Diego Patino. Estimation based on acceleration measures of an active suspension plant. In *Automatic Control (CCAC), 2015 IEEE 2nd Colombian Conference on*, pages 1–6. IEEE, 2015.

[77] Sandra Thaller, Florian Reiterer, Roman Schmied, Harald Waschl, Helmut Kokal, and Luigi del Re. Fast determination of vehicle suspension parameters via continuous time system identification. *IFAC-PapersOnLine*, 49(11):448–453, 2016.

[78] Gianpiero Mastinu and Manfred Plöchl. *Road and off-road vehicle system dynamics handbook*. CRC Press, 2014.

[79] AJ Healey, E Nathman, and CC Smith. An analytical and experimental study of automobile dynamics with random roadway inputs. *Journal of Dynamic Systems, Measurement, and Control*, 99(4):284–292, 1977.

[80] R.E. Smith and D.R. Sigman. Experimental verification of a linear rigid body model. *Ford Motor Company Research Report*, Dearborn, MI, October 1981.

[81] Alan V Oppenheim. *Discrete-time signal processing Third Edition*. Upper Saddle River, NJ: Pearson Higher Education, Inc, 2010.

[82] Lennart Ljung. System identification. In *Signal analysis and prediction*, pages 163–173. Springer, 1998.

[83] Matteo Frigo and Steven G Johnson. Fftw: An adaptive software architecture for the fft. In *Acoustics, Speech and Signal Processing, 1998. Proceedings of the 1998 IEEE International Conference on*, volume 3, pages 1381–1384. IEEE, 1998.

[84] Rik Pintelon and Johan Schoukens. *System identification: a frequency domain approach*. John Wiley & Sons, 2012.

[85] Serkan Gugercin and Athanasios C Antoulas. A survey of balancing methods for model reduction. In *European Control Conference (ECC), 2003*, pages 968–973. IEEE, 2003.

[86] ISO-8608. Mechanical vibration - road surface profiles - reporting of measured data, 1995.

[87] M Agostinacchio, D Ciampa, and S Olita. The vibrations induced by surface irregularities in road pavements–a matlab® approach. *European Transport Research Review*, 6(3):267–275, 2014.